Studies of Titanium-based Anti-Cancer Agents and their Effects on Cancer Cell Lines

Thesis submitted to the University of Nottingham for the degree of

Master of Research

September, 2025

Theresia Brigita Rangga Allo Anginan

20709295

Supervisors: Prof Simon Woodward, Dr Tracey Bradshaw, Prof Neil R Thomas

School of Chemistry, Faculty Science

University of Nottingham

Abstract

Cancer is a leading cause of mortality worldwide, and there is an urgent need for development of new therapies. Pancreatic ductal adenocarcinoma (PDAC), on the other hand, is the most aggressive types of cancers, with 90% of pancreatic cancer cases worldwide. In most cancers, especially pancreatic cancer, increased cellular iron uptake is observed, mediated by transferrin/(apo)ferritin (iron transport) proteins. Cellular iron uptake is typically via the transferrin receptor 1 (TfR1, also known as CD71). This is overexpressed in cancer cells, as iron is required for cell growth, for regulating ROS production and for mitochondrial respiration. This thesis proposes utilising the enhanced TfR1 expression of cancer cells to deliver anti-cancer agents. Specifically, we use tripodal *O-N-O bis*-phenolateamine titanium(IV) complexes which have already demonstrated potent *in vitro* anti-cancer activity towards MCF-7 and HCT-116 cancer cell lines. We proposed testing these complexes` activities against PANC-1 pancreatic cancer cells (including as spheroid clusters) and to investigate encapsulation strategies for them within apoferritin.

Discussed in Chapter 2, $[Ti\{MeN(CH_2C_6H_2\text{-}2\text{-}O\text{-}4\text{-}OMe\text{-}6\text{-}R)_2\}_2$ (**2.1a** R = Me; **2.1b** R = allyl, **2.1c** R = fluoro) were prepared with overall yields of 21-65%. The activity of **2.1a** was tested against 2D PANC-1 pancreatic cell lines using MTT and clonogenic assays. The MTT results show both complexes have GI_{50} values < 5 µM, which is lower than cisplatin (used as a positive control). Clonogenic assays of **2.1a** show that the titanium complex also disrupts PANC-1 colony formation by 90% at 10 µM concentrations. Preparation of PANC-1 3D spheroid models (spherical collections of ca. 2500 cells) was optimised to mimic small pancreatic tumours in the human body. Spheroid volume measurement concurred to reveal that treatment with **2.1**

(10 μM) resulted decreased volume of the spheroid 82% relative to control after 72 hours of treatment.

Initial attempts to encapsulate complex **2.1a** into horse spleen apoferritin using a standard pH dependent re-assembly method,[2] led to no detectable titanium species (by ICPMS) within the apoferritin cage. We propose that **2.1a** undergoes decomposition by hydrolysis more rapidly when it is entrapped in apoferritin. We studied the related hydrolysis behaviour of **2.1b** by UV-vis spectroscopy. Solutions of 76 μM **2.1b** in either: (i) DMSO/deionised water (20:80), (ii) DMSO/8 M aqueous urea (20:80), (iii) DMSO/pH 5, 0.1 M acetate buffer (20:80) or (iv) DMSO/ pH 7.4, 0.1 M phosphate buffer (20:80) were compared. We found that the hydrolysis intermediate (resulting from ligand loss from **2.1b**) is especially stable in the presence of DMSO/8 M aqueous urea (20:80), suggesting that 8 M urea-based encapsulation might form the basis of a better strategy for apoferritin encapsulated titanium agents.

In Chapter 3 we describe activity of alternative experimental anti-cancer agents: 4-amino-1,5-dimethyl-2-phenyl-1,2-dihydro-3*H*-pyrazol-3-one (2-ATA) and 2-arylthiazol-5-amine (4-AAP) derivatives as comparators for our titanium work. Preliminary MTT spot tests (at agent concentrations of 10 nM and 100 μM) in HCT-116 colon and MCF-7 breast cancer cell lines revealed only modest activity with greater growth-inhibitory effects apparent in the MCF-7 cell line for most of the tested agents. The activity of three of the more potent compounds (**3.1, 3.6, 3.7**) were further tested against both cell lines using dose-response MTT and clonogenic assays. The MTT results show compound **3.1** (N^1-(1,5-dimethyl-3-oxo-2-phenyl-2,3-dihydro-1*H*-pyrazol-4-yl)-N^4-phenylsuccinamide) gave the highest GI_{50} values: 1.73±0.6 μM and 0.752±0.1 μM against HCT-116 and MCF-7 cells respectively. These results are comparable

to the cisplatin positive control (GI_{50} values 1.27±0.3 μM and 0.69±0.1 μM) against HCT-116 and MCF-7 respectively.

Acknowledgements

I should like to offer my thanks to everyone who helped me carry out this Master's thesis, I would like to express my biggest gratitude to God for all His mercy and blessings during the thesis work and allowing my successfully completion within the course deadline.

I give my sincere thanks to my funding agency, the LPDP for their support throughout my period of study. I am very grateful to my main supervisor, Professor Simon Woodward, for his unwavering support in this project. His consistent support, patience, and his detail-oriented personality helped the author finish this thesis and overcome a lot of obstacles during the research path. I thank Prof Woodward helping me expand my laboratory skills, as I am a 'new person' in Chemistry. I also want to extend my gratitude to my co-supervisors, Dr Tracey Bradshaw and Prof Neil R Thomas, for their support and advice in preparing this thesis work.

I would like to express my gratitude to my family: my parents (Matias Herman and Maria Limbong), Angelina Rangga Allo Anginan, and Gregorius Andi Tenriadjeng for their unwavering support and encouragement during my study period. I am so very grateful for the advice and guidance given by my family enabling me to finish this present work and hopefully reach my dream in the future. I thank them also for their love and support.

I thank all members of the Woodward laboratory group and 'Apoferritin Team' for their help during this project. I particularly thank my laboratory best friends: Sarah Prayle, Catherine Liberty, and Christian Aspinall for their support, help and advice during the thesis writing period and in the lab.

Finally, I want to give especial thanks to my best friends for their support during the thesis development period: members of LPDP Nottingham and members of PPI Nottingham. Thank

you very much for becoming the ‘best supporters’ and always being the best listeners whenever I needed help. Lastly, I want to thank everybody not specifically mentioned in this section, but who have helped during this thesis project in all manner of ways. This thesis project could not have been carried out without the help and support given above by you all. Thank you very much!

Sincerely,

Theresia Brigita Rangga Allo Anginan

List of Abbreviation

ATP	Adenosine triphosphate
Bcl-2/Bcl-xL	B-cell lymphoma 2
BRCA	Breast cancer gene
c-MYC	Cellular myelocytomatosis oncogene
Cp	Cyclopentadienyl
CRC	Colorectal cancer
CSC	Cancer stem cell
CTR-1	Copper transporter 1
DMSO	Dimethyl sulfoxide
EAT	*Ehrlich ascites tumours*
ECM	Extracellular matrix
EELS	Electron energy loss spectroscopy
ER	Oestrogen receptor
EMT	Epithelial-mesenchymal transition
FTH	Ferritin heavy chain
FTL	Ferritin light chain
GLUT-1	Glucose transporter type 1
HCT-116	Human colorectal carcinoma 116
HEP	Hepcidin
HER2	Human epidermal growth factor receptor 2
HSAFt	Horse spleen apoferritin
K-Ras	Kirsten rat sarcoma viral oncogene
IM	Immunomodulatory
LAR	Luminal androgen receptor
LMCT	Ligand-to-metal charge transfer

MAP	Mitogen-Activated Protein
MCF-7	Michigan Cancer Foundation-7 (breast ductal carcinoma)
MDA-MB-468	Breast adenocarcinoma
mg	Milligram
mL	Millilitre
µL	Microlitre
µM	Micromolar
MRC-5	Medical Research Council 5 (normal fibroblast cell line)
MSL	Mesenchymal stem-like
MTT	3-(4,5-Dimethylthiazol-2-yl)-2,5-diphenyltetrazolium bromide
NER	Nucleotide excision repair
NF-κB	Nuclear factor of the κ-chain in B-cells
NK cells	Natural killer
PANC-1	Pancreatic cancer
PDAC	Pancreatic ductal adenocarcinoma
PI3K/AKT	Phosphatidylinositol 3-kinase
ULA	Ultra-low attachment
ROS	Reactive oxygen species
RB	Retinoblastoma
SAR	Structure activity relationship
TfR-1	Transferrin receptor 1
TNBC	Triple-negative breast cancer
TP53	Tumour protein 53

Table of Contents

1. CHAPTER ONE: INTRODUCTION

1.1. Tumours and malignant cells

The word 'tumour' is derived from the Latin word *tumor* meaning a swelling. In modern medicine, tumours are defined as populations of abnormal cells which show unregulated growth. Tumours can be characterised into two types: benign tumours and malignant tumours. A benign tumour is characterised by having cells with normal chromosomes, infrequent cell division, and moderate cellular development. Additionally, benign tumours do not have an ability to spread to other parts of the body. Conversely, malignant tumours are characterised by having cells with both abnormal chromosomes and proliferation characteristics, and the ability to invade surrounding tissue (metastasis). Such malignant tumour tissues are often referred to as 'cancers'.

1.2. Cancer

Cancer is a general term for a group of diseases that arise and affect any part of the body. According to World Health Organization (2025), cancer is the leading cause of death worldwide, with an incidence rate of around 20 million new cases and 10 million deaths per year (2020 data).[1] Cancer, by definition, is a progressive disease that arises from abnormal proliferation of cells. This gives rise to complex tissue masses which have the ability to promote the growth of new blood vessels (angiogenesis), thereby facilitating the invasion of neighbouring tissues, allowing their spread to other parts of the body.

Most cancers share the same similarities and features, which are referred to as 'hallmarks'.[2–4] Commonly recognised hallmarks of cancer include: sustaining proliferative signalling, evading growth suppressors, non-mutational epigenetic reprogramming, avoiding immune

destruction, tumour promoting inflammation, polymorphic microbiome, resisting cell death, enabling replicative immortality, inducing angiogenesis, senescent cells, genome instability and mutation, deregulating cellular metabolism, unlocking phenotypic plasticity, sustaining proliferative signalling, and activating invasion and metastasis.[2] These hallmarks of cancer are discussed in more detail in the next section. Often the ultimate source of the appearance of such cancer hallmarks is the genetic instability of the cells and their resultant abnormal requirement to sustain growth, discussed in Section 1.3. This also leads to the heterogeneity of cancer (the diversity of tumour characteristics in nominally identical patients), which plays an important role in tumorigenesis.

1.3. Hallmarks of cancer

The hallmarks of cancer have already been introduced and are summarised in Figure 1.1 below.

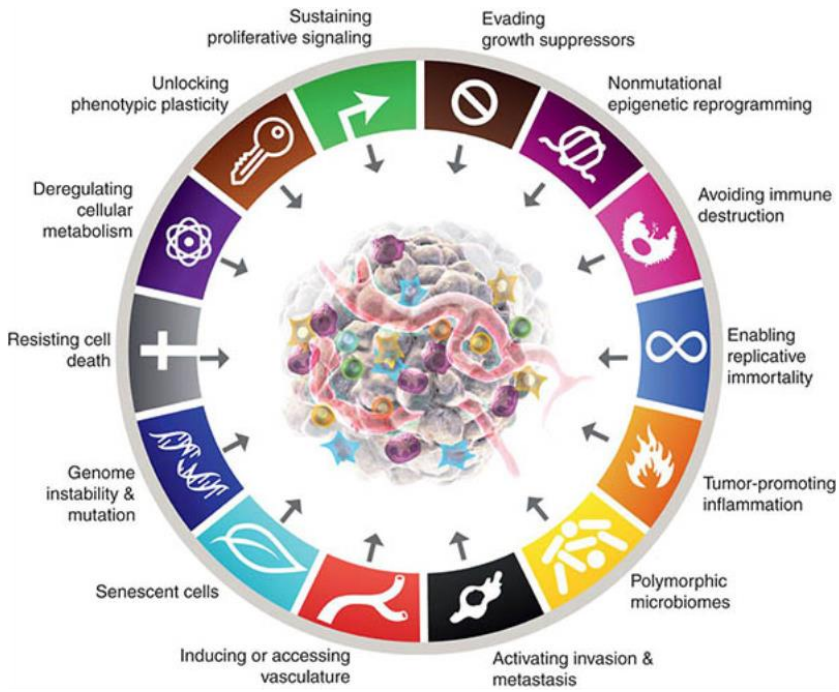

Figure 1.1. A graphical summary of the hallmarks of cancer (taken from ref. 4).

The most important and fundamental hallmark of malignant cells is their ability to sustain proliferative signals, leading to chronic cellular proliferation.[4] Normal cells have the ability to maintain homeostasis (typical behaviour) by controlling the production and release of growth-promoting signalling entities. Cancer cells, however, deregulate these signalling pathways. The capability of cancer cells to sustain proliferative signalling is achieved by several mechanisms, including production of growth factors to deliver autocrine (i.e. self) proliferative stimulation and upregulation of receptor signalling leading to hyper-activation of growth factor ligand responses (see the signal pathways of Figure 1.2).[5,6]

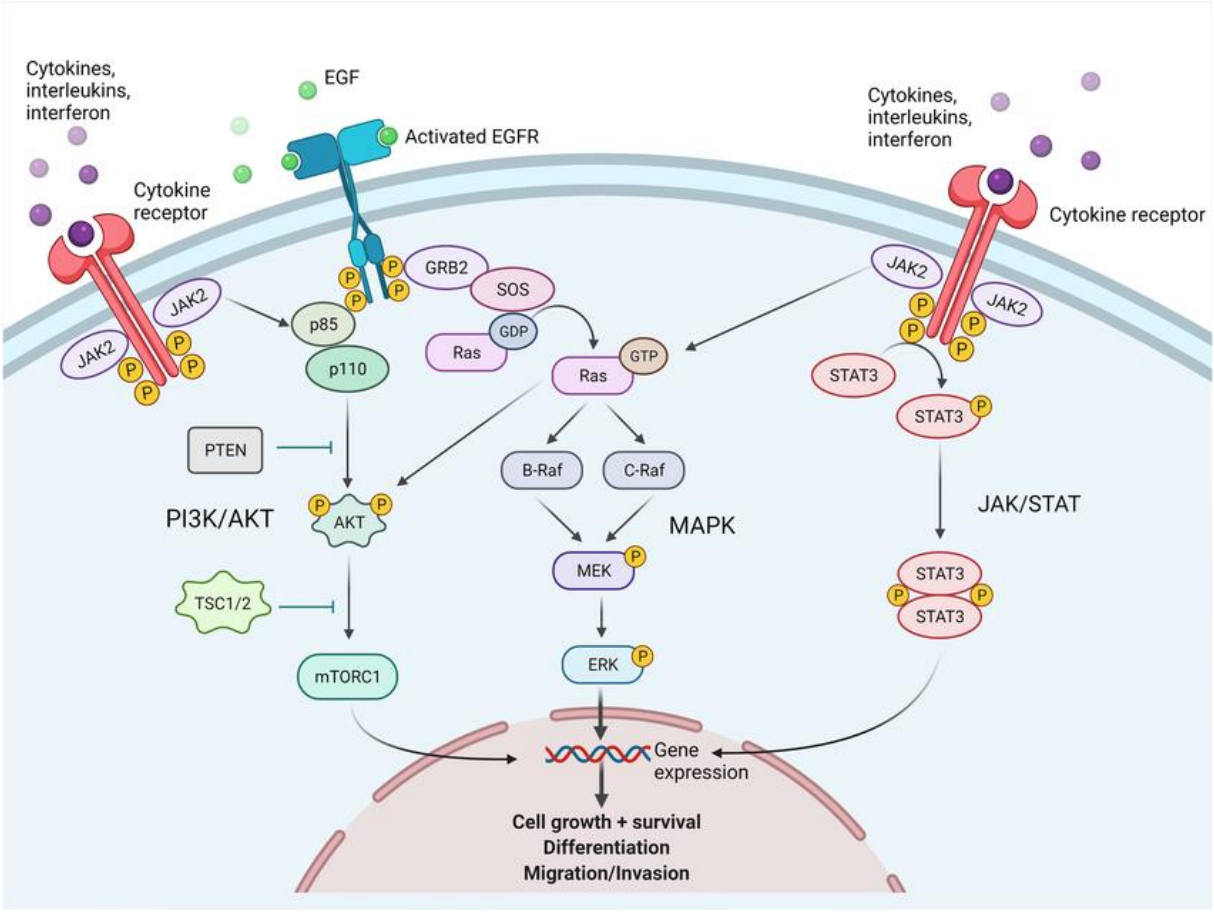

Figure 1.2. Cancerous cells key signal transduction pathway (taken from ref. 7).

Cancerous cells possess somatic mutations in key genes – proto-oncogenes and tumour suppressor genes – that encode proteins that have critical roles in maintaining homeostasis.[7]

Dysregulation or mutations in these genes lead to activation of signal transduction pathways that control cell survival, proliferation and differentiation (Figure 1.2).[4] For example, the mutation found in the catalytic subunit of phosphoinositide 3-kinase (PI3K) isoforms of cancer cells[7,8] resulting in high cell growth and survival of cancerous cells.[8,9] Cancerous cells are also known to disrupt the negative (cell growth) feedback mechanism of normal cells, resulting in accelerated proliferation. This is typically achieved by mutation of the oncogenic Ras GTPase oncoprotein, which normally acts as a negative feedback protein regulating active signal transmission within the cell. Miss-regulation of death receptor signalling by the ubiquitin mechanism is also known to be a feature of some cancer cells.[11]

In addition to accelerating growth, cancer cells also have an ability to evade growth suppressors. They achieve this by inactivation of tumour suppressor genes that normally suppress cellular growth. Typically, cancer cells inactivate the P53 and RB (retinoblastoma-associated) proteins, which normally act as the central control nodes that regulate the apoptosis and senescent signalling of cells.[10,11] This complex behaviour is the root cause of one of the crucial hallmarks of cancer – resistance to programmed cell death.[10,11] Typically, normal aged or damaged cells self-terminate by apoptosis, a natural programmed action where the cell breaks down triggered as a response to physiologic cellular stress/damage. The evasion of growth suppressors can lead to suppression of such apoptotic signalling mechanisms. Cancerous cells also have an ability to reduce the onset of autophagy (an alternative cell survival and death mechanism). Autophagy, as opposed to apoptosis (programmed cell death), is a mechanism by which cells under stress can break down their composite organelles.[12,13] This results in the recycling of the organelles through the formation of autophagosome envelopes (intracellular vesicles occur in the autophagosomes mechanism).[12,13] The autophagosomes then fuse with lysosomes resulting in degradation of the cells.

However, cancer cells can resist this by modification of the Beclin-1 protein, a protein crucial for induction of autophagosome and its delivery to lysosomes. Under normal cell conditions, Beclin-1 binds to Bcl-2/Bcl-xL proteins preventing autophagy.[12] However, when the cells undergo stress, the stress-sensor-coupled BH3 proteins disassociate Beclin-1 from Bcl-2/Bcl-xL proteins, causing the Beclin-1 protein to induce autophagy.[12]

One other mechanism by which tumour cells can sustain their growth is through enabling replicative immortality.[4] This is achieved by extending chromosomal telomeres. The latter are specialist nucleic acid sequences that function to protect the chromosomes from over replication. In normal cells, telomeres are shortened every time the cell undergoes division which leads eventually to senescence/cell death.[14] However, in cancer cells, telomeres are continuously re-extended due to the presence of abnormally activated telomerase.[15] Telomerase is a type of DNA polymerase that extends the telomere by adding repeat segments, leading to cellular immortality. [14]

Cancerous cells/tissues, in the advanced stages, are characterised by their ability to invade neighbouring cells, a process called metastasis. This altered behaviour is due to the loss of E-cadherin, an important protein for cell-to-cell adhesion.[16] The downregulation of E-cadherin in cancer cells alters intercellular attachment and interaction of their extracellular matrix (ECM) components.[16] At the same time, N-cadherin, a protein normally expressed in mesenchymal cells during organogenesis to help the migration of the cells, is upregulated in certain aggressive carcinomas.[16] This overexpression of N-cadherin helps the cancerous cells to lose local cell-to-cell contacts facilitating their ability to migrate to other parts of the body.[16]

The hallmarks of cancer are highly dependent on chromosomal alterations and genetic instability of cancerous cells.[4] Multiple tumour progression pathways can be achieved through

these genome instabilities providing ways for cancerous cells to escape applied current cancer treatments (i.e. the emergence of resistance to previously active anti-cancer agents).[17–19] The inability of cancer cells to maintain their genomic systems and to detect DNA defects and repair them is the most common cause of the increase in the rate of mutations within cancer cells.[17–19]

Interestingly, cancer pathology has revealed that some tumours are able to infiltrate and mediate the immune system allowing them to mirror inflammatory conditions in normal tissues.[20] The immune system, especially the adaptive immune system, has evolved to naturally eradicate tumours. Thus, to escape from this adaptive immune system, tumour cells can develop the ability to mimic normal tissues by producing receptors that only exist there.[21] This aids the cancer in invading surrounding tissues without being detected by immune cells.

Cancer cells have an ability to reprogram their mitochondrial processes, allowing them to increase ATP production. Warburg observed, that in the presence of oxygen, cancer cells prefer to consume glucose to generate energy (ATP) (rather than the normal oxidative phosphorylation of the mitochondria); lactate product of glycolysis acidifies the tumour microenvironment.[22,23] This aerobic glycolysis is now called the 'Warburg effect'.[22–24] This reprogramming of energy metabolism allows excess GLUT1, a glucose transporter, to transport glucose into the cytoplasm of cancer cells. This glucose then can then be used to activate oncogenes (e.g. *MYC*, *RAS*) and sustain cellular growth.[25–27]

External factors, such as non-mutational epigenetic regulation, can also become factors contributing to the development of cancers. Typically, non-mutational epigenetic mechanisms are usually used to mediate embryonic differentiation, development, and organogenesis.[3] However, these capabilities can be exploited by cancer cells enabling direct alteration of the transcriptomic heterogeneity of cancer, further increasing the cancer cell

population.[3] One classic example is that of hypoxia leading to insufficient vascularisation or angiogenesis.[28] Under hypoxia conditions, cancer cells reduce the activity of TET demethylases, changing the methylome to further increase the extent of methylation (hypermethylation).[28] Hypermethylation is the process of over-addition of methyl groups to the cytosines controlling the epigenetic process. This leads to further transcriptional repression typically silencing tumour suppressor genes.[29] Additionally, microbiomes, can also contribute to the development of cancer. Recent studies reveal that polymorphic microbiomes in a population can have an impact on cancer phenotypes.[30,31] It has been shown that such microorganisms (i.e. fungi and bacteria) can affect cancer development, progression, and response to chemotherapy drugs.[30,31]

Aging and senescence are factors that also contribute to the development of cancer.[3] Senescent cells are cells that have stopped their division permanently but have not yet undergone apoptosis. These cells remain metabolically active in the body and may release bioactive substrates such as proteases, chemokines, and cytokines that can harm healthy cells. These bioactive substrates can also promote the growth of cancerous cells through local cell-to-cell communication (i.e. 'paracrine manners' signalling compounds). This type of signalling is thought to contribute strongly in late-stage cancer by promoting angiogenesis, suppressing tumour immunity, as well as stimulation of metastasis.[32,33]

In recent years, researchers have found the existence of cancer stem cells (CSCs) that are able to promote cancer heterogeneity. Such CSCs can promote the growth of new tumours and increase tumour growth sites in the original tissue origin. Originally CSCs were found in mice, as evidenced by their ability to generate a new tumour upon inoculation into previously unaffected recipient mice.[34,35] It has been proposed that CSCs grow from normal tissue stem

cells. CSCs development is then triggered by the formation of primary tumour. This results in the formation of bulk tissues consisting of heterogenous tumour cells.

1.4. Pancreatic cancer

Pancreatic cancer is a leading cause of cancer death worldwide (~3% of all cancer cases) whose incidence has dramatically increased over the last 25 years.[36] This trend is aligned with the risk factors of pancreatic cancer, such as age, genetic factors, and external factors (i.e. smoking, drinking). [36] Because it is often diagnosed late, patients with metastasised pancreatic cancer make up half of those seeking treatment for this cancer. Those already showing tumour-vascular involvement make up another 30-35% of the presenting patient population, with only a minority (<15%) diagnosed with localised tumours that can be removed by surgery.[36] The nature of the patient demographic, who often display advanced cancers, makes the disease difficult to treat especially as the majority of anti-pancreatic cancer drugs tried so far show, at best, modest efficacy.

Pancreatic ductal adenocarcinoma (PDAC) is the most aggressive and lethal of the common cancers, and accounts of 90% of pancreatic cancer cases worldwide.[37] Although general improvements in the cancer therapy have been reported, the overall five-year survival rate of PDAC remains lower than 8%, reflecting the aggressive nature of PDAC.[38] PDAC mostly arises in the head of the pancreas, and this form accounts for 60-70% of all cases of PDAC. [37] This type of PDAC can sometimes be detected in their early stages as it frequently affects the bile duct. The bile duct is a linker that carries bile from the liver and gallbladder to small intestines. The growth of tumour in pancreas head can lead to the obstruction in common bile, leading to the accumulation of bilirubin in the bloodstream, resulting in jaundice. [37] However, the most commonly lethal forms of PDAC are when it arises in the body or tail of pancreas. These types,

in early stages, are frequently asymptomatic making their detection difficult. This leads in part to the poor patient prognosis observed for late discovered pancreatic cancer. The causes of PDAC remain unclear. For example, research shows that iron loss (i.e. anaemia) is common in many pancreatic cancer patients. This occurrence is associated with the mitochondrial metabolism demands of the cancer in ATP production and the generation of reactive oxygen species (ROS).[39] Furthermore, pancreatic cancer-induced inflammation plays a role in elevated hepcidin (HEP) production.[39] This is an iron regulator which leads to changes in ferroprotein (FPN), a key iron transport protein that exports iron from cells when it is demanded elsewhere in the body. [39] This also reduces the absorption of iron in the digestive tract, further elevating iron retention macrophages.[39]

Typical symptoms observed in PDAC patients, include abdominal pain, weight loss, and jaundice.[40] However, some patients also experience thromboembolic disease or the obstruction of blood clotting occurred in blood vessels, as well as well as unexpected onset of type 2 diabetes.[40] Current mainstream therapies for pancreatic cancer are limited to surgery and radiotherapy. Thus far, chemotherapy (such as the antimetabolite gemcitabine) has been shown to have little significant effects on pancreatic cancer. Furthermore, recent more advanced approaches, such as anti-body therapy targeting molecular pathways, have also been shown to have little effect on pancreatic cancer.[41] These results are thought to be due to the rapidity by which PDAC can acquire resistance to many agents' making pancreatic cancer very challenging to treat.[41]

The therapy of pancreatic cancer, particularly PDAC, remains a major challenge, with only early surgical intervention having reliable treatment outcomes. However, only 15–20% of patients are eligible at diagnosis due to late-stage detection of pancreatic cancer being common.[38] For most of patients with unresectable or metastatic PDAC, palliative

chemotherapy is the standard of care. Current chemotherapy treatments include gemcitabine; an antimetabolite chemotherapy drug combined with nab-paclitaxel have shown some improvement in survival rates of PDAC patients as compared with gemcitabine alone. However, the overall patient survival rate for this gemcitabine combination treatment remains unacceptably low (less than one year on average).[42,43] Presently only radiotherapy and chemotherapy combined with radiation are used in the treatment of late stage PDAC.[44] However, the overall survival rate is still poor and the cytotoxicity of radiotherapy towards normal cells is problematic and can be fatal in some cases.[44] Consequently, despite these incremental improvements in treatment, PDAC remains one of the hardest cancers to treat.[36] Overall survival outcomes remain low when compared to other types of cancer.[36] Thus, there is a need for the discovery of new treatment agents that can kill, or at least prevent onward growth of PDAC, increasing the overall survival rates/life expectancy/quality of life of patients.

1.5. Colorectal cancer

The large human intestine is divided into three major parts: the anal canal, colon, and rectum. If cellular mutation occurs in the colon and/or rectum this leads to colorectal cancer (CRC). This cancer is the third most diagnosed form globally, and the second most common cause of cancer mortality worldwide.[45] The exact aetiology (onset) causes of colorectal cancer remain largely unknown. However, several factors are known to contribute to CRC: genetics, dietary factors, carcinogenic exposure, and coexisting non-cancerous conditions (especially colorectal polyps, Crohn's disease, or ulcerative colitis).[46,47] This makes CRC is a multi-factorial disease and it is hard to predict which patient groups are the most at risk.

CRC can arise from hyperplasia of the epithelial cells in the colorectal mucosa, atypical hyperplasia, or adenoma, which can all be initiated by exposure to the carcinogenic factors

mentioned above.[48] Such exposure can lead to changes in the structure of the cellular DNA, transforming normal cells into malignant phenotypes. It has been shown that there are three major molecular mechanisms responsible for the onset of CRC: (i) the development of chromosomal instability, (ii) genetic mutation [specifically of the cell's DNA mismatch repair (MMR) that corrects errors in daughter DNA strands during their replication], and (iii) CpG island hypermethylation.[48] In the latter, methylation triggers deamination reactions of cytosine-phosphate-guanine resulting in increased mutation rates. These three mechanisms are associated with alteration of multiple genes such as *c-MYC, K-Ras, P53*, and MMR-associated genes (*hMLH1, hMLH3, hMSH2, hMSH3, hMSH6, hPMS1, and hPMS2*).[48] Moreover, these multiple genetic alterations and associated molecular pathways typically overlap with each other leading to the increased rate of the disease progression seen in some patients with CRC.

1.6. Breast cancer

A malignancy originating in the breast, breast cancer is the most common cancer diagnosed in woman worldwide and the 5th leading cause of cancer death globally.[49] It is estimated that in 2020 new cases of breast cancer amounted to more than 2 million cases, with a worrying increase in death rates due to recent changes in risk (lifestyle)s and poorer cancer detection, especially in the developing world.[49] Breast cancer mostly occurs due to genetic mutations. Two major genes are specifically linked to the occurrence of breast cancer: *BRCA1* and *BRCA2*. The mutation(s) present in these genes is often inherited in an autosomal dominant manner. Breast cancer can be classified into four subtypes based on its mRNA gene expression level: Luminal A, Luminal B, HER2-enriched, and basal-like breast cancer. Patient diagnosis of one of these subtypes can provide better information on the most appropriate treatment strategies

and management of breast cancer patients. Luminal A breast cancer is distinguished by of the involvement of oestrogen and progesterone receptors (ER and PR respectively) in the liminal epithelium lining in the mammary duct which hare associated with mammary development, growth, and function.[50] This type of breast cancer also involves the human epidermal growth factor 2 receptor (HER2) an epidermal growth factor receptor that plays a role in normal cell growth and differentiation.[50] On the other hand, luminal B breast cancer has a better prognosis than luminal A breast cancer even though HER2 is involved. Luminal B cancers also have high expression of proliferative/relation genes and lower expression of PR in luminal epithelium.[51] While luminal breast cancers are characterised by the presence of ER and/or PR proteins, HER-2 enriched breast cancer is characterised by the presence of HER2, and the absence of ER and PR.[52] HER2-enriched breast cancer grows faster due to the expression of proliferation related genes such as ERBB2/HER2 and GRB7.[52] This can make its treatment challenging. Finally, the most common type of breast cancer (accounting for 20% of all breast cancer cases) is basal-like/triple-negative breast cancer (TNBC). TNBC is identified by a HER2-negative, ER-negative, and PR-negative status, and it too has an aggressive nature leading to a poor patient prognosis. TNBC has the highest BRCA1 mutation rate, accounting for approximately 80% in all TNBC cases. Due to the heterogeneity profile of TNBC, it can be differentiated into six further subtypes based on the gene expression profiling: basal-like (BL1 and BL2), mesenchymal (M), mesenchymal stem-like (MSL), immunomodulatory (IM), luminal androgen receptor (LAR), and an unspecified group (UNS).[53] Presently, it is not easy to treat TNBC because of lack of receptors to target, and deciding on suitable treatments for TNBC is complicated by its range of sub-types.

Based on the fact that breast cancer covers such a wide range of types/subtypes researchers have sought biomarkers that can help detect the presence of specific breast cancer types.

Some biomarkers are useful for diagnosis purposes, such as ER or PR, and changes to HER3. ER is important in the diagnosis of breast cancer because an associated significantly enhanced ER receptor, found in 75% of all invasive breast carcinomas informs treatment strategies.[54] PR, on the other hand, is over expressed typically in patients with ER-positive breast cancer.[55] This is because the expression of PR is itself determined by the expression level of the ER.[55] Therefore, ER and PR levels are highly correlated to each other in breast cancer tissues. The expression of HER2 is useful in the early detection of breast carcinogenesis, making it a promising biomarker for breast cancer and molecular target for therapy.[56]

The most common type of breast cancer (accounting for 20% of all breast cancer cases) is basal-like/triple-negative breast cancer (TNBC). TNBC is identified by a HER2-negative, ER-negative, and PR-negative status, and it too has an aggressive nature leading to a poor patient prognosis. TNBC has the highest BRCA1 mutation rate, accounting for approximately 80% in all TNBC cases. Due to the heterogeneity profile of TNBC, it can be differentiated into six further subtypes based on the gene expression profiling: basal-like (BL1 and BL2), mesenchymal (M), mesenchymal stem-like (MSL), immunomodulatory (IM), luminal androgen receptor (LAR), and an unspecified group (UNS).[53] Presently, it is not easy to treat TNBC because of lack of receptors to target, and deciding on suitable treatments for TNBC is complicated by its range of sub-types.

1.7. Front-line metal-based cancer treatments: cisplatin

Metal-based cancer treatments use metal-containing compound to either limit the growth of cancer cells or eliminate them completely via cytotoxic effects. Cisplatin (*cis*-diamminedichloro-platinum (II)) (**1.1**, Scheme 1.1), discovered serendipitously, is the most

famous metal-based therapy with high efficacy towards a wide range of cancer types (including colon and breast cancers).[57]

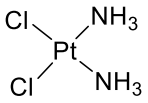

(**1.1**)

Scheme 1.1. Structure of Cisplatin (**1.1**).

Cisplatin's activity was found by Barnett Rosenberg in 1965 during attempted studies of electrical field effects on the growth of *E. coli*.[58] During this research, cisplatin was accidently formed *in situ* but later discovered in the growth media. Subsequently independently synthesised cisplatin was tested against testicular cancer with hugely positive outcomes.[59,60] This led to cisplatin becoming a major front-line cancer treatment for testicular germ-cell cancer and used as first-line regimens for the treatment of other cancers. For example, head and neck squamous cell carcinomas are susceptible to a combination of cisplatin and 5-fluorouracil leading to overall survival rates and reduced risk of recurrence.[61] Similarly, a combination of cisplatin and gemcitabine has become a major frontline therapy for a range of cancers including: metastatic urothelial carcinoma, non–small cell lung cancer, and metastatic biliary tract cancer.[62–64] Such combination therapies are effective and frequently improve overall survival, the tumour response towards therapy rate, and progression-free survival. Such combination approaches have led to interest in the discovery of other metal-based therapies (platinum based and other metals) for such approaches.

The activity of cisplatin is mediated by the interaction of cisplatin with DNA, which creates DNA lesions that inhibit DNA transcription and replication processes.[57] To do this cisplatin must first enter the cell and be converted to its active form (Figure 1.3).

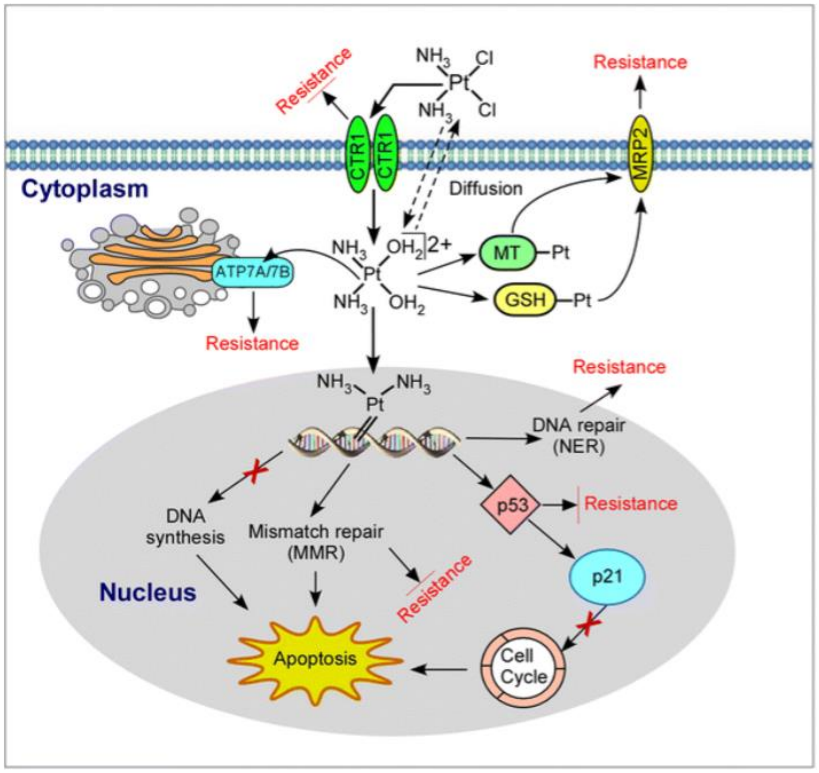

Figure 1.3. Cisplatin mechanism of action inside the targeted cancer cells. (taken from ref. 66).

Cisplatin can enter the cell by two different mechanisms: simple passive diffusion, or more commonly, by using active membrane transporters (i.e. the copper transport protein CTR-1, which in normal action provides the cell with copper needed, for example, in cytochrome c oxidase). After entering the cell, cisplatin is hydrolysed and its two anionic chloride ligands are replaced by neutral water ligands. This exchange makes cisplatin into its active Lewis acidic form *cis*-$[Pt(OH_2)_2(NH_3)_2]^{2+}$.[65] In this form cisplatin can easily form covalent (coordinative) bonds with the N7 position of adenine and guanine DNA bases and this leads to crosslinking of the DNA.[65] The crosslinking of the DNA happened because platinum is bind to the N7 atom of purine bases of the DNA.[66] The major product of DNA adducts formed by cisplatin were 1,2-intrastrand cross-links involving adjacent bases (Figure 1.4), where *cis*-$[Pt(NH_3)_2\{d(GpG)\}]$ (*cis*-GG) account for 47−50% of the adducts formed and *cis*-$[Pt(NH_3)_2\{d(ApG)\}]$ (*cis*-AG) another 23−28%.[66] Furthermore, 1,3-intrastrand crosslinks compelling interstrand adducts and

nonadjacent guanines (*cis*-GNG) account for 8-10% of the adducts formed.[66] The crosslinking of the DNA and cisplatin resulting in inability of the cells to complete DNA synthesis, causing cell cycle arrest (in the S phase) to facilitate DNA repair, or failing that, triggering programmed cell death.

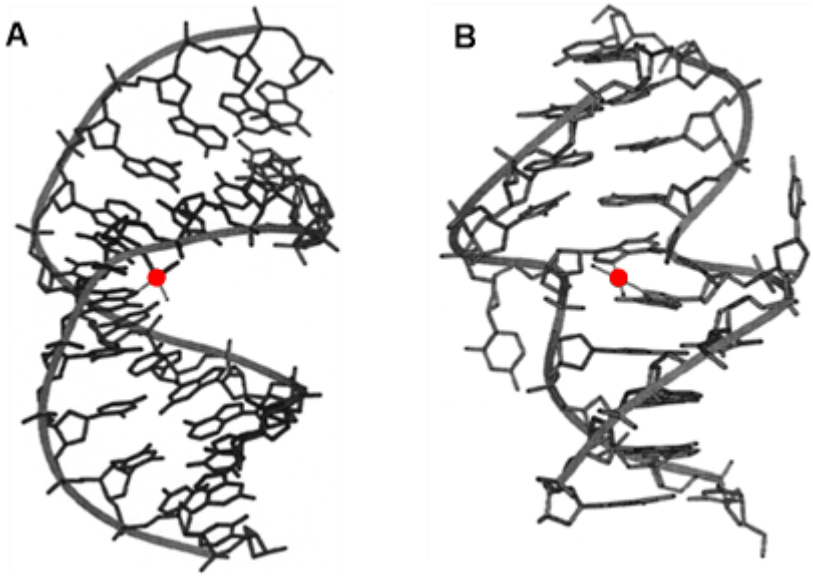

Figure 1.4. Typical crosslink motifs resulting from interaction of cisplatin with DNA. (A) 1,2-intrastrand G…G cisplatin adduct. (B) Interstrand DNA G…G crosslinking by cisplatin. The platinum atom of the $[Pt(NH_3)_2]^{2+}$ unit is shown in red. The X-ray and NMR derived structures are taken from ref. 66.

In response to cisplatin treatment, some cancer cells can create mechanisms to repair the damage induced by cisplatin. These outcomes create resistance or "unresponsive mechanism responses" towards cisplatin treatment. Breast cancer and colorectal cancer, specifically, have been shown to become unresponsive to cisplatin upon prolonged exposure. Several mechanisms have been shown to create such resistance including: alteration in DNA repair mechanisms (i.e. DNA mismatch repair and nucleotide excision repair), alteration in signal transduction pathway, enhancement of drug detoxification by metallothionein and glutathione, and downregulation of the cooper transporter resulting in reduced drug

accumulation.[67,68] These resistance mechanisms are a cell line and mutation dependent, meaning that a particular tumour can develop one or more resistance mechanism. The emergence of resistance in cisplatin treated patients is a big problem and there is a clear need to find alternative metal-based cancer treatments that overcome, or are at least less susceptible, to such problems. While significant advances have been made with improved platinum-based agents (e.g. carboplatin, oxaliplatin, nedaplatin)[69,70] the underlying problems of resistance and toxicity remain. Recent work on ruthenium-based complexes has led to agents that have entered clinical trial (e.g. NAMI-A, KP1019, BOLD-100, TLD-1433).[71–73] Some of these show promising results, but they are not yet established as widespread medicines. This is because ruthenium-based complex has mechanism of action towards the inhibition of tumour migration and activate stress response protein (i.e. GRP78) to induce immunogenic cell death. [71–73] However, it has strong binding to albumin resulting in long tissue retention. There is a need to further the scope of low toxicity metal-based therapeutic agents. Titanium-based agents are thought to be one such possibility as the emergence of resistance is not documented in any trial of this type of metal-based therapy.

1.8. The genesis of titanium-based complexes as metal-based cancer treatment agents

The only non-cisplatin (or derivatives thereof) metal-based therapies that have reached clinical trials in the last 40 years are based on titanium. The first generation of titanium species used as metal-based chemotherapy agents were *bis*(cyclopentadienide) titanium dichloride (Cp_2TiCl_2, titanocene dichloride) **1.2**, and *cis*-diethoxy*bis*(1-phenylbutane-1,3-dionato) titanium(IV) [$(bzac)_2Ti(OEt)_2$, budotitane, **1.3**] (Scheme 1.2). Both compounds appeared to have promising effects towards cancer in the period 1979-1985 and later reached Phase I clinical trials.

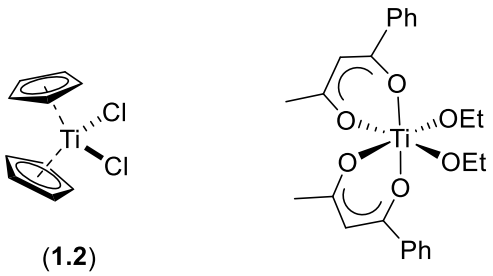

(**1.2**) (**1.3**)

Scheme 1.2. Structures of titanocene dichloride (**1.2**) and budotitane (**1.3**).

Compound **1.2** was first discovered to have high cytotoxicity against the mouse cancer *Ehrlich ascites tumours* (EAT). When administered into EAT infected mice, compound **1.2** is highly effective (up to 100% cure rates) and shows little metal toxicity when compared to cisplatin. Based on the presence of a '$TiCl_2$' unit alone, Köpf-Maier proposed that **1.2** has a similar DNA-binding ability to cisplatin. To prove this hypothesis, electron energy loss spectroscopy (EELS) was applied and DNA-titanocene binding seemed to be supported as the titanium concentration was maximised at the nucleus.[74] However, the weak signal-to-noise ratio in these early experiments required use of high concentrations of the complex (up to 10 mM). Although these conditions suggested association of **1.2** with cellular nucleic acids, the possibility of artefacts or contamination (i.e. no DNA binding) could not be excluded. Subsequently, X-ray fluorescence analysis was used as an alternative method to probe possible titanium–DNA interactions within cells.[74] These investigations showed that **1.2** has a mode of action distinct from cisplatin, and the primary target of such species is not solely DNA, but potentially includes a wider range of alternative targets (see later).[75] Although initially assumed to have a mechanism of action akin to cisplatin, the hydrolysis of **1.2** dichloride does not lead to $[Cp_2Ti(OH_2)_2]^{2+}$ and is in fact highly complex leading to the formation of insoluble aggregates in aqueous solution, which further react with water to form TiO_2 due to the highly oxophilic characteristics of titanium(IV). Analysis of **1.2** dichloride in water by ^{1}H NMR

spectroscopy, across a broad range of pH levels, shows that both chloro groups are completely hydrolysed with a $t_{1/2}$ of 50 minutes (leading to $[Cp_2Ti(OH)(OH_2)]^+$. Subsequently, the cyclopentadienyl (Cp) ligands are hydrolysed after, with a $t_{1/2}$ of 54 hours (leading to a complex array of poorly characterised products).

Similarly, the anticancer properties of **1.3** were determined in 1982, when this agent was tested against animal malignancies (i.e. colon tumours and EAT). During mechanistic investigation of the hydrolysis of **1.3**, the complex was added to distilled water. This produced a suspension from which **1.3** could be recovered intact.[76–78] However, the rate of the hydrolysis of solutions of **1.3** is dramatically increased in the presence of acetonitrile or methanol co-solvents. The diketonato ligands of **1.3** in acetonitrile/water are completely hydrolysed within 2.5 hours. Under these conditions the half-life of ethoxy groups in water/co-solvent mixtures is even more transitory: solvolysis was calculated with a $t_{1/2}$ of 20 seconds.[79] Furthermore, study of complex **1.3** showed it is isolated as a *cis* isomer. Molecular modelling (MM3) suggested that steric reasons lead to **1.3** being isolated as a *cis* isomer.[78]

Although both **1.2** and **1.3** had limited phase II clinical trials, neither compound progressed further due to poor efficacy in human subjects and associated toxicity issues with their formulations. Due to these challenges contemporary researchers have new titanium complexes that are much more stable to hydrolytic conditions and with much higher activity *in vitro*, raising the potential for *in vivo* human efficacy. Key points of the development of this area are discussed in the next section; further details can be found in a recent review.[74]

1.8.1. Titanium anti-cancer agents containing phenolate-based ligands

A second generation of titanium-based anti-cancer complexes was introduced in 2007 by Tshuva, using phenolato chelating polydentate ligands with oxygen-nitrogen-nitrogen-oxygen

(ONNO) ligand donor sets. These titanium complexes are much more stable under the aqueous biological environments.[80] This is due to the presence of chelate amine-*bis*(phenolato) donor sets in the titanium complexes. The alkoxide donors also help improve complex stability due to the strong covalent bonds formed at the oxophilic titanium(IV) centre.[81] The connectivity of N-O binding also allows the utilisation of a variety of bonding modes and alternate branching motifs that can be used to further stabilise the structure of such titanium complexes. The first group of phenolato titanium (IV) complexes developed as anti-cancer agents were the so called 'salan' compounds that have donor sets based on diamine-amine-*bis*(phenolato) cores (**1.4a-c**, Scheme 1.3).[79] To engender biological activity Tshuva chose to include two labile *cis*-alkoxo ligands (most often O-*i*Pr), presumably by analogy to the structure of budotitane (**1.3**).

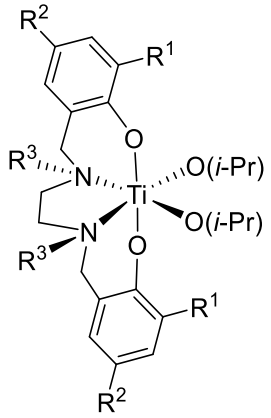

(**1.4a-c**)

(**1.4**)	R^1	R^2	R^3
a	*t*-Bu	*t*-Bu	Me
b	Me	Me	Me
c	H	Me	Me

Scheme 1.3. Tshuva's Salan Ti(IV) complexes featuring *cis*-*bis*(isopropoxide)Ti(IV) units (**1.4a-c**) that have been tested in HT29 and OVCAR-1 cancer cell lines. [82]

Tshuva and colleagues have worked extensively with amino-phenolate ligands,[81] often targeting titanium complexes via tetradentate [ONNO] ligand sets providing [ONNO]-TiX_2 complexes (salan complexes), where X is an easily hydrolysed ligand (e.g. the O-*i*-Pr groups in Scheme 1.3). These pendant phenoxy groups are easily modified allowing investigation of how

ligand structure changes the hydrolytic stability of the derived titanium complexes.[81,83] This type of titanium complex has several potential advantages. The octahedral geometry at titanium(IV) centre leads to neutral complexes that could facilitate passive diffusion into cells. Additionally, they favour stable *cis* configurations. Tshuva *et al.* have synthesised *cis*-*bis*(isopropoxide)Ti(IV) complexes of structure (**1.4**) and tested them against many types of cancer cell lines including: HT-29 (colon cancer) and OVCAR-1 (ovarian cancer) demonstrating, in many cases, appealing anti-tumour activity levels.[82] The complexes **1.4** contain various diamine *bis*(phenolato) ligands (Scheme 1.3), and substituent modifications within the ligand lead to different biological activities. For example, complex **1.4a** shows no detectable cytotoxicity towards both HT-29 and OVCAR-1 cells, while **1.4b** shows some cytotoxicity in both cell lines (HT-29 IC_{50} of 12±1 µM and OVCAR-1 IC_{50} of 14±1 µM.[82]

In a related publication, Abid and co-workers showed the high activity *bis*-phenolato Ti(IV) complex (with similar ONO ligand sets) against various cancerous cell lines (Scheme 1.4).[84] He determined an initial structure activity relationship (SAR) for various different ligands attached to his complex using biological assays (mainly MTT) to determine their growth inhibitory and cytotoxicity properties. Some information on the mechanism of action of these Ti(IV) complexes was also determined.

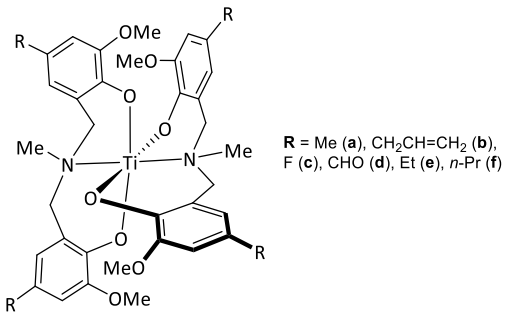

Scheme 1.4. Lead compounds reported by Abid et al. See also structures (**2.1a-f**) in Chapter 2.

The complexes of Abid *et al*. trigger apoptosis, as shown by flow cytometry using dual staining annexin-V propidium iodide and, γ-H2AX assays, supported by caspase activation studies.[84] Abid *et al.* found that **2.1** complexes are able to create cell cycle arrest, due to the accumulation of the complex in the G2/M phase.[84] Furthermore, **2.1a-c** demonstrates high selectivity and cytotoxicity towards a wide range of cancer cell lines, with GI_{50} < 10 μM in most of cancer cell lines. For example, MCF-7 breast cancer is rather sensitive to **2.1a** showing a GI_{50} of 1.0±0.04 μM. Pleasingly it is significantly less active against non-cancerous cells, e.g. normal MRC-5 lung fibroblasts reveal a GI_{50} value of 7.3 μM, i.e. **2.1a** is 7-fold less active in the normal cell line vs. MCF-7.[84]

To support the finding of Abid, Musa *et al.* tested these compound's cellular behaviour to further help define their mechanism of action in cancer cell lines. In his research, he showed that compounds of the **2.1** class are able to block the G2/M, leading to cell death in colon cancer HCT-116 and MCF-7 breast cell lines.[85] These Ti(IV) complexes also downregulate the expression of ERK1/2 MAP kinase signal transduction and the survival proteins Bcl-2 and Mcl-

1 resulting in membrane blebbing and chromatin condensation, further promoting nuclear fragmentation and cell death. [85] Musa's studies are consistent with the target of such Ti(IV) complexes being the mitochondria, in line with the work of Tshuva. [85] However, Abid, Musa and co-workers did not extensively test their Ti(IV) complexes against pancreatic cancer 2D or 3D-models disease, which is the aim of investigations in this work. We also planned to use a transferrin receptor (TfR1)-targeted delivery vector – apoferritin (AFt) - to deliver **2.1** to cancer cells.

1.8.2. Sadler hypothesis of titanocene-transferrin interactions

Based on the section above, it has been suggested that **1.2** has some potency against cancer cells. However, Waern *et al.* showed that use of **1.2** results in no substantial Ti-uptake when V79 hamster lung cells are treated with 100 µM solutions of titanocene dichloride (**1.2**). Thus, Sadler suggested an alternative mechanism to transport the 'Ti^{4+}' into cells using transferrin proteins. He proposed that apo-transferrin can rapidly transfer **1.2**, by its conversion to Ti^{4+} under physiological conditions, due to the rapid hydrolysis of its chloride and cyclopentadienyl ligands (resulting in some form of (undefined) 'naked Ti^{4+}' (Scheme 1.5). This suggestion is supported by the model NMR investigation showing that Tf metal-adducts exhibited structural changes, making a stable Ti-Tf species after the insertion of Ti^{4+} into the cage (although the nature of that species has never been explicitly defined). This Ti-Tf complex is transported into the cell through endosomes, and subsequent release of 'Ti^{4+}' ions is proposed to be facilitated by binding of the 'Ti^{4+}' with adenosine triphosphate (ATP), making the titanium able to transfer to DNA or RNA (Scheme 1.5). However, there is no *direct* spectroscopic evidence to support this hypothesis and it is now regarded with some scepticism, although it did provide us with

the idea that encapsulation of **2.1a** in AFt (iron-free ferritin), instead of transferrin, might be viable.

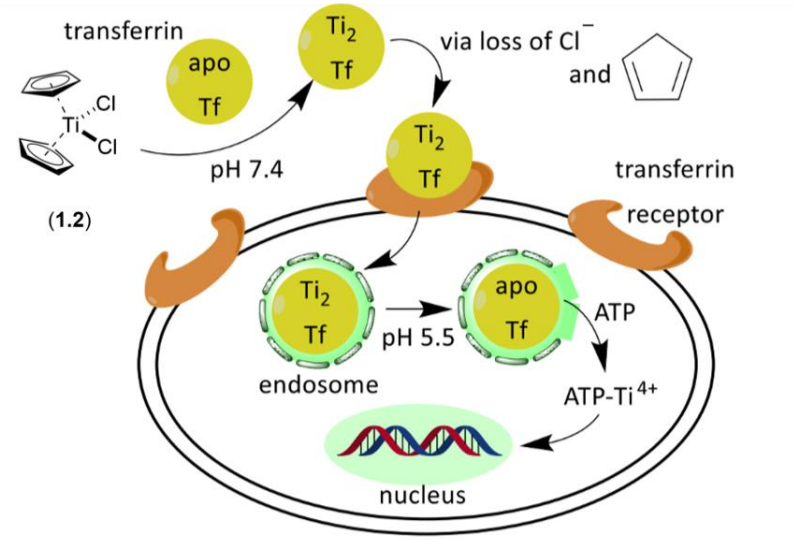

Scheme 1.5. The uptake of titanium from titanocene dichloride (**1.2**) by transferrin protein and the mechanism of its release as proposed by Sadler.[86]

We were further encouraged in our own proposal by the work of Tshuva *et al*. who has recently used the highly stable Ti(IV) complex (**1.5**, Scheme 1.6) to allow embedding with organic nanoparticles via evaporation from microemulsions. Tshuva showed that **1.5**, once embedded within these nanoparticles, shows very high anti-proliferative activity towards the A2780 ovarian cancer cell line, demonstrating encapsulation-based increase in its activity towards cancer cells. [87]

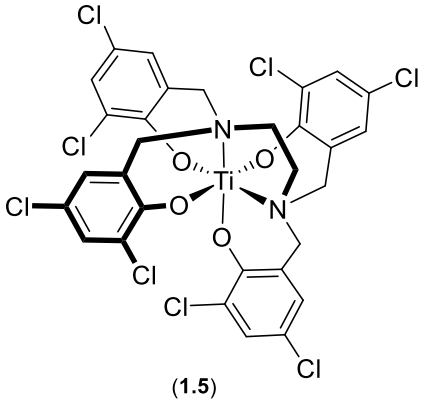

(**1.5**)

Scheme 1.6. The structure of Tshuva's complex (**1.5**).

1.9. Drug carriers and nanoencapsulation

The application of nanotechnology in biomedical science continues to evolve rapidly to cover chemical sensing, biological imaging, and drug delivery applications.[88] Nanocarriers can have suitable pharmacokinetics and high cell permeability for delivering drug molecules into targeted cells, enhancing the drug delivery system. A wide range of synthetic carriers (i.e. micelles, carbon nanotubes, dendrimers, polymers) have been developed for applications to increase the efficiency of drug delivery.[88] However, it is important to note that in such applications there are often practical limits most commonly associated with low drug delivery efficiency and/or acute toxicity associated with the carrier at high doses. Thus, nowadays, researchers have been putting greater emphasis on the use of natural nanocarriers, due to their biocompatibility, low toxicity, and high cellular uptake.[88] Natural nanocarriers include viruses, ferritin, and other proteins that facilitate self-assembly of supramolecular structures. This route has frequently become the best choice when delivering drugs into target cells.

The natural nanocarriers used should lack toxicity, be non-carcinogenic, and not have immunogenic effects.[88] Additionally, the carrier should have a long-life span in the host cells to ensure effective dose delivery of the drug cargo. To ensure this requirement is met, ideally,

the half-life of release of the carried drug should be measured before biological studies. Natural nanocarriers need also to realise effective loadings and have controllable release mechanisms for disembarking their carried drugs from the natural carrier.[88] This factor is frequently dependent on carrier conformational changes, its chemical immobilisation, and non-covalent interactions of the cage carrier with its environment.[89] One of the most used natural carriers are, protein-based nanocages, they can be chemically conjugated with a specific therapeutic agent by post-translational attachment of the agent to reactive side chains of amino acids (i.e. amines, hydroxyl, carboxyl or sulfhydryl functions) on appropriate side chains. [88] These covalent conjugations can control/trigger the kinetic release of the drug cargo, this can be modified based on the conjugation associated with the nanocage and the environment the cage is in.[88] The interior cavity of most protein-based nanocages have reactive sites which are suited to interaction with a range of agents (i.e. drugs, metals, nucleic acids etc.) which increase the binding affinity of the cage to the drug guest. Natural nanocarriers that have a specific target also clearly enhance the therapeutic potential of suitably matched target drug agents. For example, nanocarriers for cancer therapy agents will be highly favoured if they accumulate in the tumour microenvironment (TME) by enhancement of permeation and retention effects (EPR).[88] EPR is facilitated by the chaotic, porous tumour vasculature and poor lymphatic drainage often observed in the TME. To further increase tumour cell affinities, targeting ligands may be attached to the delivering nanocage. For example, to target the transferrin receptor, which is present abundantly on malignant cells, the carrier should present a specific target site that can bind with transferrin receptors.[90] All of the above factors contribute to the selectivity and activity of drugs delivered by nanocarriers, but optimising and balancing these needs is still a rather empirical process.[88]

As we proposed to use apoferritin as our preferred nano carrier this is discussed in detail in the next two sections.

1.10. Transferrin Receptor 1 and Transferrin: protein associated with iron regulation

The transferrin receptor 1 (TfR-1) is a type II transmembrane glycoprotein that binds with transferrin and have a critical function in iron uptake. [90] A schematic of its mechanism of action is shown below in Figure 1.5. TfR-1 has a molecular mass of 90 kDa and 760 amino acids. The overall protein is linked with disulfide bonds to the cell surface. TfR-1 can bind with two transferrin molecules, with binding affinity (K_d) at pH 7.4 of 4 nM for diferric transferrin and 30 nM for monoferric transferrin. [90]

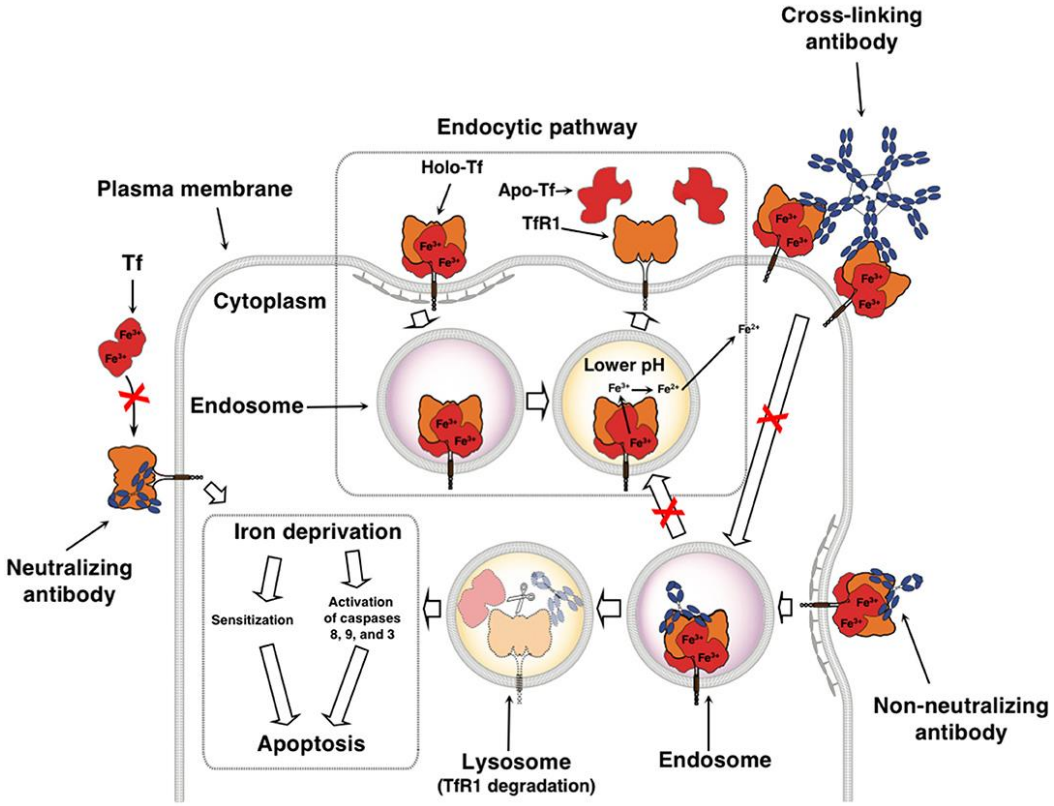

Figure 1.5. Mechanism of transferrin (TfR-1) binding and the release of iron ion to the cells.

Taken from ref. 92

In normal cells, TfR-1 is only expressed at low level,[91] however, a greatly increased level of expression of TfR-1 is associated with high proliferation cells and malignant cells due to their increased iron needs. Increased expression of TfR-1 is associated with advanced cancers states in nearly all cases, making it a universal cancer marker.[92] Most genes responsible for TfR-1 expression also have roles related to cancer progression. One example gene is *c-MYC*, a proto-oncogene that, as a carcinogenic oncogene, is responsible for cancer proliferation which shows a tight regulation linkage to *TFRC* the gene encoded for TfR-1 expression. This is thought to be achieved by binding to the E box binding site in intron 1 of *TFRC*.[93] The overexpression of TfR-1 also makes cancer cells susceptible to iron deprivation, leading to its depletion in healthy tissues/cells. It has also been found that increased intracellular iron in cancer cells protects them by reducing natural killer (specifically NK92MI) cell activity.[94] The TfR-1 receptor (like many others that are over expressed in cancer) has been found to activate the transcription of genes driving immunity, inflammation, cell survival, and proliferation. Specifically, in malignant cells inhibition of the NF-κB kinase (IKK) complex, further increased cancer cell survival.[95] These observations make TfR-1 a suitable target for cancer therapy agents.

Transferrin itself is a monomeric glycoprotein with a molecular weight of 80 kDa that is found mainly in blood serum and cerebrospinal fluid.[90] It plays at central role in iron transport of Fe(III) to the liver, bone marrow, and spleen.[90] Transferrin consists of two globular lobes at the C and N termini between which is the iron binding site. [90] Iron binding typically requires the presence of a carbonate anion. Finally, the two transferrin lobes each have two further subdomains that function as 'opening gates' to release iron at the target.[90]

Iron-free transferrin is also referred to as apo-transferrin.[90] This has the ability to undergo conformational change promoting binding with ferric ions. Transferrin has a maximum binding

capacity, of two ferric ions (Fe^{3+}).[90] In binding the second ferric ion, the carbonate co-ligand plays an electrostatic role opposing the otherwise repulsive charge that would build up at the binding site.[90] Although they are archetypal iron carriers transferrin can also have other biological activities including: prevention of the formation of ROS species, impeding bacterial survival by iron binding, delivering macrophages to tissue, and finally as marker of inflammation.[90] Transferrin has also been used as a carrier for drug delivery system, especially in cancer therapy. For example, a study by Jain showed that transferrin can be used as a nanocarrier for anti-brain cancer agents allowing penetration of the blood brain barrier (BBB) and targeting glioblastoma multiforme (GBM) cells.[96]

However, there are challenges still to be overcome in widespread use of transferrin. One major limitation is the stability of transferrin and another is the avoidance of immunological responses. The transferrin protein is stable under the blood serum condition (pH 7.4, 100 mM NaCl).[90] However, it easily aggregates undergoing opsonisation (immune tagging), leading to phagocytosis (absorption) or under non serum conditions hydrolytic degradation. Modified transferrin proteins are also recognised by the immune system, leading to equivalent immune/phagocytosis responses.[90] One way to overcome these issues is to use ferritin, an iron storage iron protein that can also be used as a nanocage protein carrier.

1.11. Ferritin and apoferritin: a nanocage for drug loading

Ferritin is a large 450 kDa protein also involved in iron metabolism, specifically as an iron storage system for the body.[97] The protein is large (12 nm diameter), hollow (inner core 8 nm diameter) and composed of 24 sub-units (Figure 1.6).[97] It stores, transports and delivers iron in a controlled manner to mammalian cells. Nature uses this transport protein as free aqueous (serum) Fe^{2+}/Fe^{3+} species are too Lewis acidic and thus are highly toxic to cells.[97] Ferritin

consists of two subunit types referred to as the heavy (FTH1, 21 kDa) and light (FTL, 19 kDa) chains.[98] The subunits are encoded by different genes, and the ratio of the expressed proteins (isoferritins) results in tissue specific distributions and properties. FTH1 is highly expressed in the heart and also leads to ferroxidase activity, in which Fe^{2+} is oxidised to Fe^{3+} and subsequently stored the ferritin.[97] On the other hand, FTL which is expressed more in the liver, shows increased iron nucleation sites, spaces to store iron, improving iron uptake and storage system.[97] Conversion of Fe^{2+} into Fe^{3+} has advantages, as inclusion of Fe^{3+} into ferritin protects nucleic acids, proteins, and lipids from reactive oxygen species (ROS) that that are more easily triggered by iron(II) species via the Fenton reaction between Fe^{2+} and serum H_2O_2.[97] Avoiding this is crucial for cell survival as high ROS levels lead to cell death. Ferritin can store ~2000 Fe^{3+} ions in its normal physiological state.[97] However, if the cavity is suitably activated this can be increased to ca. 4500 Fe^{3+}.[97] The Fe^{3+} entering the ferritin form ferric hydroxide-phosphate ($5Fe_2O_3 \cdot 9H_2O$), which forms the core of the iron stored in ferritin.[97] This process is required because it prevents radical formation, ensuring iron ion is safe for released into the cells under reductive conditions, and provides a bioavailable, stable, and soluble iron reservoir for the body.[97]

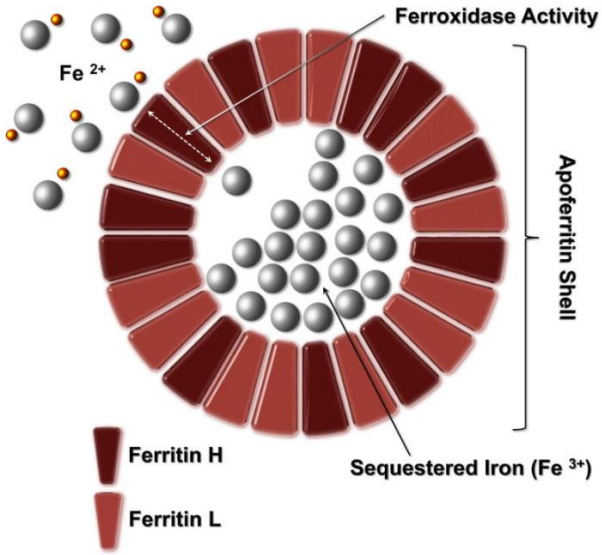

Figure 1.6. Schematic representation of the ferritin protein structure. Taken from ref. 98.

Despite it is function as an iron storage system, several studies already suggest that ferritin can be used as an effective drug delivery system.[99] Ferritin nanocarriers are potentially ideally suited to cancer chemotherapy as they are predisposed to target TfR-1 receptors, which are overexpressed in tumour cells, potentially allowing for selective and efficient delivery.[99] Human heavy chain ferritin (HFn) has the ability to enter tumour cells through interaction with TfR-1 using receptor-mediated internalisation (see Figure 1.3 earlier). This selective deliver offers potential to increase the effectiveness of chemotherapeutic drugs, making ferritin a highly popular contemporary protein nanocarrier.[99] Furthermore, ferritin is much more stable that transferrin: it may be handled at higher temperature (up to 80 °C for 10 minutes). This can be useful if, for example, inclusion of the proposed drug cargo into the apo-ferritin is sluggish.[99]

Upon removal of all the iron from ferritin, a hollow protein shell is obtained, normally called apoferritin.[100] This protein has a crucial role in cellular iron uptake due to high affinity for iron

reforming ferritin. Apoferritin has an outer diameter of 120 Å (12 nm) and inner core diameter of 80 Å (8 nm). [100] It is an approximately hollow sphere in shape and composed of 24 protein subunits some comprising of heavy (H) and light (L) chains.

Apoferritin was first realised from horse spleen, called as horse spleen apoferritin, and this material is still commonly used and abbreviated as HSAFt, It was the first protein cage used as a template in the synthesis of inorganic nanoparticles.[89,100] There are now several known loading methods for apoferritin, including: (i) pH-dependent reversible disassembly/reassembly mediated drug loading; (ii) channel-dependent drug loading using diffusion methods; (iii) urea-based drug loading achieved by enlargement of the apoferritin cage.[100] The choice of method employed is largely dependent on the properties of the cargo to be loaded.

1.12. Cell lines and biological techniques in cancer science

This thesis involves the use of a wide range of cancer cell lines and techniques used to measure both their proliferation and growth inhibition. It is therefore important here to provide suitable general background information on the materials and approaches we propose to employ in our research models (Chapters 2-3).

1.12.1. PANC-1 and Mia PaCa-2 pancreatic cancer cell lines

PANC-1 is a pancreatic cancer cell line derived from ductal pancreatic carcinoma of a 56 year-old Caucasian male. PANC-1 cells expressed multiple tumour markers including: epithelial-mesenchymal transition (EMT), cancer stem cells and neuroendocrine biomarkers.[101] PANC-1 cells also express vimentin and E-cadherin, markers responsible for transition of cancer cells towards more invasive phenotypes.[102] These cells also express CD44 and CD24 proteins,

cell surface markers responsible for increasing the tumorigenic potential of PANC-1.[103] Additionally, CA19-9, a well-known marker for pancreatic cancer has been found in PANC-1 along with SSTR2, a somatostatin receptor indicative of neuroendocrine differentiation.[104,105]

Furthermore, PANC-1 exhibits several well-known mutations, such as, homozygous missense mutations in the *TP53* gene (p.P72R and p.R273H) and heterozygous missense mutation in the *KRAS* gene (p.G12D).[106] The latter is a well-known protein involved in cancer progression. PANC-1 is typically used in pharmaceutical studies as an *in vitro* model of pancreatic ductal adenocarcinoma. It also has been used for studies of biomarker production and glucose metabolism in pancreatic cancer.[107]

Because pancreatic cancer is relatively heterogeneous, we also proposed to study the Mia PaCa-2 cell line as well, especially for 3D tissue models. This cell line was derived from the pancreatic ductal adenocarcinoma of a 65-year-old Caucasian male. In terms of protein expression, Mia PaCa-2 cells show elevated levels of clustering (CLU) and Bcl-2, which both impact cell growth, survival and resistance of the cells towards treatment agent.[108] Mia PaCa-2 cells also possess a mesenchymal phenotype, express E-cadherin and have low levels of phosphorylated Erk, make this cell line more aggressive than PANC-1.[109]

1.12.2. HCT-116 colon cancer cell lines

In developing new potential agents for cancer therapies, it is common to use an established cancer cell line as an additional tumour model allowing comparisons to other cell lines: HCT-116 is one such 'work horse' system in cancer biology. HCT-116 colorectal cancer cells are derived from colon cancer tissues showing constitutive KRAS activity (see Figure 1.2).[110] This

protein is a member of the Ras GTPase family and has a pivotal role in cell proliferation, differentiation and survival. Additionally, HCT-116 shows upregulation of β-catenin a protein that plays critical roles in both cell adhesion and the Wnt signalling pathway. The latter controls gene expression, cell behaviour, and ultimately many cellular outcomes.[111] HCT-116 (despite being cancerous) is also a genetically stable cell line, which makes it a useful model (as genetic drift is avoided, particularly if only low cell passage numbers are used).

1.12.3. MCF-7 breast cancer cell lines

The MCF-7 breast cancer cell line was historically derived from the metastatic pleural effusion of a female breast adenocarcinoma patient[112] and is commonly used in cancer biology. The MCF-7 cell line shows a fluid accumulation between the culture dish and their cell monolayer, making them exhibit epithelial-like morphology and monolayers that form dome structures. MCF-7 is one example of a few breast cancer cell lines that express the oestrogen receptor alpha (ER-α).[112] Thus, it is useful in modelling hormone-dependent breast cancer due to its sensitivity to oestrogen. MCF-7 also expresses glucocorticoid and progesterone receptor, which play pivotal roles in metabolism and inflammation regulation.[113]

1.12.4. MRC-5 lung fibroblast cells

MRC-5 is a human diploid cell lines originating from the lung tissue of a 14-week-old male foetus. It consists of connective tissue cells with normal male karyotype (46, XY).[114] It has a morphology of fibroblast-like cells, elongated and spindle-shaped.[114] It is not an immortalised cell lines and has a maximum passage number of 45-70 before entering senescence.[114] It has been used widely in biomedical research as a 'representative' non cancer cell line comparator.

Additionally, MRC-5 cells are also used more widely in vaccine production, virology/ toxicology, and general cell biology research.

1.12.5. 3D cultures and spheroid formation of pancreatic cancer

Cell culture is a crucial technique in biological and biomedical research involving growing and maintaining cell lines under controlled laboratory conditions that mimic the actual environment of the cell growth.[115] This technique can be used as a model for studying cellular and molecular biology, mechanism of certain disease, and drug development process. Cells used can be cultured using two major system; two-dimensional (2D) monolayers cell culture systems and three-dimensional (3D) culture systems.[115]

2D cell culture approaches utilise a system (i.e. tissue culture dishes, cell culture flask, or glass surface) to grow cells as a flat monolayer.[115] This technique approach has become a 'gold standard' in biomedical research, especially oncology, because it is cheap and easy to monitor.[115] However, 2D cell growth has a limitation in that it is not a three-dimensional structure like a real tissue, making it hard to do advance research in interactions between cells under actual living tissue conditions or in measuring nutrient uptake or oxygen intake towards tissues.[115] Thus, there is a need to have models that can mimic *in situ* cell growth under tissue-like conditions.

Real solid tumours grow *in vivo* in three-dimensional (3D) configurations, exposing the cancer cells to specific micro tissue environments (i.e. different nutrient gradients, hypoxia conditions, etc.) which mediate the cell's ability to grow.[116] However, conventional *in vitro* monolayer or bi-dimensional (2D) cell culture models fail to mimic precisely such actual 3D environments present in real tumour tissues/cell microenvironments.[116] This can lead to

contradictory or misleading results when comparing *in vitro* cell models to *in situ* tumours. This is particularly important in pancreatic cancer, as this cancer is notorious for having strong synergistic cell-cell interactions with surrounding cells/tissues (both normal (stromal) and cancerous).[117] Attaining new methods to model such systems is a contemporary goal in cancer research.[117] One simple way forward is to use 3D cell culture models. These have been widely developed and are now able to (at least partially) mimic conditions of the cells within real tumours.

Significant efforts have been made to optimise 3D cell cultures so that the modelled tumour environment is realistic. The simplest and most common approach is to use a spheroid model. Here the growth of the cells is expanded to produce sphere-like assemblies of ca. 1000-7000 cells able to mimic the cell-cell and cell-matrix interactions and gradients present in solid tumours.[116] This provides a very simple way to begin to understand the initial and avascular stages of tumours growth *in vivo*. For pancreatic cancer 3D spheroids, Mia PaCa-2 pancreatic cancer cell assemblies are widely used in such approaches due to their ability to (partially) reflect the cellular mechanism, cytoarchitecture, and tumour microenvironment of early-stage pancreatic cancer.[118]

Methods for generating such spheroid assemblies include: hanging drop (where cells are suspended droplet medium hanging in a plate lid using gravity), rotary cell culture (where cells are cultured rotating vessel), round bottom well plate (which uses concave bottom to force cells to settle in the middle), and ultra-low binding (using ultra-low attachment plate to prevent cells from adhering to the surface of the plate).[116] Sometimes these techniques also require the use of hydrogels to facilitate cell-cell contact and make spheroid growth viable.

However, the Mia PaCa-2 spheroid formation, targeted in our own studies does not need the addition of such adhesive agents.

Some cells have an innate tendency to aggregate and undergo self-assembly: in principle they could form spheroids on their own.[116] In fact, this phenomenon happens naturally during organogenesis, but it is also affected by several variables including: growth factors in cell culture medium, nutrients, oxygen availability, and paracrine factors (signalling molecules).[116,119] Spheroid formation is a growth process as the cell culture medium must penetrate inside the spheroid by diffusion to promote further growth and this is limited by spheroid size.[119] Additionally, the formation and growth of spheroids is controlled by the adhesion and differentiation of the aggregating cells. Extracellular matrix proteins, such as cadherin and integrin are highly involved in the mechanism of spheroid formation, as the function of these proteins is to promote cell-to-cell adhesion.[116] The process of spheroid formation can be divided into several steps: initial agglomeration of single cells, the adhesion of further cells, and cellular signal transduction. Agglomeration of single cells is accomplished by the loose adhesion to the peripheral cell surface, which is primarily triggered through the action of integrin.[120] Subsequently, E-cadherin promotes further adhesion of cell aggregates by homophilic binding between cellular cadherins, followed by cellular signal transduction by the β-catenin complex.[120] We planned to adopt such spheroid models in our own research investigations.

1.13. MTT assay

We introduce the MTT assay here as it is a central tool in our own studies in later chapters. The MTT assay uses a homogenous tertrazolium reduction assay for the detection of viable (metabolically active) cells.[121] The MTT (3-(4,5-dimethylthiazol-2-yl)-2,5-diphenyltetrazolium

bromide) molecule is positively charged and easily penetrates eukaryotic cells.[122] This is because MTT is relatively small and ambiphilic (has both hydrophilic and hydrophobic characteristics). This molecular structure enables MTT to diffuse and enter cells through the phospholipid bilayer of eukaryotic cell membranes.[122] The lipid solubility of the phenyl and thiazolyl groups of MTT solutions enable it to interact with hydrophobic site of the membrane, while the charged tetrazolium moiety maintains sufficient aqueous solubility to reman unbound in the cytosol of the cells.[123]

MTT detects living cells by an active metabolism mechanism whereby live cells convert MTT into a purple formazan product (Scheme 1.7) which has a strong absorbance of 570 nm.[122]

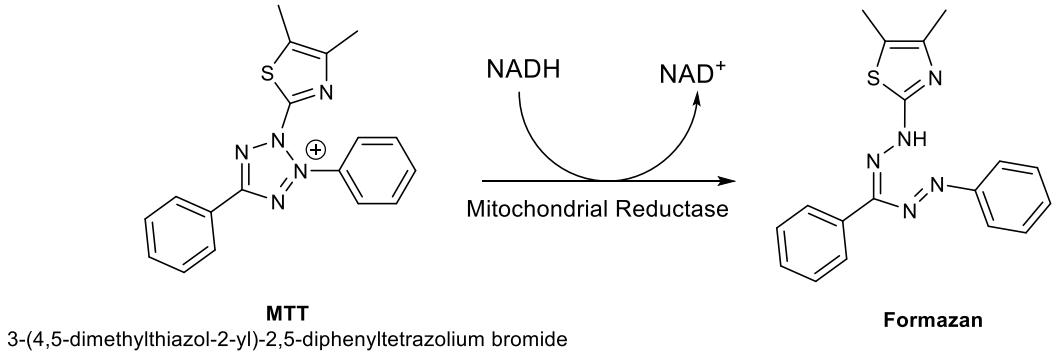

Scheme 1.7. Metabolic conversion by mitochondrial/cellular dehydrogenases.

The permeability of MTT is thus critical for its function as a metabolic activity probe, enabling it to reach intracellular reductive enzymes and provide an accurate measure of cell viability.[124] On the other hand, dead cells do not have *any* ability to convert MTT into formazan. The formazan created by live cells is accumulated in the form of insoluble precipitates inside cells, near the cell surface. Multiple strategies have been developed to solubilise the formazan products including the use of DMSO, SDS, dimethylformamide solvents and use of acidified isopropanol, as well as the combination of an organic solvent and a detergent. [121]

Typically, researchers use DMSO to solubilise the crystalline formazan as this leads to better accuracy and reproducibility in the MTT assays. While formazan is completely insoluble in aqueous media, the addition of DMSO allows its complete solubilisation resulting in uniform aqueous solutions suitable for absorbance measurements.[122] DMSO is particularly advantageous due to its robust solvation efficiency and minimal absorbance at 570 nm, resulting in no background interference by the solvent.[122] The efficiency and consistency of DMSO in solubilising formazan have direct impact in accuracy of cell viability quantification and sensitivity of the assay.[122] For these reasons it has become the most widely used of the colorimetric cell viability assays.

1.14. General aims of thesis

The major aim of this research is to discover a suitable titanium-based anti-cancer complex showing activity towards pancreatic cancer cells. Titanium complexes will be designed and synthesised towards this goal. Growth inhibition will be examined in 2D and 3D pancreatic cancer cell models. This research also attempts to encapsulate titanium complexes in apoferritin and determine their hydrolysis behaviour under near biological conditions.

Thus, the objectives are set for this study:

- To prepare new, well characterised, titanium complexes.
- To investigate the anticancer and cytotoxic activities of the new titanium complexes by biological assays to evaluate growth inhibition of cancer cells in both 2D and 3D pancreatic cancer culture, after optimisation of PANC-1 spheroids.
- To encapsulate the novel titanium complex using HSAFt nanocage.

- To determine the stability of the titanium complex by hydrolysis of the titanium complex under 20% DMSO 80% solvent.

2. CHAPTER TWO: PREPARATION AND ATTEMPTED APOFERRITIN ENCAPSULATION OF ONO-LIGATED TITANIUM(IV) ANTI-CANCER AGENTS

2.1. Research aims

As discussed in Chapter 1, titanium complexes (**2.1a-f**), which are attained from the ONO-*bis*-phenolate ligands (**2.2a-f**), are potent *in vitro* anti-cancer agents (Scheme 2.1).[84,85] The methyl (**2.1a**), allyl (**2.1b**) and fluoro (**2.1c**) complexes in particular are very active (GI_{50} < 10 μM in many cancer cell lines). These three complexes also represent a homologous variation of the 4-position (**Y** in Scheme 2.1) both in terms of size and electronic effects. While some information, both biological and chemical, is available on the behaviour of **2.1a-c** under dilute aqueous conditions, in the presence of cancer cells, understanding of this class of agents' 'mechanism of action' is far from complete. Two particular issues relevant to own work are: (i) understanding hydrolysis of complexes **2.1**, and (ii) finding a way to overcome the limited aqueous solubility of complexes of type **2.1** without negatively affecting their biological activity. For the former, no definitive picture has been developed, and for the latter, previous attempts to improve water solubility (e.g. via **2.1d** and related species) had led only to a reduction in anti-cancer activity.

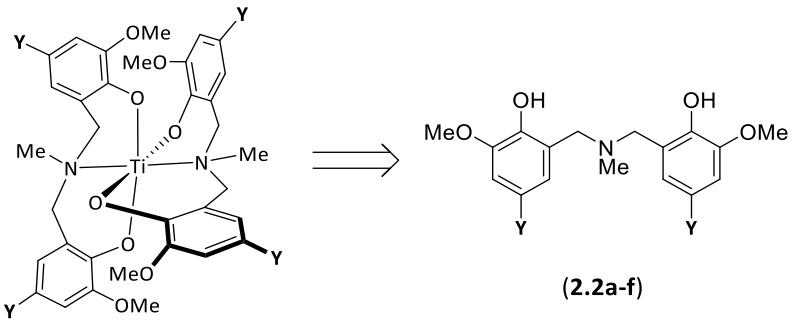

(**2.1a-f**) **Y** = Me (**a**), $CH_2CH{=}CH_2$ (**b**), F (**c**), CHO (**d**), Et (**e**), *n*-Pr (**f**) (**2.2a-f**)

Scheme 2.1. Literature[84,86] titanium(IV)-ONO complexes of relevance to this chapter.

In this Chapter we aim to:

- Acquire samples of the complexes **2.1a-c**, of suitable purity for both mechanistic and biological studies.

- Understand the pathway(s) by which complexes **2.1** hydrolyse in dilute aqueous solution as a function of pH and other additives (especially urea).

- Conduct preliminary investigations to identify if complexes **2.1** can be encapsulated in ferritin proteins, as discussed in Chapter 1, by methods involving either pH or urea manipulation of the apoferritin protein, to upload **2.1**, thus providing a new method for drug delivery of agents **2.1**.

2.2. Preparation of ligands (2.2a-c)

At the start of our studies, while we had some complexes of type (**2.1**) already available, but it was deemed useful to have freshly prepared samples, necessitating synthesis of the precursor ONO-ligands (**2.2**). Initially, we concentrated on the preparation of the methyl ligand **2.2a**, which from literature studies,[84,85] can be prepared by two methods (Scheme 2.2), and subsequent product separation, effected by column chromatography.

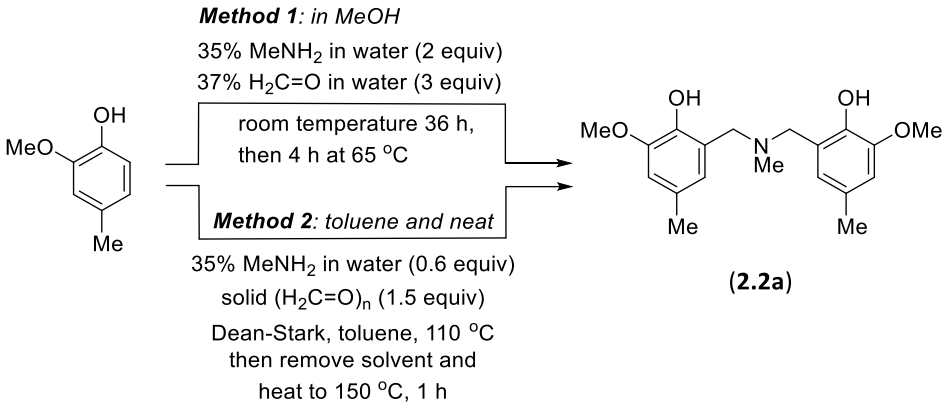

Scheme 2.2. Reported literature [84,86] preparations of methyl ligand (**2.2a**).

As Musa[85] had reported good yields (50-80%) for ligands **2.2b-f** we initially employed his 'Method 1' (Scheme 2.2), even though he had not used it specifically for **2.2a**. Application of Musa's method initially seemed successful as the starting 2-methoxy-4-methylphenol was converted into a major new species (R_f 0.47 in 4:1 cyclohexane:EtOAc). However, repeated attempts to complex this ligand batch to titanium(IV) by use of TI(O-*i*-Pr)$_4$ led to only very poor samples of complex **2.1a** being isolated, which is not expected. This led us to also prepare a second sample of ligand **2.2a** via the approach of Abid ('Method 2', Scheme 2.2).[84] This was also apparently successful leading to a new major product (R_f 0.62 in 4:1 cyclohexane:EtOAc products of 'Method 1' and 'Method 2' were both isolated by column chromatography and further purified by recrystallisations from Et_2O-pentane at 4 °C. Alarmingly, the crystals from 'Method 1' show a colourless needle shaped habit, while that of 'Method 2' are pale yellow hexagonal plates. Spectroscopic comparison of the two 'ligand' samples from 'Method 1' and 'Method 2' is complicated by the fact that neither reaction was particularly clean (~50% yield) and that imperfect chromatographic separation of the major products and several minor colourless and yellow uncharacterised by-products co-elute with the desired **2.1a** (from either

method). The ^{1}H NMR spectra, in the aryl region, of both samples is near identical in impure samples. Figure 2.1 shows the equivalent region for highly purified materials. Proton NMR spectra of crude 2.1 (from either 'Method') confusingly also overlap with authentic samples of pure ligand **2.1a**, despite their different R_f values and crystal habits. Full spectroscopic data for the materials isolated are given in Table 2.1, however, at the time of their initial isolation we did not have all of this data and its interpretation was complicated by the presence of significant impurities in both samples. The initial data we had led us to speculate that we had isolated either two tautomeric forms of the desired ligand (**2.1a** and **2.1a'**), or that we had isolated an impure sample containing mono functionalised **2.3** (Scheme 2.3). As we were unable initially to make a definitive structural assignment, we moved to X-ray structural analysis, see the next section.

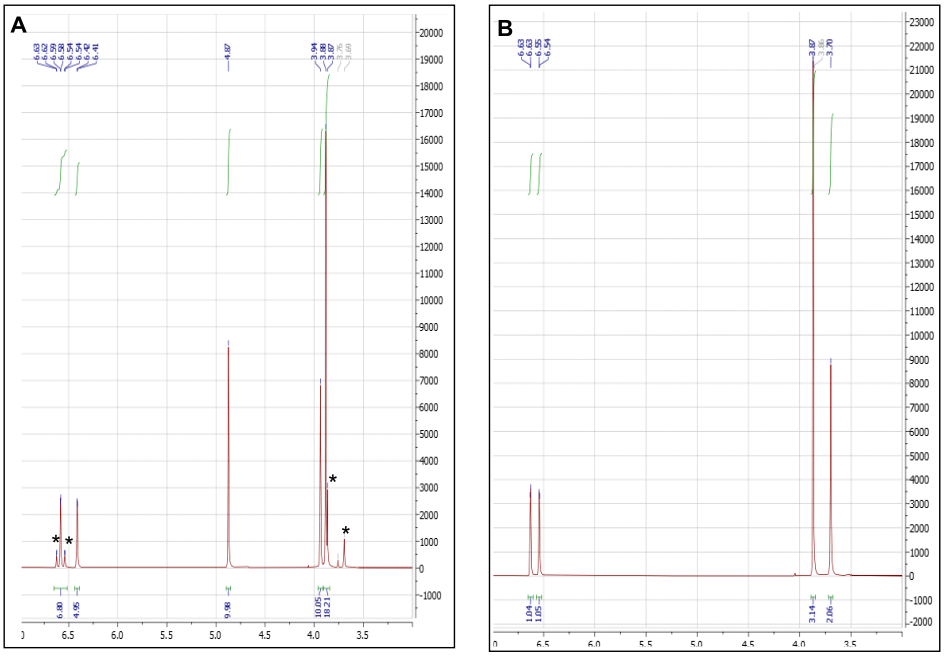

Figure 2.1. A. Partial ^{1}H NMR spectrum of 'ligand' sample from 'Method 1' (3-7 ppm). **B**. Partial ^{1}H NMR spectrum of 'ligand' sample from 'Method 2' (3-7 ppm). Traces of the latter product can be seen in in the former (shown by *).

Table 2.1. Spectroscopic data for the 'ligand' samples arising from the chemistry of Scheme 2.2.

Technique	'Ligand' from 'Method 1' (Scheme 2.2)	'Ligand' from 'Method 2' (Scheme 2.2)
^{1}H NMR (400 MHz, $CDCl_3$)	δ_H 6.56 (s, 1H, ArH), 6.39 (s, 1H, Ar*H*), 4.85 (s, 2H, OCH_2), 3.91 (s, 2H, OCH_2), 3.86 (s, 3H, OCH_3), 2.61 (s, 3H, NCH_3), 2.26 (s, 3H, CH_3)	δ_H 8.42 (br s, 2H, O*H*), 6.63 (d, 2H, *J* = 1.8 Hz, Ar*H*), 6.54 (d, 2H, *J* = 1.8 Hz, Ar*H*), 3.87 (s, 6H, ArO*CH₃*), 3.70 (s, 4H, Ar*CH₂*N), 2.28 (s, 6H, Ar*CH₃*), 2.21 (s, 3H, N*CH₃*)
^{13}C NMR (100 MHz, $CDCl_3$)	δ_C 147.5 (C), , 140.9 (C), 129.6 (C), 120.1 (C), 19.6 (CH), 110.5 (CH), 84.3 (CH_2), 56.0 (CH_2), 51.9 (OCH_3), 40.0 (NCH_3), 21.3 (CH_3)	δ_C 147.0 (C), 143.5 (C), 128.2 (C), 122.3 (C), 122.1 (CH), 111.3 (CH), 58.5 (CH_2), 55.9 (CH_3), 40.8 (NCH_3), 21.1 (CH_3)
Infra-red (ATR)	2991, 2953, 2899, 1670, 1589, 1498, 1468, 1450, 1409, 1378, 1349, 1317, 1290, 1275, 1227, 1205, 1187, 1148, 1136, 1096, 1084, 1052, 1032, 1017,	3007, 2980, 2949, 2912, 2847, 2809, 1604, 1501, 1495, 1462, 1445, 1418, 1383, 1365, 1329, 1299, 1285, 1262, 1250, 1235, 1210, 1192, 1156, 1121,

	982, 963, 944, 915, 856, 845, 823, 791, 751, 737, 715, 686, 607, 586, 537, 512, 474, 450	1088, 1024, 986, 967, 954, 921, 875, 832, 787, 756, 739, 691, 665, 591, 566, 551, 467, 445
Mass spectrum (+ESI)	HRMS $(M+H)^+$ Calcd. for $C_{11}H_{16}NO_2$ 194.2502, found 194.1179	HRMS $(M+H)^+$ Calcd. for $C_{19}H_{26}NO_4$ 332.4140, found 332.1886

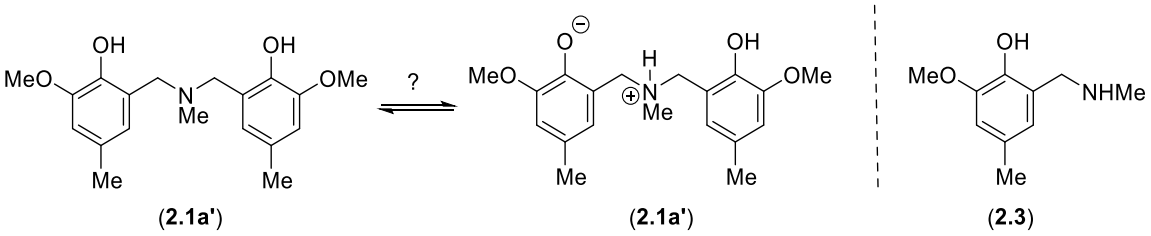

(**2.1a'**) (**2.1a'**) (**2.3**)

Scheme 2.3. Initial proposals for potential structures for the materials resulting from the two methods of Scheme 2.2.

2.2.1. Crystallographic studies of the 'ligand' materials from Scheme 2.2

Our recrystallised samples proved suitable for single crystal X-ray studies. An initial study revealed that the hexagonal plate crystals, isolated from 'Method 2' are indeed the desired ligand (**2.1a**), whose structure is shown in Figure 2.2, together with a schematic showing the atom numbering scheme. Selected bong lengths and angles are shown in Table 5.1 (Appendix). Interestingly, in the solid-state at least, there is a significant hydrogen bond between O-H38A and N1A (Figure 2.2) suggesting that the equilibrium proposed in Scheme 2.3 is not unreasonable. A partial packing diagram of (**2.2a**) is shown in Figure 2.3 and reveals that the unit cell is composed of two independent molecules.

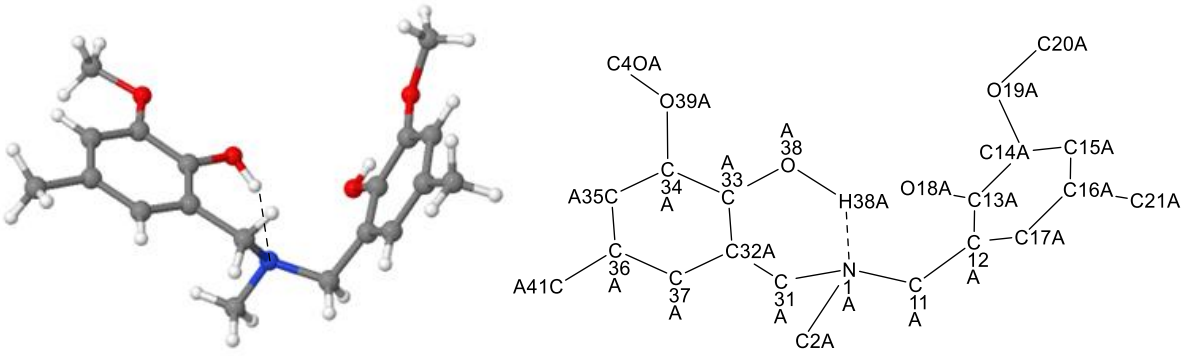

Figure 2.2. Molecular structure of hexagonal plate crystals ('Method 2' from Scheme 2.2) confirmed to be **2.2a** by X-ray crystallography. The hydrogen bond distance between N1A….H38A is 1.98 Å.

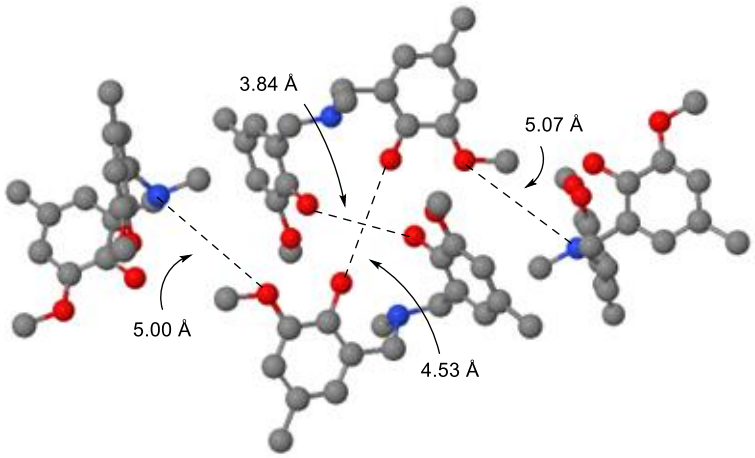

Figure 2.3. Partial molecular packing diagram for (**2.2a**), hydrogen atoms excluded for clarity.

Conversely, crystallographic investigation of the 'ligand' material from 'Method 1' in Scheme 2.2 revealed it to be neither the ligand (**2.2a**), nor any of the suggestions of Scheme 2.3, but 8-methoxy-3,6-dimethyl-3,4-dihydro-*2H*-benzo[e][1,3]oxazine (**2.4**) (Figure 2.4). Selected bong lengths and angles are shown in Table 5.2 (Appendix), while a partial packing diagram is presented in Figure 2.5.

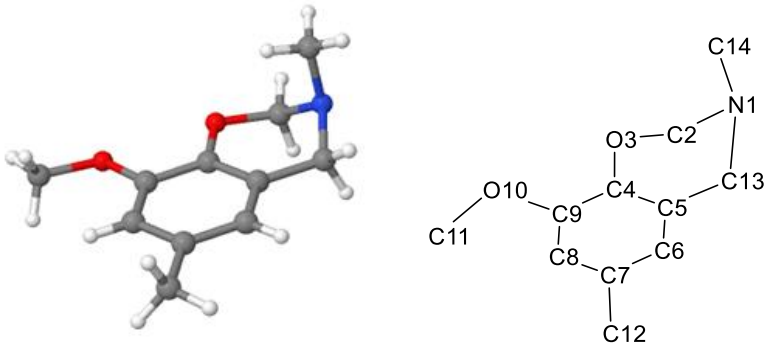

Figure 2.4. Molecular structure of needle crystals ('Method 1' from Scheme 2.2) confirmed to be 8-methoxy-3,6-dimethyl-3,4-dihydro-*2H*-benzo[e][1,3]oxazine (**2.4**) by X-ray crystallography.

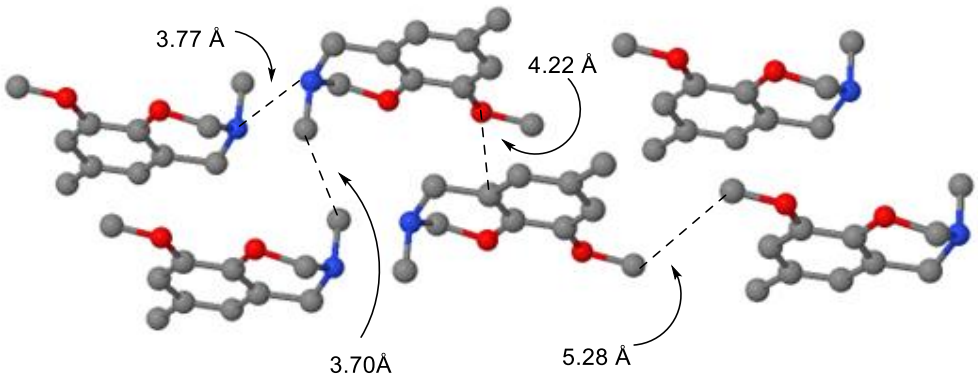

Figure 2.5. Partial molecular packing diagram for (**2.4**), hydrogen atoms excluded for clarity.

Referring to Table 5.2, the longest bond distance in **2.4** is C(5)–C(13) at 1.5153 Å. This bond length is in the range expected for a C(sp^3)-C(sp^3) single bond (typically 1.54 Å). On the other hand, the shortest bond distance obtained from crystallography data of **2.4** is O(10)–C(9) with a length of 1.3682 Å. This is shorter than single bond distance of O-C bond (typically 1.43 Å) and longer than O-C double bond (typically 1.21 Å). Thus, it is an indicative of partial double-bond. This happens because of the lone pairs of the oxygen atom are in resonance with the ring system with that directly influences the distance of the O-C bond.

The formation of 3,4-dihydro-*2H*-benzo[e][1,3]oxazine intermediates in the preparation of ligands **2.2b-f** has been noted before.[85] However, the latter study did not involve the preparation of **2.2a**. In our hands, at least, the formation of **2.4** under mild conditions (mild heating in methanol reflux) seems to preferentially favour the formation of this product, which was unexpected. Both **2.2a** and **2.4** can be isolated from the use of methylamine and formaldehyde as they share the common intermediate (**2.5**, in box within Scheme 2.4).

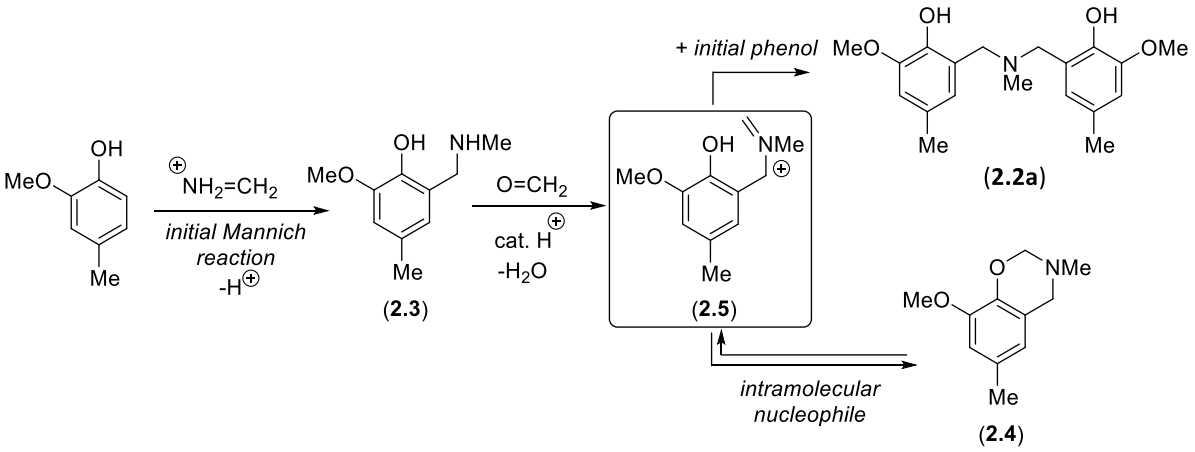

Scheme 2.4. Mechanistic rational for the formation of **2.2a** and **2.4**.

An initial Mannich[85] reaction leads to the production of initially proposed **2.3**. However, this is efficiently captured by formaldehyde to form intermediate **2.5** which undergoes unexpected rapid 6-*endo*-trig[85] intramolecular cyclisation to **2.4**, which isolated from reactions at mild temperatures (<65 °C, 'Method 1'). Under more forcing conditions (150 °C, 'Method 2') **2.4** is capable of re-opening and **2.5** is captured by a second equivalent of the phenol starting material. This Mannich reaction leads directly to ligand **2.2a**.

2.3. Preparation of ONO-ligated Ti(IV) complexes

Our initial attempts to prepare complex (**2.1a**) were frustrated as, at that point we were unaware that our initial sample of ligand (**2.2a**), was in fact mostly 8-methoxy-3,6-dimethyl-3,4-dihydro-*2H*-benzo[e][1,3]oxazine (**2.4**). Because of this, attempts to prepare its complex (**2.1**, Scheme 2.5) under standard conditions provided only impure samples of the complex (ca. 60-80% purity, even after multiple recrystallisations). While this initial **2.1a** material proved suitable for preliminary biological studies (see Section 2.5), it was not appropriate for accurate solution speciation or kinetic studies. Fortunately, through existing collaborations,[125] we had access to analytically pure samples of the allyl (**2.1b**) and fluoro (**2.1.c**) and their associated ligands (**2.2b-c**). Therefore, we chose to focus onward studies on these, especially the allyl derivative.

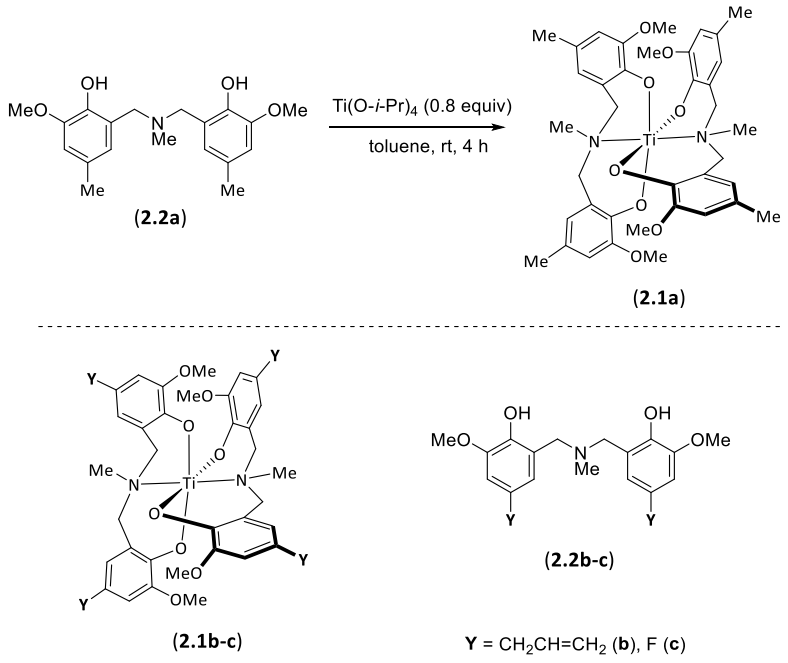

Scheme 2.5. Literature [84,86] procedure used for the preparation of our sample of complex (**2.1a**).

2.4. Hydrolysis study of titanium complex

2.4.1. Preliminary observations

Very initial results confirmed that the purity of our methyl complex (**2.1a**) was insufficient to attain accurate mechanistic data. However, these studies also indicated that allyl complex (**2.1b**) is a suitable alternative. Before any kinetic data could be acquired, the baseline solubility of (**2.1b**) need to be determined. Our studies confirmed the latter is almost completely insoluble in water, but it has appreciable solubility in dry DMSO (up to ca. 700 mM). Thus, the titanium complex (**2b**) can be dissolved in dry DMSO and diluted with aqueous media to provide mixtures whose nominal concentration varied from 37.5 μM to 1.86 mM. Deionised water, pH 7.4 phosphate buffer, pH 5.0 acetate buffer or 8 M urea aqueous solutions proved useful (Table 2.4). These were visually inspected and their solubility characteristics and the data reported in Table 2.4. Attempts to use pH 10 buffer solutions are unsuccessful, orange **2.1b** rapidly de-colourised (runs 21-24). Presumably, deprotonated ligand and TiO_2 are formed. At high complex concentrations (run 21, 300 μM) the presence of a colourless precipitate is clear.

Table 2.4. Solubility studies of allyl titanium complex (**2.1b**) in various DMSO-aqueous solutions and at different concentrations and compositions. Combinations useful for spectroscopic studies are highlighted.

Run	Nominal Concentration	Composition	Notes
1	1.86 mM	50% DMSO, 50% water	Precipitates
2	1.06 mM	71% DMSO, 29% water	Trace of solid precipitation
3	761.2 µM	80% DMSO, 20% water	Fully soluble
4	585.4 µM	73% DMSO, 27% water	Starts to precipitate, trace of solid
5	300 µM	80% DMSO, 20% water	Fully soluble
6	150 µM	40% DMSO, 60% water	Just about soluble
7	75 µM	20% DMSO, 80% water	Fully soluble
8	37.5 µM	10% DMSO, 90% water	Fully soluble, clear transparent yellow solution
9	300 µM	80% DMSO, 20% 8 M urea	Fully soluble
10	150 µM	40% DMSO, 60% 8 M urea	Just about soluble
11	75 µM	20% DMSO, 80% 8 M urea	Fully soluble

12	37.5 µM	10% DMSO, 90% 8 M urea	Fully soluble, clear transparent yellow solution
13	300 µM	80% DMSO, 20% acetate buffer (0.1 M, pH 5.0)	Fully soluble, yellow solution
14	150 µM	40% DMSO, 60% acetate buffer (0.1 M, pH 5.0)	Just about soluble
15	75 µM	20% DMSO, 80% acetate buffer (0.1 M, pH 5.0)	Just about soluble
16	37.5 µM	10% DMSO, 90% acetate buffer (0.1 M, pH 5.0)	Fully soluble
17	300 µM	80% DMSO, 20% phosphate buffer (0.1 M, pH 7.4)	Fully soluble
18	150 µM	40% DMSO, 60% phosphate buffer (0.1 M, pH 7.4)	Just fully soluble
19	75 µM	20% DMSO, 80% phosphate buffer (0.1 M, pH 7.4)	Fully soluble
20	37.5 µM	10% DMSO, 90% phosphate buffer (0.1 M, pH 7.4)	Fully soluble, clear transparent yellow solution

21	300 μM	80% DMSO, 20% hydroxide-glycine buffer (0.08 M, pH 10)	Decolourizes, white precipitate forms
22	150 μM	40% DMSO, 60% hydroxide-glycine buffer (0.08 M, pH 10)	Fully soluble, transparent solution, no colour
23	75 μM	20% DMSO, 80% hydroxide-glycine buffer (0.08 M, pH 10)	Fully soluble, transparent solution, no colour
24	37.5 μM	10% DMSO, 90% hydroxide-glycine buffer (0.08 M, pH 10)	Fully soluble, transparent solution, no colour

Higher concentrations of complexes **2.1b** (>300 μM in aqueous mixtures) proved only partially soluble or led to supersaturated solutions that easily reprecipitated (**2.1b**) as orange powders. For example, in an independent study with complex **2.1c** could be re-isolated as single crystals (as confirmed by X-ray crystallography), in addition to precipitated **2.1c** powder. From Table 2.4 it can be concluded that allyl complex (**2.1b**) can be studied in mixed DMSO plus aqueous media in 20:80 v/v mixtures can also be reliably studied at concentrations up to 75 μM for UV–vis spectroscopy (highlighted in Table 2.4). However, for $^{1}H/^{19}F$ NMR spectroscopy higher concentrations (300-500 μM) are needed to enable data accumulation within minutes) and

these required greater amounts of DMSO (typically 80% DMSO and only 20% of the aqueous component, highlighted in Table 2.4). However, all of the DMSO-aqueous mixtures (regardless of composition in the range 20:80 to 80:20 DMSO to aqueous component) are unstable and begin to undergo change within minutes, leading to challenges in their quantification. In contrast, solutions of (**2.1b**) in dry DMSO (either deuterated or non-deuterated) remain spectroscopically stable for at least one month, as confirmed by ^{1}H NMR and UV–vis spectroscopy, the latter allowing quantification of (**2.1b**) using the Beer-Lambert law (Figure 2.6).

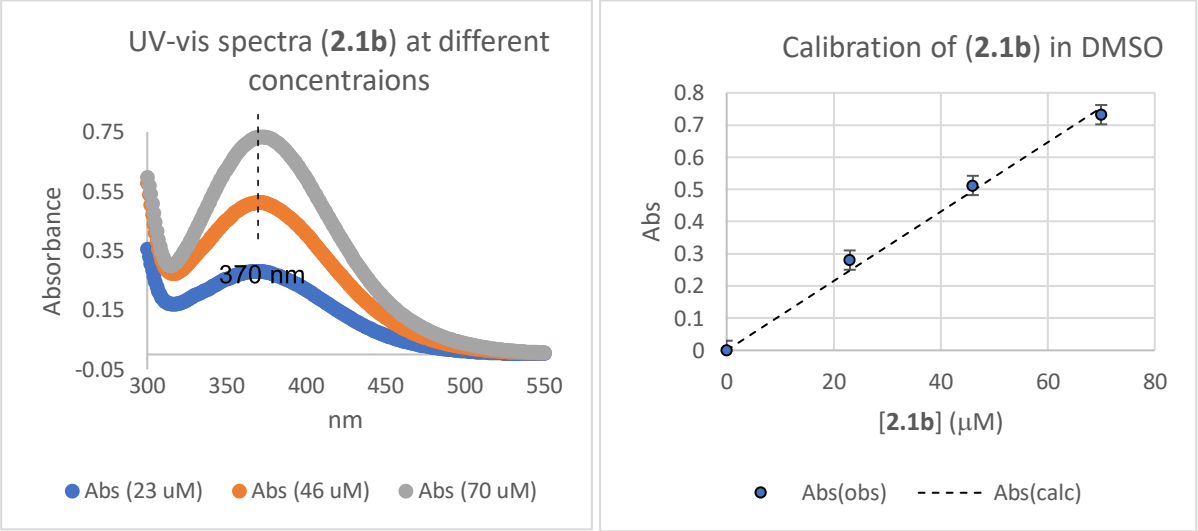

Figure 2.6. Derivation of the molar absorptivity (extinction coefficient) ε_{370} for complex (**2.1b**) in neat DMSO. A fit of ε_{370} = 0.0108(3) μM^{-1} cm^{-1} with R^2 = 0.994 at 370 nm. Other values of ε could be determined at different wavelengths.

In neat dry DMSO a distinct absorption maximum (λ_{max}) is observed at 373 nm (Figure 2.6) for complex (**2.1b**), which is attributed to a ligand-to-metal charge transfer (LMCT) transition for ligand→Ti(IV). Attempts to similarly calibrate complex (**2.1b**) in 80:20 water:DMSO are not successful. After the addition of distilled water (to afford DMSO/water = 20:80 v/v) the 373 nm

absorbance of **2.1b** undergoes a time dependent shift to ca. 420 nm, as the overall absorbance of the sample falls. An initially fast process (within mins, that produces a small change in the reaction absorbance), then a slower process (days) which results (eventually) in a precipitate forming in the UV cell. Over 3 days the solution changes from a pale-yellow solution to an absolutely colourless supernatant, having no absorbance at 300-550 nm, with a bright yellow precipitate on the bottom of the cuvette (Figure 2.7). This yellow material is insoluble in all common NMR solvents, but it may be filtered onto Whatman glass microfiber GF/A, washed with water, and the disk dried. Subsequent IR analysis (Figure 2.7) indicates the presence of a titanium coordinated ligand species 'TiL', based on the similarity of the IR spectrum to that of the parent TiL_2 (**2.1b**), see experimental section. The isolated yellow material is apparently not recovered (**2.1b**) as it is insoluble in DMSO, which (**2.1b**) is.

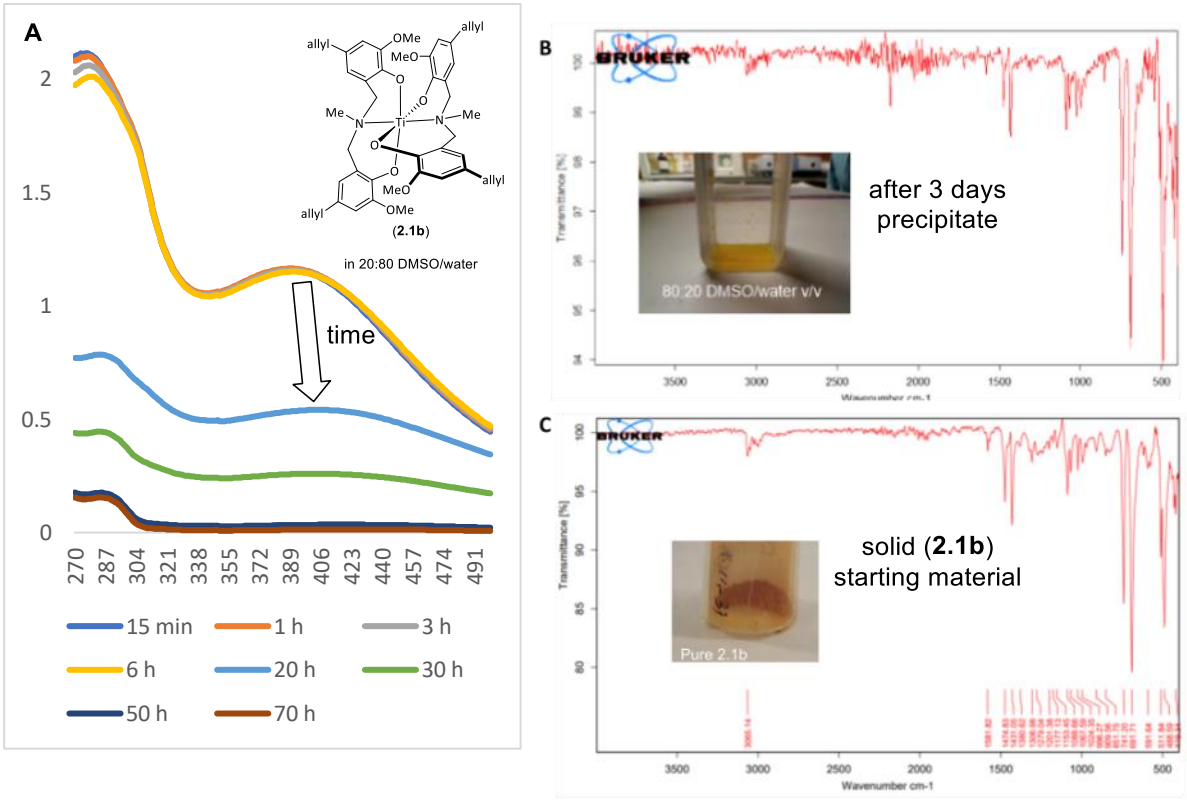

Figure 2.7. (**A**) Time dependant UV-vis spectra of complex (**2.1b**) in 20:80 DMSO:water. A slightly supersaturated solution of **2.1b** was used to maximised the amount of precipitate

isolated, [**2.1b**]$_{initial}$ = 105 μM. (**B**) IR spectrum of the yellow precipitate (ATR, of sample on QF glass filter paper, the later used as a background) isolated (< 1 mg) after 3 days (after washing with water, to remove DMSO, and air drying at room temperature). **C** IR spectrum (ATR) of genuine (orange) **2.1b**.

The UV-vis spectrum of the colourless supernatant liquid providing the yellow precipitate of Figure 2.7 reveals a small maximum at 290 nm, which is coincident with an identical absorption in the parent ligand (**2.2b**). Calibrating authentic ligand (**2.2b**) in 20:80 DMSO:water allowed us to determine the concentration of ligand in solution in the sample of Figure 2.7 to be 135 μM. As this is 1.3× the original 105 μM solution of **2.1b** we deduce that the yellow precipitate has one ligand per titanium and the extra 0.3 equivalent is due to either experimental error, or that some further hydrolysis has occurred leading to contamination with ca. 15% TiO_2 and additional ligand (**2.2b**). The complete insolubility of the yellow precipitate made it hard to characterise. Attempts to realise MALDI mass spectra provided evidence of residual complex [found *m/z* 810, **2.1b** requires *m/z* 810] and ligand [found *m/z* 385 (L+2H), **2.2b** requires *m/z* 383] together with uncharacterised signals at *m/z* 671, 649, 633, 605, 493 and 456. The first and largest of these appears to show a titanium isotope pattern. We are not sure if these latter signals represent true fragments, artifacts of the MALDI process, or secondary ions generated by the breakdown of an oxide dimer, most likely to be LTi(μ-O)$_2$TiL, where L is the dianion of ligand **2.1b** based on mass balance of ligand left in the supernatant solution.

Finally, preliminary NMR investigations of the hydrolysis of complex (**2.1b**), albeit in 80:20 DMSO-d_6:D_2O at 300 μM, also reveal that there is very rapidly (within 1 h), but only partial, conversion of **2.1b** into to a new minor new species. This is most easily detected in the aromatic region where the existing four diastereotopic aryl C-H signals of **2.1b** (δ_H 6.65, 6.59,

6.52 and 6.48) are joined by two minor new signals (δ_H 6.66 and 6.50) that are almost coincident with the chemical shifts of ligand (**2.2b**) in the same solvent. It is also clear from the broadening of the minor component and major component are in exchange, and that this results in an initially stable equilibrium mixture (for the first 60 mins). Over the course of time (days) the intensity of complex **2.1b** falls and no other appreciable amount of complex replaces them, just ligand is observed. After 3 days the NMR tube contains an appreciable amount of precipitate, akin to that in Figure 2.7. These results led us to conclude that complex **2.1b** is undergoing hydrolysis to form an intermediate (missing one ligand) and the free ligand **2.2b**. Because of the exchange noted above, we could not detect the minor titanium complex specie. Therefore, we set out to define its existence using chemical kinetics.

2.4.2. Kinetics studies

UV–vis spectra were recorded between 270 and 700 nm, limited by the DMSO cutoff at 268 nm at a spectrometer at a scan speed appropriate to capture spectra faster than the observed fast kinetics. All spectra were baseline-corrected to zero absorbance at 632 nm (the minimum absorbance of **2.1b** in the range studied) to ensure consistent application of Beer's law for concentration determinations. Data collected every 5-20 mins (as appropriate for the experimental rate) over a 16 h period (or longer) automatically. These data provide insights, when the behaviour of the λ_{max} absorption (at 380 nm) of the starting material (**2.1b**) are plotted vs. time for hydrolyses in the presence of water (Figure 2.8A) and pH 7.4 phosphate buffer (Figure 2.8B) systems. In all these reactions, as close as was possible, the initial concentrations used are $[\mathbf{2.1b}]_{initial}$ = 76 μM (in 20:80 DMSO to aqueous component mixtures). Identical investigations were carried out using pH 5 buffer (Figure 2.8C) and 8 M urea (Figure 2.8D).

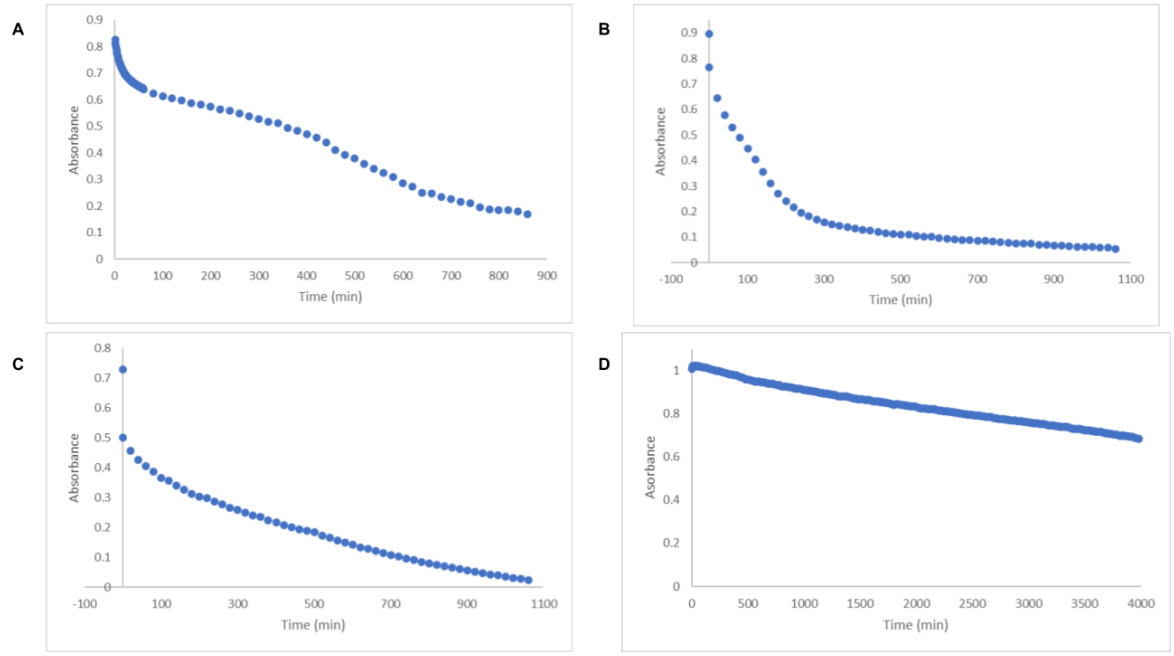

Figure 2.8. Time dependent UV-vis absorbance at 380 nm for hydrolysis of complex (**2.1b**), initially at 76 μM, dissolved in a 20% DMSO and 80% water (**A**), a 20% DMSO and 80% pH 7.4 phosphate buffer (**B**), a 20% DMSO and 80% pH 5.0 acetate buffer (**C**), a 20% DMSO and 80% 8 M urea (**D**), v/v mixture. Data collection was stopped at 860 min (14.3 h) as yellow precipitate formation started to lead to poor data quality.

It is clear in both the first two cases (Figures 2.8A and 2.8B) there is an initial 'faster' process, followed by a 'slower' decay. Using Billo's approach,[126] we investigated the order of both these decays and found that the former most accurately fitted a first order reversible reaction (R^2 >0.99), and the second process a second order irreversible reaction (R^2 >0.99). Our decisions on which kinetic scheme[127] to fit were guided by the quality of fit they provided under Billo's "Solvstat" analysis tool.[126] Clearly, the 'faster' and 'slower' processes are linked by a common intermediate. We therefore proposed the model of Scheme 2.6 as the simplest consistent with all the observations made so far.

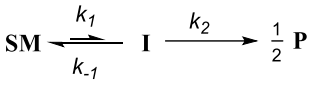

$$\frac{-d[\mathbf{SM}]}{dt} = k_1[\mathbf{SM}] - k_{-1}[\mathbf{I}] \quad (2.1)$$

$$\frac{d[\mathbf{I}]}{dt} = k_1[\mathbf{SM}] - k_{-1}[\mathbf{I}] - k_2[\mathbf{I}]^2 \quad (2.2)$$

$$\frac{d[\mathbf{P}]}{dt} = \frac{1}{2}k_2[\mathbf{I}]^2 \quad (2.3)$$

Scheme 2.6. Kinetic scheme proposed for hydrolysis of complex (**2.1b**) and associated rate law equations.

Within Scheme 2.6, complex **2.1b** is **SM** (the starting material), **I** (some presently undefined intermediate), and **P** (the yellow insoluble product of our reaction). The fractional coefficient in front of **P** and the associated second order rate constant k_2 indicate that **P** is formed by combination of two molecules of **I**. Unfortunately, differential equations of higher order consecutive reactions (such as Scheme 2.6) cannot be integrated into closed forms since these equations contain more than one dependent variable.[127] We therefore chose to simulate this model using a simple numerical integration approach to Equations 2.1-2.3 of Scheme 2.6 on Excel.[127] We chose to fit the observed absorbance at 380 nm to that calculated through Equation 2.4.

$$A_{380}(\text{calc}) = A_{380}(\mathbf{SM}) + A_{380}(\mathbf{I}) + A_{380}(\mathbf{P}) \quad (2.4)$$

Where: A_{380}(calc) is the calculated absorbance at 380 nm and A_{380}(**SM**), A_{380}(**I**) and A_{380}(**P**) are the calculated absorbances of the starting material, intermediate and product. Our optimisation was made by minimising the error between A_{380}(obs) and A_{380}(calc) through non-linear least squares regression of the values of k_1, k_{-1}, k_2, ε_{380}(**SM**), ε_{380}(**I**) and ε_{380}(**P**), where the k values are the rate constants and the ε values the molar absorptivity at 380 nm. Graphical outputs from fitting these data are shown in Figures 2.9-2.10, while the derived rate constants

and molar absorptivity and goodness of fit values are reported in Table 2.5 for hydrolysis of complex (**2.1a**) in DMSO solutions (20% by volume) that were co-mixed with water and pH 7.4 phosphate buffer, pH 5.0 acetate buffer, or 8 M aqueous urea (all 80% v/v in the mixture with DMSO).

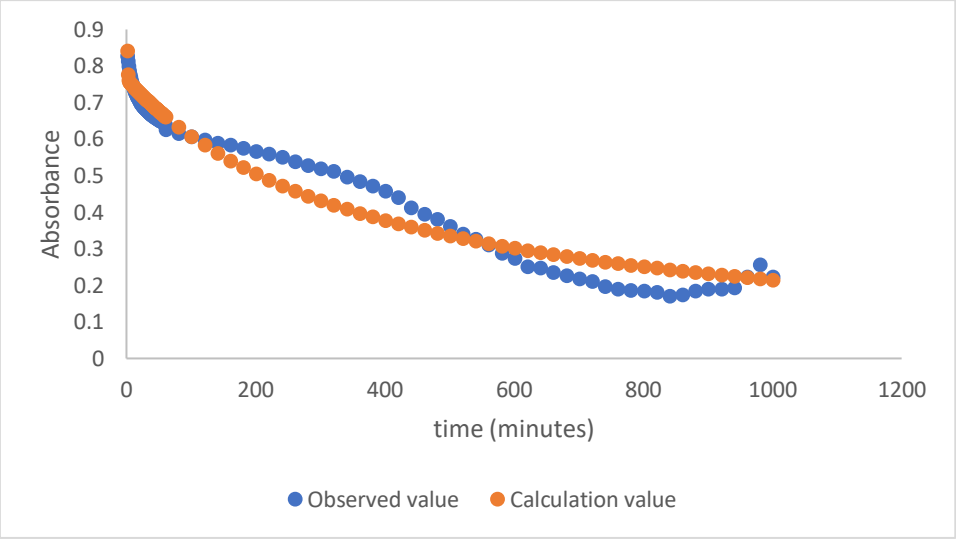

Figure 2.9. Comparison of observed data for hydrolysis of **2.1b** dissolved in a 20% DMSO and 80% water, v/v mixture vs. that calculated by simulation of Scheme 2.6.

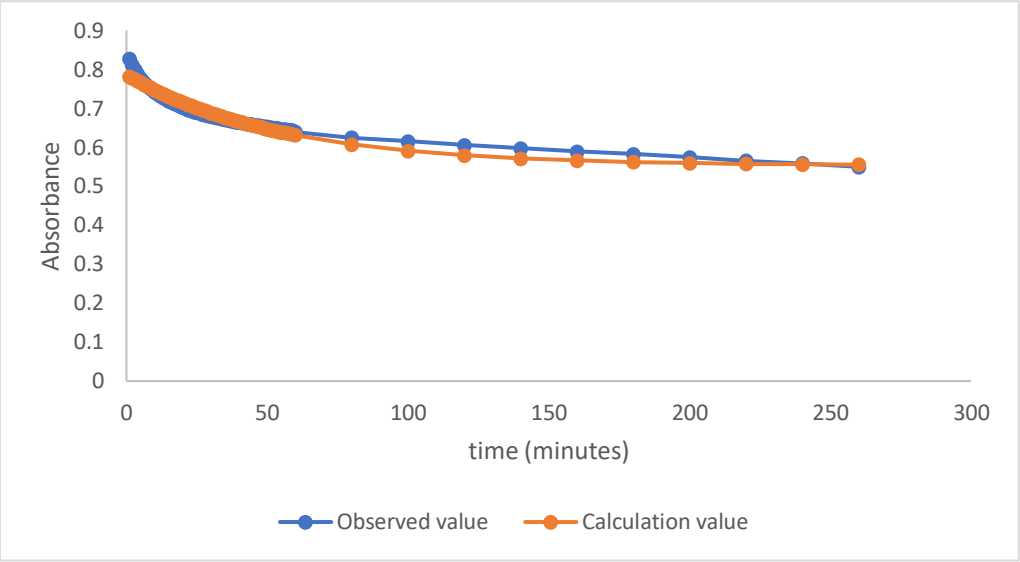

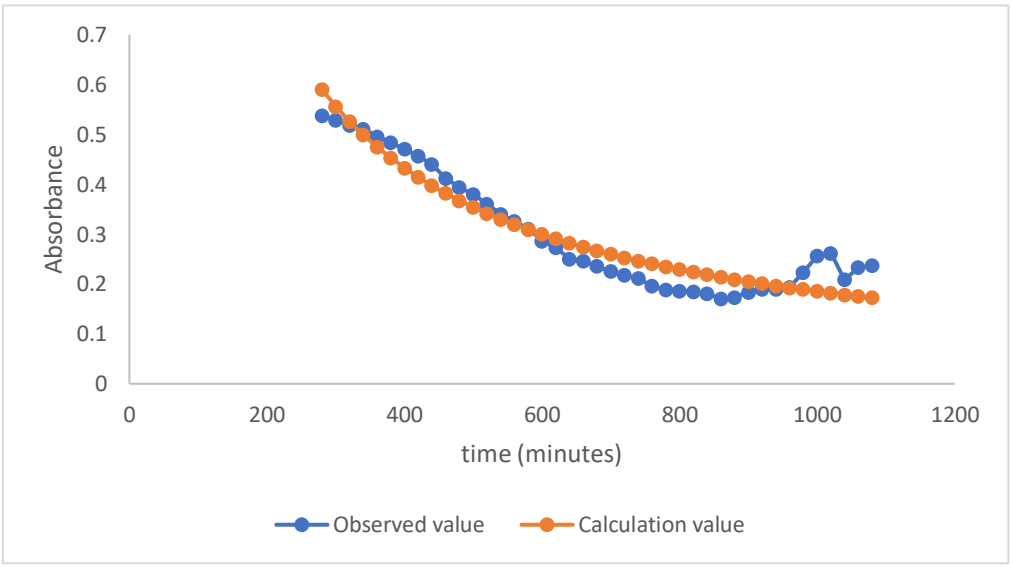

Figure 2.10. Comparison of observed data for hydrolysis of **2.1b** dissolved in a 20% DMSO and 80% water, v/v mixture vs. calculation value in first order reaction and second order reaction, respectively.

As can be seen in Figure 2.9, the model proposed does not the observed values leading to an erroneous calculated value of k_1/k_2 in the kinetics study. Thus, we tried to do separate simulations for both the first order and second order reactions. Figure 2.10 shows that a first order reaction fits observed data with some slight outliers.

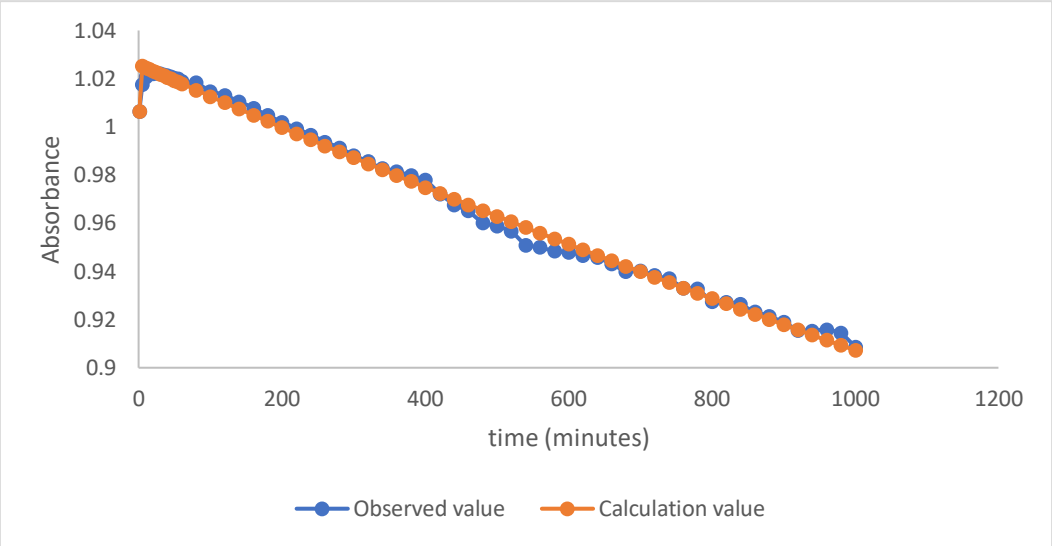

Figure 2.11. Comparison of observed data for hydrolysis of **2.1b** dissolved in a 20% DMSO and 80% 8 M urea, v/v mixture vs. that calculated by simulation of Scheme 2.6.

The hydrolysis model (refer to Scheme 2.6) of **2.1b** fits the data in the solvents 20% DMSO 80% 8 M urea (Figure 2.11) and 20% DMSO 80% phosphate buffer (Figure 2.12). However, there are some of poorly fitted data points (refer to Figure 2.12), reflecting perhaps a deficiency in the model or experimental error. For example, the calculated fit in Figure 2.12 shows that in the first 200 minutes the model runs faster than the real experiment. However, for the 200-600 minute data, the model values runs slightly slower than the real data.

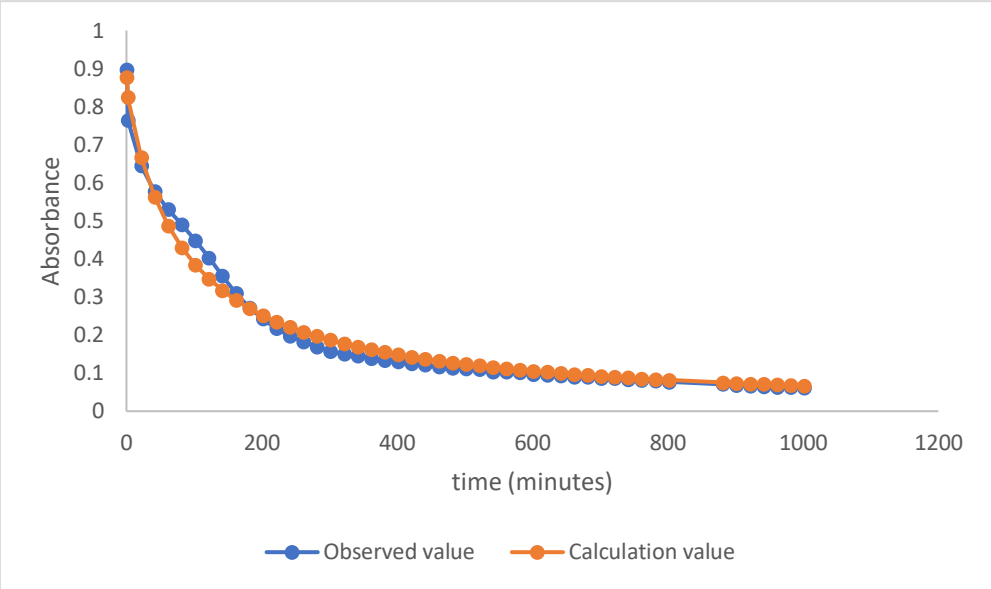

Figure 2.12. Comparison of observed data for hydrolysis of **2.1b** dissolved in a 20% DMSO and 80% phosphate buffer, v/v mixture vs. that calculated by simulation of Scheme 2.6.

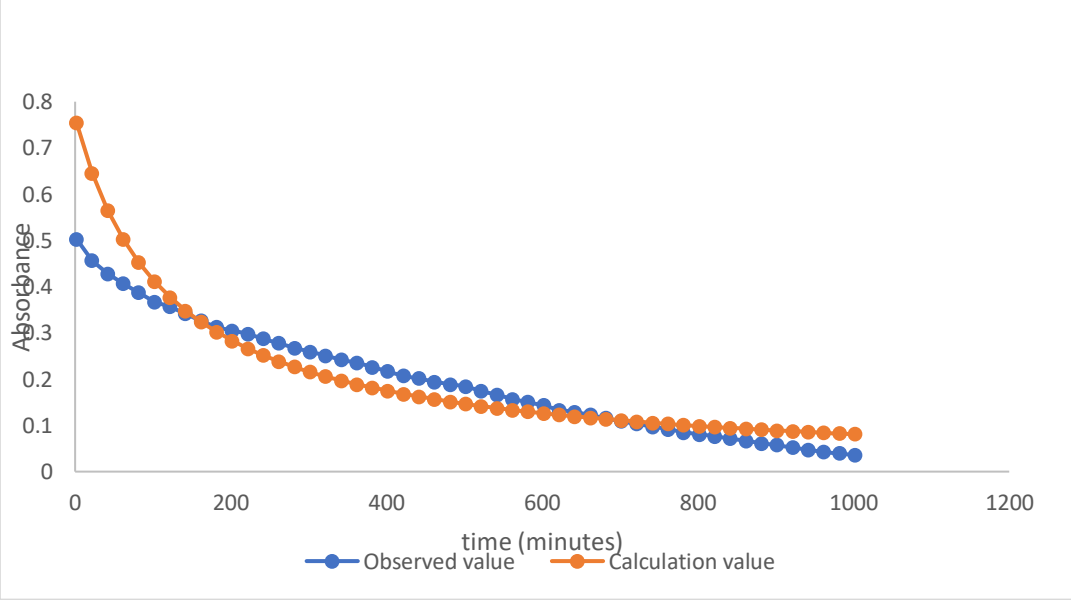

Figure 2.13. Comparison of observed data for hydrolysis of **2.1b** dissolved in a 20% DMSO and 80% acetate buffer, v/v mixture vs. that calculated by simulation of Scheme 2.6.

In the kinetics study of 20% DMSO 80% acetate buffer we saw significant hydrolysis at the start of the reaction in the first minutes leading to a poor fit to the models of Scheme 2.16. Thus,

Figure 2.13 shows that the simulation does not accurately reflect the true hydrolysis mechanism in the presence of acid. Presently, we do not have another proposal however.

Table 2.5. Rate constants determined by simulation of Scheme 2.6 to the data of Figures 2.8-2.13.

Hydrolysis conditions[a]	k_1 (min^{-1})	k_2 (μM^{-1} min^{-1})
Water	- (behaviour does not fit, see Figure 2.12)	- (behaviour does not fit, see Figure 2.12)
Phosphate buffer (pH 7.4)	0.694	0.000210
Acetate buffer (pH 5.0)	- (behaviour does not fit, see Figure 2.16)	- (behaviour does not fit, see Figure 2.16)
8 M urea	0.351	1.905×10^{-5}

[a] All studies carried out with [**2.1b**]$_{initial}$ = 76 μM in DMSO/aqueous mixtures of v/v composition 20:80, where 80% of the volume is the aqueous component.

For comparison hydrolysis in just water (Figure 2.9) the rate of hydrolysis of **2.1b** is accelerated, while that in 8 M urea (Figure 2.11) it is retarded. Protonolysis is a classical method to

accelerate the rate of hydrolysis reactions by improving the leaving group ability of the alkoxide and this may also account for the behaviour of Figure 2.13. On the other hand, urea is a very strong hydrogen bond donor/acceptor. One picture consistent with our studies is given in Scheme 2.7. Here complex **2.1b** undergoes partial hydrolysis to intermediate (**I**), that is in exchange with **2.1b** through re-coordination of ligand **2.2b**. If intermediate (**I**) dimerises it provides product (**P**) that is insoluble in the reaction medium. However, in the presence of urea (**I**) is stabilised by hydrogen bond formation, perhaps as in structure **2.6**. If this picture is true, then it is predicted that urea-based encapsulation in apoferritin will be more effective than pH switching strategies as it slows, rather than accelerates the hydrolysis process.

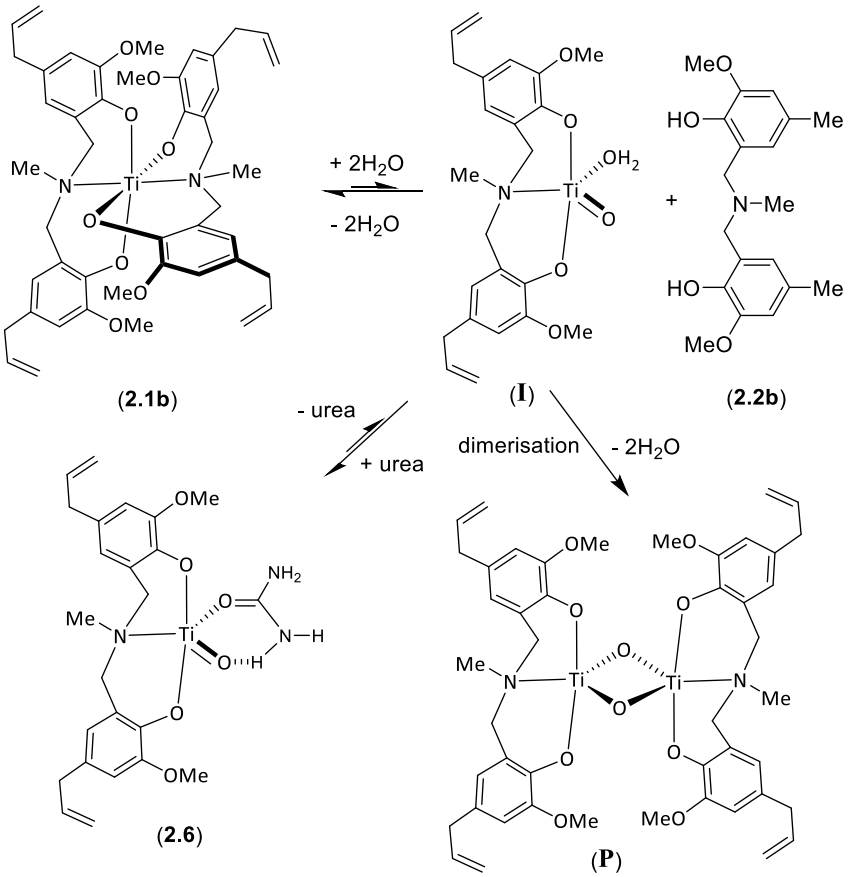

Scheme 2.7. Proposed mechanism of hydrolysis of complex **2.1b**.

2.5. Biological assay

2.5.1. MTT assay

An MTT assay was employed in this study to quantify the residual metabolic activity of PANC-1 pancreatic cancer cells after treatment with compound **2.1a** over a standard 72 h period at various dosing levels. It is important to acknowledge that the purity of the complex **2.1a** used in these experiments is only 80±4% by elemental and NMR analysis. This means that there is a potential for the derived GI_{50} values to be underrepresented, and that the possibility for cross-contamination from impurities in the **2.1a** sample exists. This is unfortunate, but within the timeframe of this project we did not have time to re-prepare **2.1a**. Fitting of the derived dose-response curves of Figure 2.8 provided GI_{50} values of 7±4 μM and >15±4 μM respectively for (**2.1a**) and cisplatin respectively. Musa reported GI_{50} value of 13.1±0.5 μM for cisplatin for PANC-1.[85] The GI_{50} of (**2.1a**) against PANC-1 was not reported by Musa, but the ethyl analogue of **2a** (Y = Et) provided a GI_{50} value of 1.9±0.2 μM against PANC-1. The allyl complex (**2.1b**) and fluoro (**2.1c**) gave related GI_{50} values against PANC-1 of 4.3±0.1 μM and 1.2±0.4 μM respectively. Abid reported GI_{50} values of 1.0 and 3.4 μM for (**2.1a**) against MCF-7 and HCT-116 cell lines respectively.[84]

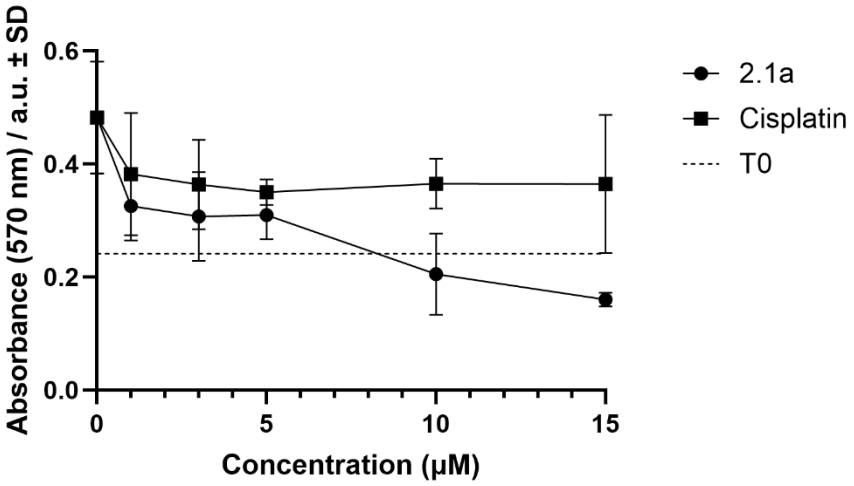

Figure 2.14. Dose-dependent response of PANC-1 cell proliferation when treated with (**2.1a**) and cisplatin as measured by MTT assay. Data shown as mean ±SD. n = 3. Compound **2.1.a** used in this study has a purity of 80±4%.

As can be seen in Figure 2.14, the dose-response MTT graph indicates that treatment with **2.1a** resulted in a concentration-dependent decrease in PANC-1 cell viability, consistent with growth-inhibitory activity towards this cell line. Previous research by Musa has shown that *bis*-phenolate amine titanium complexes of the type (**2.1**) have the ability to induce cell cycle arrest and DNA damage response by inducing reactive oxygen species (ROS) formation and DNA double-strand breaks (γH2AX).[85] This effect has been proposed to lead to caspase activation and downregulation of anti-apoptotic proteins (i.e. Bcl-2 and Mcl-1), which are involved in the MAPK signalling pathway and ER stress response, resulting in the apoptosis of the cancer cells. These mechanisms provide contextual insight into possible molecular mechanism of this compound, however there is no direct evidence present in this study. Therefore, further mechanistic investigation is needed to reveal the actual molecular mechanism of **2.1a**. The GI_{50} value estimated in this study for **2.1a** appears lower than the reported value for related compounds of this family. However, as indicated in Sections 2.2-2.3 our sample was of lower purity than that of Musa (80±4% based on the ^{1}H NMR spectrum of

the material used in these biological assays). The lower purity, assay conditions, and biological response might contribute to uncertainty in the GI_{50} value.

Figure 2.8 also appears to show that the positive control, cisplatin, exhibited relatively low growth inhibition towards PANC-1 pancreatic cancer cell lines (a GI_{50} value of >10 μM is estimated from Figure 2.8). Our cisplatin is comparable with the results of Musa,[85] who reported a GI_{50} value of 13.1±0.5 μM for cisplatin against PANC-1 (vs. our 15-20 μM depending on cisplatin source refer to Section 2.7.2). While these values are comparable, the inhibition observed in this study is lower than expected, suggesting potential biological or experimental factors influencing the assay outcomes.

We propose that this observation could be due to one of four possibilities: (i) a decomposed sample of cisplatin, (ii) mycoplasma bacterial contamination, (iii) development of a cisplatin resistant PANC-1, (iv) another unexplained contamination. Although the cisplatin degradation is considered unlikely given the use of fresh commercial sample, mycoplasma contamination might become the plausible contributing factor. Later in the project re-testing of our PANC-1 cell line (newly acquired from a commercial source) was revealed to be mycoplasma infected. However, at this stage we did not know this, as the PANC-1 cells came with certification asserting that they had passed all initial quality control checks. The possibility of cisplatin resistance within the original PANC-1 population cannot be excluded but was not directly assessed.

PANC-1 cells are known to have the ability to develop overexpression of ATP binding cassette (ABC) drug efflux transporters, including P-glycoprotein (MDR1) and MRP1. These effectively expel chemotherapeutic agents out of the cell, reducing intracellular drug accumulation. Additionally, the slower proliferation rate of PANC-1 cells makes it intrinsically less sensitive

to platinum agents. These characteristics may contribute to the cisplatin response in this study. In conclusion, the limitation in this study has implications into the uncertainty of the GI_{50} values obtained. Consequently, the results presented in this section are best interpreted as qualitative trends in growth inhibition rather than quantitative potency comparisons.

2.5.2. Clonogenic assay

Clonogenic assay are important technique in cancer biology to determine the ability of cancer cells to survive and proliferate after brief exposure to cytotoxic agent.[128] It is complimentary to MTT studies as it provides insight of the long-term (inherited) proliferative capability of cells and test agent cytotoxic properties that cannot be determined by MTT alone.

The effect of the **2.1a** on PANC-1 was assessed using a clonogenic assay. The cells were treated with several concentrations (1, 5 and 10 mM) of **2.1a** (of 80±4% purity) and suitable cisplatin positive controls over 24 h. All samples were then allowed to grow for 10 days in agent free medium. As shown in Figure 2.9b (plates labelled 'Media'), untreated control cells formed a very high number of colonies growth, while treatment with various concentration of **2.1a** significantly reduced colony formation in a dose-dependent manner. At a concentration of 10 μM, PANC-1 daughter colony formation was nearly eliminated, suggesting that the initial treatment of the cells with **2.1a** has dramatically reduced PANC-1 cell viability and subsequent colony formation.

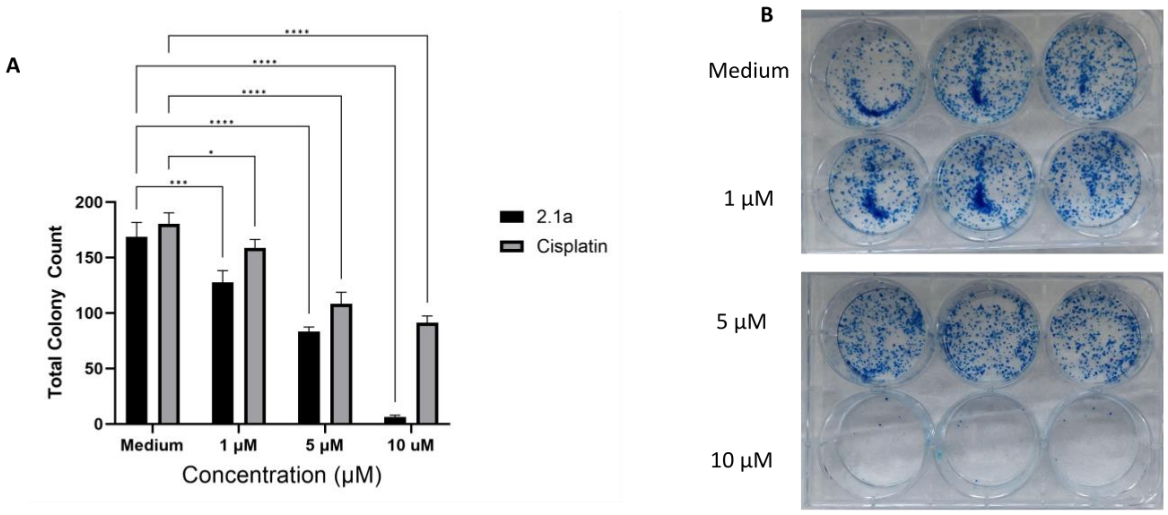

Figure 2.15. Effect of **2.1a** and cisplatin towards colony formation of PANC-1 cells (**A**) and PANC-1 colony growth response towards **2.1a** (**B**). Data shown as mean ±SD. *P < 0.05; ***P < 0.001; ****P < 0.0001 as compared with medium, n = 3.

A clear dose-dependent decline in formation of colony was observed in cisplatin treated cells, demonstrating its inhibitory effect as DNA-targeting agent that has a function in inhibition of cancer cell proliferation. On the other hand, Figure 2.15 shows that **2.1a** has significantly inhibition rate at 1 µM ($p < 0.05$), 5 µM ($p < 0.0001$), and 10 µM ($p < 0.0001$). This suggesting that compound **2.1a** not only affects immediate metabolic activity but also exerts sustained cytotoxic effects. The observed dose-dependent reduction in colony numbers indicates that even a short exposure to **2.1a** can lead to irreversible damage in clonogenic potential, potentially due to DNA damage.[128] This enhanced in activity was align with the result of the MTT data (see Section 2.5.1), confirming the higher activity of the compound in inhibiting cancer cell growth in long-term as compared with cisplatin. These findings are consistent with the proposed mechanism for the drug family **2.1** involving ROS generation and apoptosis induction.[85] Compared to conventional chemotherapeutic agents, like cisplatin, which also

impair clonogenic survival, **2.1a** appears to offer improved activity against PANC-1 cells, a cell line known for its high chemoresistance.[129]

Despite cisplatin's potent DNA-alkylating activity, the possibility exists that our PANC-1 sample might exhibit moderate intrinsic resistance, which can be attributed to multiple biochemical mechanisms already discussed. Additional mechanisms of resistance exist for PANC-1, including upregulation of the nucleotide excision repair (NER) pathways (that recognise and excise cisplatin–DNA adducts), and activation of anti-apoptotic proteins such as Bcl-2.[129,130] Additionally, as discussed in Section 1.7, reduced intracellular accumulation of cisplatin mediated by decreased expression of the copper transporter CTR1 and increased efflux via ATP-binding cassette (ABC) transporters could also limit the cytotoxic potential of cisplatin observed in our PANC-1 cells.[131]

2.5.3. Three-dimensional (3D) models of PANC-1

PDAC has highly disorganised tissue formation which involves a complex tumour microenvironment (TME) between tumour cells, stromal cells, extracellular matrix (ECM), and immunosuppressive microenvironment. These features contribute to the aggressive behaviours of PDAC and resistance therapies.[130] Thus, to further mimic PDAC tumour behaviour and tissue architecture, 3D models, in the form of spheroids, have been employed. These spheroids are simple 3D models of accumulated cancer cells *in vitro*, which allow the cells to interact with each other in a very simple tissue model. For example, developing nutrient and oxygen gradients are present as they are in *in vivo* tumours. Other characteristics such as drug resistance, hypoxia, or necrosis are also better modelled in spheroids. This allows the determination of more realistic cancer behaviour, including cancer stem cell behaviour,

tumour biology and cancer progression, as well as providing drug screening and chemoresistance study opportunities.[132]

We used **2.1a** in spheroid tissue models of pancreatic cancer, employing *in vitro* spheroid 3D PANC-1. Initially we optimised the formation of the PANC-1 spheroids by varying the initial seeding density. We found seeding density to be the most important factor in determining reproducible spheroid morphology, viability, and size. Such factors, of course, affect the downstream analysis such as drug screening.

Initial investigations revealed that the use of ultra-low attachment (ULA) plates strongly favoured the formation of reproducible spheroid models of PANC-1.[133] We propose this is because ULA plates are specifically designed to prevent cell-surface adhesion of the cels to well surfaces and thus encourage cells to undergo cell-to-cell interactions greatly facilitating spheroid formation. ULA wells achieve this through use of a highly hydrophilic non-ionic polymer, typically poly-HEMA (poly-2-hydroxyethyl methacrylate) that work to prevent cells adhering to the surface.[133–135] Finally, ULA round bottomed wells facilitate the use of buoyancy effects to gather cells into the middle of the plates, ensuring uniform and compact spheroid formation.[133]

In our experiment, PANC-1 cells were seeded in ULA 96-well plates at a range of densities: 500, 1000, 1500, 2000, 2500, and 3000 cells per well when determining optimal conditions of compact spheroid formation. Figure 2.10 shows the size and shapes of the PANC-1 spheroids as a function of time (24 and 48 h), providing a basis for selecting a suitable seeding density that has physiological relevance more faithfully mimicking the condition of tumour mass of a PDAC tumour mass.

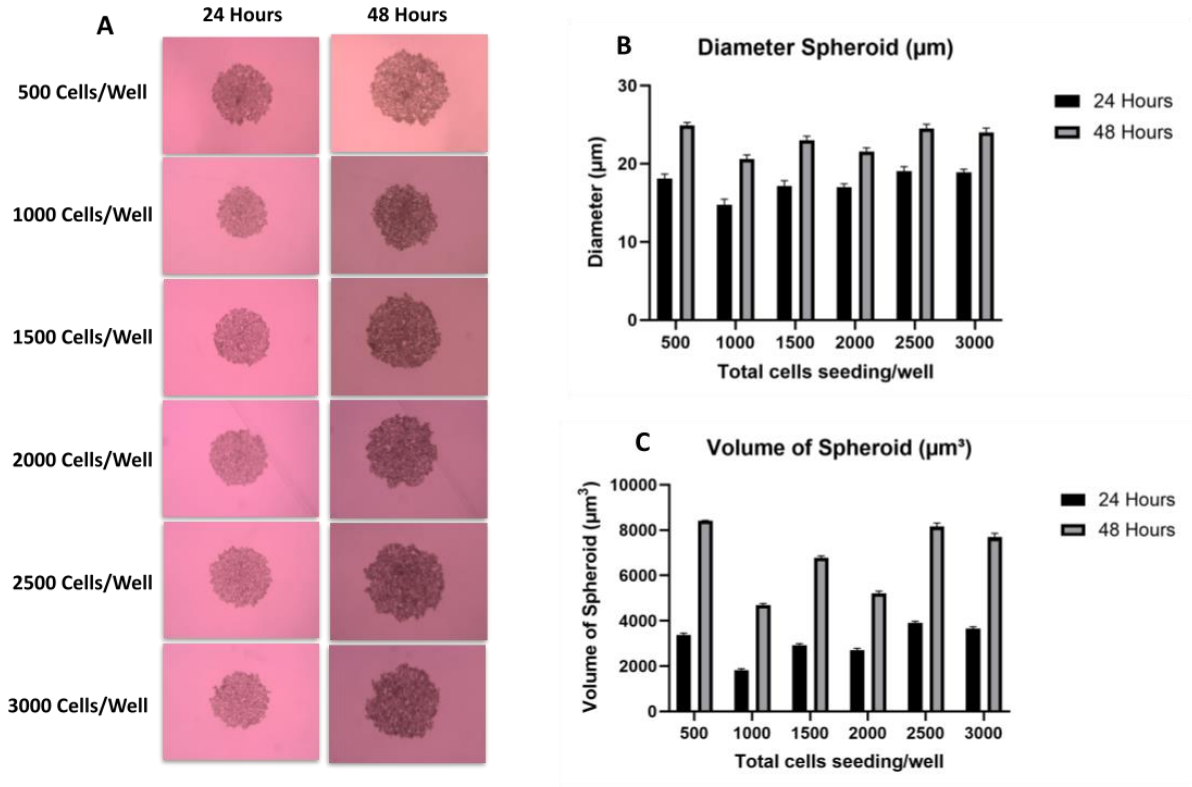

Figure 2.16. Effect of seeding density on PANC-1 3D spheroid formation. (**A**) Representative images of PANC-1 spheroids seeded at different densities: 500, 1000, 1500, 2000, 2500, and 3000 cells per well in ULA. Increasing seeding density resulted in spheroids with larger diameters and more compact morphology. Scale bar: 200 µm. (**B**) Growth of diameter of PANC-1 spheroids after 24 hours and 48 hours. (**C**) Growth of volume of PANC-1 spheroids after 24 hours and 48 hours. Data shown as mean ±SD n = 3.

Based on Figure 2.16, measurement of our PANC-1 spheroid diameters showed that there is no significant difference among the seeding density groups, indicating the initial seeding number did not overly influence the derived spheroid diameters. However, our data suggest that varied seeding densities does somewhat influence the volume of PANC-1 spheroid. Spheroids made from 2500 cells per well demonstrated the best (reproducible) results across

those conditions evaluated providing higher volume but compact morphologies. Spheroid volumes decreased and their structural integrity was less stable at both lower densities (≤2000 cells per well) and higher densities (3000 cells per well). Although the volume of spheroid made from 500 cells per well showed almost the same values as the spheroid made from 2500 cells per well, based on the picture shown, the spheroid still has some gaps (as determined by light passage) meaning that the spheroid is not dense.

Our results show that seeding density has an impact on spheroid diameter and this influences volume and morphology of the spheroid. Furthermore, our result suggest that diameter alone is not a sufficient indicator of spheroid quality, which consistent with previous reports[132] that emphasise the importance of volume and structure in assessing spheroid models.

At a seeding density of 2500 cells per well optimal cell-to-cell contact is observed in our system and this reflects balance between the cells, effective oxygen diffusion, effective nutrient uptake and overall distribution. A literature study suggests that oxygen has a limited diffusion distance (around 100–200 µm) in such tissue.[136,137] In well packed spheroids, oxygen can penetrate to almost all cells, resulting in uniform growth and viable compact structures of the spheroid. [138,139] However, if the spheroid is too large or the cell density is too high, sufficient oxygen cannot reach the core of the spheroid, leading to metabolic stress, hypoxia, and ultimately necrosis of the cells.[138,139] Similarly, nutrient uptake and distribution also contribute to the growth of spheroids. The effective distribution of amino acids, glucose, and growth factors depends on the diffusion characteristics of the spheroid,[138,140] which needs to be optimised to support cell proliferation and metabolism maintenance in large spheroids. This effect is not observed at lower seeding densities, due to insufficient intercellular interaction, resulting in reduction of nutrient utilisation.[141] In contrast, spheroids at higher densities cannot transfer nutrients essential for the growth of spheroid, because outer layer of cells

consume nutrients rapidly. This results in starving of the core cells and impaired spheroid integrity.

Our results align with previous findings confirming that the intermediate seeding density results in greater structural integrity and physiological relevance of for subsequent spheroids, compared with lower and higher initial cell denities.[132,142] Thus, we proceed at seeding densities of 2500 cells per well in our PANC-1 spheroid models as discussed in the next section.

2.5.4. Cytotoxicity analysis of 2.1a in 3D spheroid of PANC-1

Using PANC-1 spheroids from seeding densities of 2500 cells per well, we treated the subsequently fully developed PANC-1 spheroids (attained after 48 h) with cisplatin (1-10 μM) and with the test agent **2.1a** (1-10 μM). As shown in Figure 2.17 the PANC-1 spheroids typically increase in both volume regardless of the presence of cisplatin or **2.1a** (sample purity 80±4%) at concentrations below 10 μM. Interestingly, however, by day 3 after treatment of the initial spheroid with 10 μM of **2.1a**, the PANC-1 spheroid volumes are significantly decreased as compared with the medium-only control ($p < 0.0001$). Furthermore, the spheroids treated with 10 μM of **2.1a** showed reduced compactness (refer to Figure 2.17a). This is in stark contrast to the dose-dependent studies of PANC-1 spheroid tested with cisplatin that showed no effect at 10 μM. These results suggest limited activity for both agents (at concentration <10 μM) under our 3D culture conditions, with reduction of 82% of spheroid volume relative to control occurring at 10 μM after 72 hours of treatment with our titanium agent (**2.1a**).

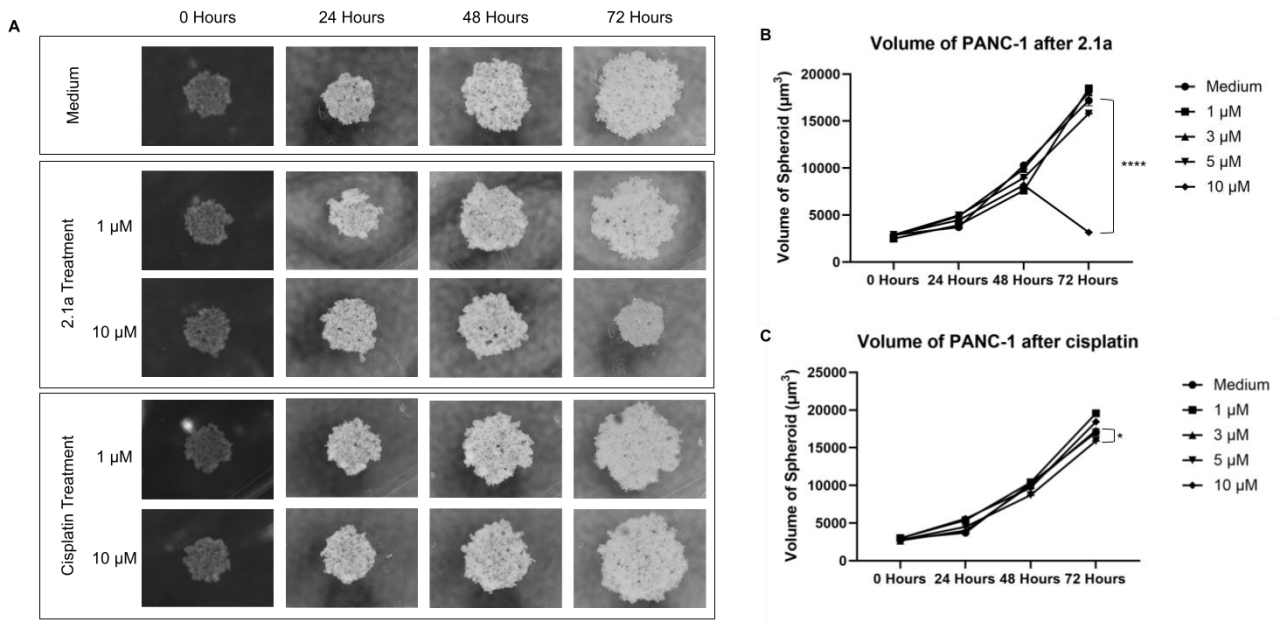

Figure 2.17. Cytotoxic studies on the growth of PANC-1 3D spheroid volume at agent concentrations of 1 µM, 3 µM, 5 µM, and 10 µM for cisplatin and complex (**2.1a**). (**A**) Representative images of PANC-1 spheroids after treatment with **2.1a** and cisplatin at concentration of 1 µM and 10 µM. (**B**) Volume of PANC-1 spheroid (in μm^3) after treatment with **2.1a**. (**C**) Volume of PANC-1 spheroid (in μm^3) after treatment with cisplatin. Data shown as mean ±SD. *P < 0.05; ****P < 0.0001, n = 3.

Several, non-exclusive mechanisms likely explain these observations: limited drug penetration in the spheroid, microenvironment driven chemoresistance, concentration-dependent cytostatic, and the role of oxygen and nutrient gradients in spheroids. Nevertheless, given the very poor precedent for drug action in PANC-1 tissues the activity of **2.1a** (which was 80±4% pure) is encouraging.

It has been shown that spheroids can develop gradients in oxygen, nutrients and extracellular matrix which further reduce penetration of small molecules and drugs penetration into the

core of the spheroid.[141] Compared to 2D cultures, this reduced penetration protects the core of the spheroid from drug exposure.

PANC-1 cells have been reported to express chemoresistance to various agents through multiple cellular mechanisms (i.e. drug efflux, DNA repair, altered metabolism).[67,143,144] In spheroidal shapes, cell-to-cell and cell-to-matrix contacts increasing hypoxia mechanism and nutrient-limited cores. These encourage stress responses and quiescence, which provide defence mechanisms against cytotoxic chemicals.[132] Furthermore, the lower concentration present at the centres of spheroids can result in lower cytostatic effects or different growth arrest mechanism without apoptosis, which fail to slow growth of the spheroid.[145,146] It is known that effective oxygen diffusion and nutrient distribution contribute in the mechanism of drug penetration to spheroids and clearly the outer proliferative layers are more exposed to the dissolved agent.[147] Thus, volumetric responses can reflect a complex interplay of drug concentration, penetration, and the spatially heterogeneous physiology of spheroids. However, in our case partial collapse of the spheroid architecture is achieved after long exposure to higher concentrations (10 µM) of complex (**2.1a**) leading to volume decrease and loss of compactness. Furthermore, at 10 µM of **2.1a**, the percent inhibition showing a higher inhibition rate on both diameter and volume of PANC-1. This can happen due to the loss of cell-cell contacts of the spheroid, leading to spheroid disintegration or the breakdown of 3D architecture of spheroid. It seems higher concentrations of **2.1a** are able to penetrate into the outer layer of spheroid, decreasing in ECM proteins (i.e. collagen and fibronectin), lead to loss of ECM integrity, loss of cell adhesion, and apoptosis of the cells.[148–150] This makes the spheroid volume reduce and become smaller in size (diameter and volume).[148–150] Thus, suggesting that

2.1a with high concentration are able to inhibit the growth of 3D PANC-1, resulting in shrinkage of volume of spheroid.

2.5.5. Cytotoxicity analysis of 2.1b in 3D spheroid of MCF-7 and MRC-5

When investigated by Musa,[82] complex (**2.1b**) showed high growth inhibitory and cytotoxicity towards many cancer cell lines, especially MCF-7 which provided a GI_{50} value of 2.4±0.2 µM from 2D MTT studies.[85] In our study we decided to investigate the effects of complex (**2.1b**) on the growth of cancerous (MCF-7) and non-cancerous (MRC-5) 3D spheroids 3D models as a comparison to our PANC-1 study. The effect of **2.1b** on the spheroid diameters and volumes are shown in Figure 2.19. In all cases these results are benchmarked against growth of the spheroids in the media alone, or in the presence of 1-10 µM cisplatin. This results further highlight different pharmacological behaviours for **2.1b** in 3D vs. 2D models of cancer cell lines.

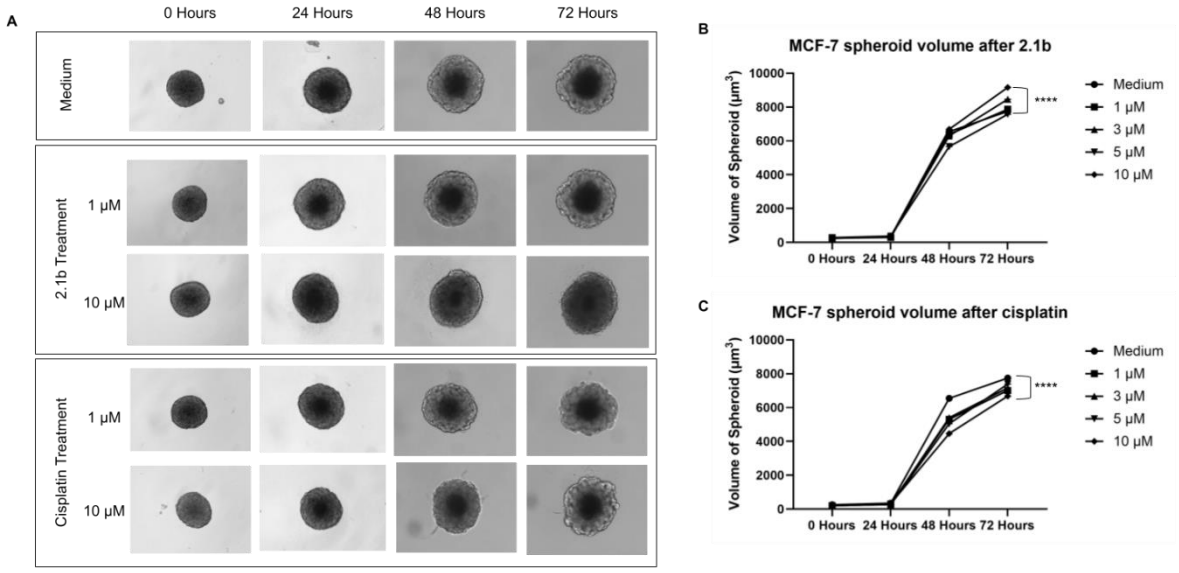

Figure 2.18. Cytotoxic studies on the growth of MCF-7 3D spheroid volume at agent concentrations of 1 µM, 3 µM, 5 µM, and 10 µM for cisplatin and complex (**2.1b**). (**A**) Representative images of PANC-1 spheroids after treatment with **2.1b** and cisplatin at

concentration of 1 µM and 10 µM. (**B**) Volume of MCF-7 spheroid (in μm^3) after treatment with **2.1b**. (**C**) Volume of MCF-7 spheroid (in μm^3) after treatment with cisplatin. Data shown as mean ±SD. ****P < 0.0001, n = 3.

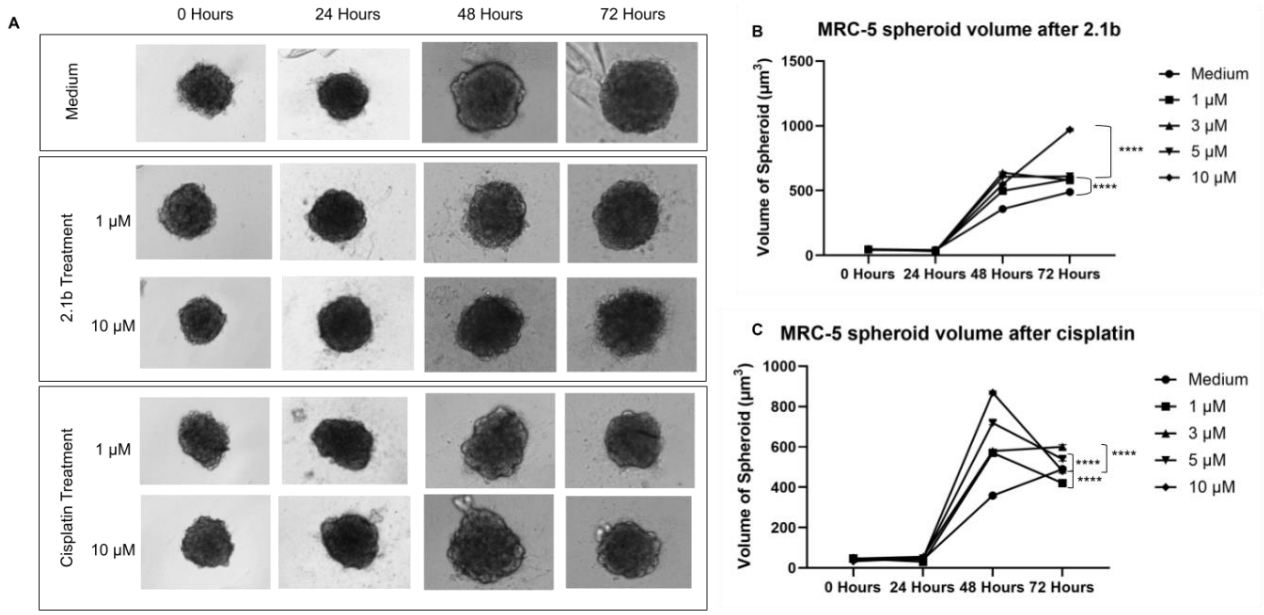

Figure 2.19. Cytotoxic studies on the growth of MRC-5 3D spheroid volume at agent concentrations of 1 µM, 3 µM, 5 µM, and 10 µM for cisplatin and complex (**2.1b**). (**A**) Representative images of MRC-5 spheroids after treatment with **2.1b** and cisplatin at concentration of 1 µM and 10 µM. (**B**) Volume of MRC-5 spheroid (in μm^3) after treatment with **2.1b**. (**C**) Volume of PANC-1 spheroid (in μm^3) after treatment with cisplatin. Data shown as mean ±SD. ****P < 0.0001, n = 3.

In Figure 2.18 and 2.19, study of MCF-7 spheroids treated with **2.1b** at different concentrations (1-10 µM) showed an increase in the volume of the spheroids in all cases progressively from day 0 to day 3. No significant differences are seen between the control and treatment groups. This suggests that complex (**2.1b**) did not induce measurable growth inhibition within the 72 hours treatment period.

Cisplatin treatment of MCF-7 spheroids (Figure 2.18C) shows an increase in both diameter and volume of the spheroid from day 0 to day 3). However, cisplatin reduced the growth of MRC-5 spheroids (Figure 2.19C), especially at later time points and higher doses, indicating toxicity toward non-cancerous fibroblasts. This aligns with cisplatin well-known side effects, such as nephrotoxicity and cytotoxicity in normal tissues.[151] This lack of selectivity emphasises the ongoing clinical challenge of balancing therapeutic efficacy with systemic toxicity.

In comparison spheroid treatment with **2.1b** does have negative inhibitory effects on either MCF-7 or MRC-5 (Figure 2.18A and Figure 2.19A) of our 72 days experiment, meaning the spheroid keeps growing, even in the presence of **2.1b** and cisplatin. In the presence of cisplatin, the growth of the spheroid in MCF-7 is accelerated, however, the growth of MRC-5 is slower. On the other hand, the presence of **2.1b** showing its ability to slow down the growth of spheroid in MCF-7 cells and increase the growth of MRC-5. This suggests that **2.1b** have drug selective mechanisms towards cancerous cells and low growth inhibition towards MRC-5 as compared with cisplatin. Thus, while **2.1b** shows promise as a chemo-preventive agent in 2D studies, this was not fully extended to our own 3D work. Overall, our results suggest that **2.1b** may have limited direct cytotoxicity in tissues and that an improved formulation of it is needed to ensure its *in vitro* MTT activities could be delivered in a therapy. While cisplatin retains its effective tumour suppression activity in spheroids it also still exhibits non-selective cytotoxicity, underscoring the need for improved metal-agents or targeted delivery systems in clinical applications.[151,152]

2.5.6. PANC-1 TfR-1 expression

As discussed in Section 1.11 transferrin transports iron into cells needing it, while ferritin stores iron inside those cells, releasing it when required. Transferrin receptors (TfRs),

especially TfR-1, are vital proteins involved in normal cellular iron uptake. In the case of pancreatic ductal adenocarcinoma, transferrin receptor levels are elevated.[153] As iron uptake forms a vital part of our strategy to use apo-ferritin to deliver titanium agents (**2.1**) we sought to confirm that our PANC-1 cell line have over expression of TfR-1.

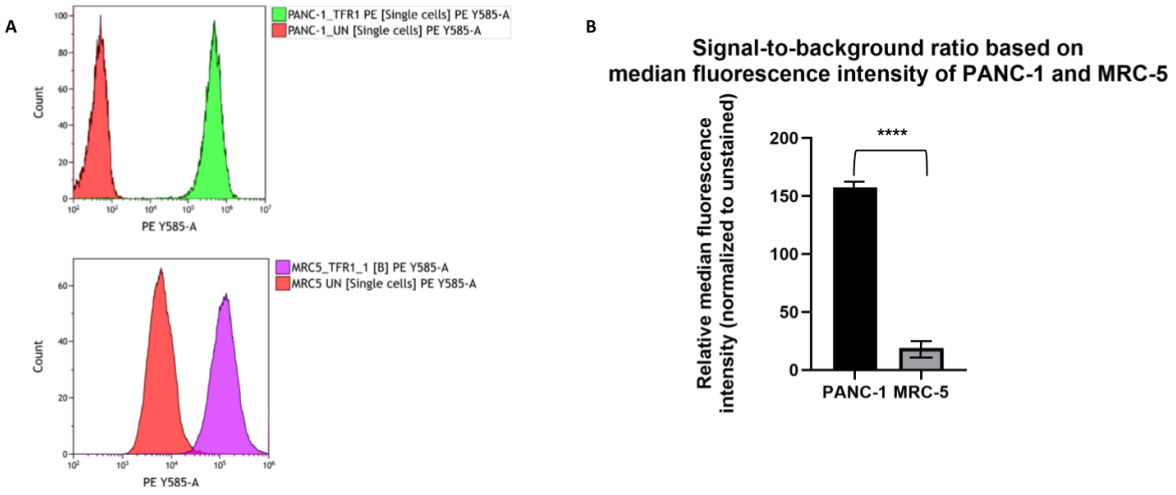

Figure 2.20. Expression of TFR-1 in PANC-1 cell line and MRC-5[154]. (**A**) Representative flow cytometry histograms showing TfR-1 expression in PANC-1 (top) and MRC-5 (bottom) cells. Red indicates unstained control cells. Green (PANC-1), purple (MRC-5) indicate cells with antibody conjugated with PE, CD71 (Transferrin Receptor) Monoclonal Antibody (OKT9 (OKT-9)), PE, eBioscience™. (**B**) Quantification of TfR-1 expression shown as signal-to-background ratios calculated from the median fluorescence intensity (MFI) of stained samples normalised to unstained controls. PANC-1 exhibit higher TfR-1 expression as compared to MRC-5. ****P < 0.0001. The value represents single representative experiment with n=10,000 events.

TfR-1 expression in PANC-1 was determined by flow cytometry (Figure 2.20). Quantification of the TfR-1 expression was performed by calculating the ratio of median fluorescence

intensity of TfR-1 stained samples to unstained controls, normalising for background autofl1-stainede (Fiugre 2.20B). Using a signal-over-unstained normalisation, PANC-1 TfR-1 stained cells exhibit 158-fold higher median fluorescence intensity as compared to the unstained control. Normal human lung fibroblast cells (MRC-5) are used further as a control for TfR-1 expression. MRC-5 cells exhibit 18-fold higher median fluorescence intensity as compared to their unstained control. MRC-5 cells were found to have a low expression of TfR-1, suggesting only normal levels of basal iron uptake consistent with this cell line's non-cancer phenotype. In contrast, refer to Figure 2.20B, PANC-1 has higher TfR-1 median fluorescence expression, which in line with the elevated iron requirements linked to aggressive tumour growth and chemoresistance and the supports PANC-1 cellular processes receive through enhanced iron levels when under survival stress. Collectively, these flow cytometry data confirm that TfR-1 expression is substantially increased in PANC-1 as compared to MRC-5, supporting its suitability as the target therapy of apoferritin-mediated drug delivery.

2.5.7. Attempted encapsulation of titanium complex (2.1a) in apoferritin

A standard pH-dependent disassembly/reassembly protocol has been adopted to encapsulate complex **2.1a** into apoferritin.[155] HSAFt is initially subjected to acidic conditions (pH ~2.0) to induce cage disassembly. After buffering the resultant hydrolysed protein to pH 5, we then added titanium complex (**2.1a**, 1.5 μM, 150 equivalents vs. the HSAFt). The solution was then gradually neutralised to pH 7.4 over 1 h using sodium acetate buffer to promote reassembly of the protein nanocage, aiming to trap the titanium complex (**2.1a**) within the protein's internal cavity. To gain insights into whether our attempts to encapsulate **2.1a** within the protein had been successful we undertook Native PAGE analysis of the protein compositions after the attempted encapsulation (Figure 2.21).

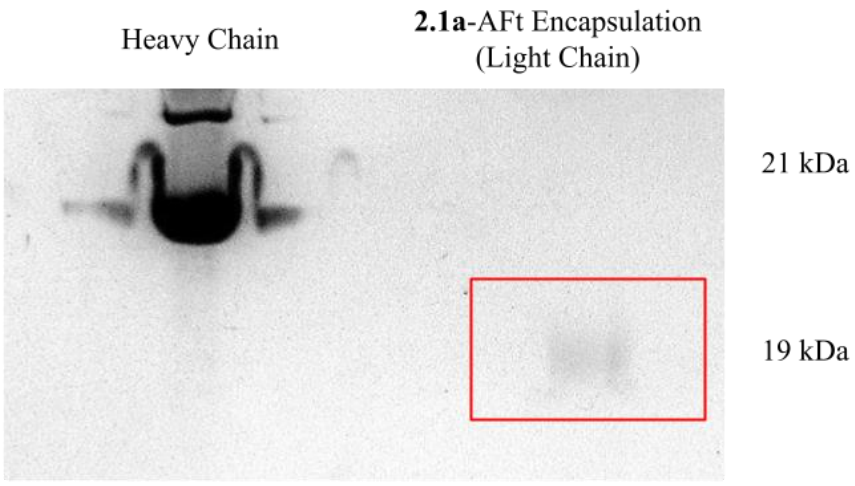

Figure 2.21. Native PAGE analysis of HSAFt subunits in the presence of **2.1a.** The heavy chain (21 kDa, left lane) and light chain (19 kDa, right lane) were analysed under non-denaturing conditions. Titanium content within AFt was assessed separately by ICP-MS (Table 2.6).

Native PAGE resolves proteins based on charge and conformation and does not directly detect the presence of titanium inside of the cage. Titanium content was therefore assessed independently by ICP-MS. Following attempted encapsulation, native PAGE (Figure 2.21, right-hand lane) indicates that HSAFt remains detectable under non-denaturing conditions, suggesting partial recovery of HSAFt subunits after the encapsulation. The band of the samples (right lane, indicated by the red square) have a molecular weight approximately 19 kDa corresponds to the light-chain subunit, indicating that the recovered material consists predominantly of L-chain HSAFt. This is consistent with the known subunit composition of HSAFt reported in the literature.[156]

Table 2.6. ICP-MS analysis of **2.1a** inside of HSAFt. Titanium content inside of HSAFt is below the detection limit (10 ppb) in both HSAFt and attempted **2.1a** encapsulation conditions. Standards used for calibration are shown.

Sample	Titanium ICP-MS
HSAFt alone (controls)	< 10 ppb
2.1a-HSAFt encapsulated	< 10 ppb
Standard calibrations at:	10 ppm, 1 ppm, 100 ppb, 10 ppb, 1 ppb

We used ICP-MS in an attempt to detect the presence of **2.1a** inside of the cage (Table 2.6). ICP-MS analysis (Table 2.6) shows that titanium levels remain below the detection limit. Thus, ICP-MS data suggest no titanium is present. The HSAFt protein band in our PAGE study is also smeared after encapsulation, consistent with its aggregation or denaturation compared to the original protein. Reasons for this could include the fact that HSAFt proteins are known to exhibit poor stability after low pH or metal hydrolysis.[157,158] Our data align with previous studies suggesting that HSAFt is not suitable for pH encapsulation protocols, due to the low pH procedures degrading the HSAFt protein.[157] Hydrolysis of (**2.1a**) is also a likely factor contributing our failure to encapsulate our complex. As shown in Section 2.4 complexes of type **2.1a** are rather rapidly hydrolysed first to an intermediate and then an insoluble product. This is not compatible with the days long procedure associated with pH-controlled HSAFt drug encapsulation. During attempted encapsulation of (**2.1a**) in HSAFt similar yellow precipitates to those seen in the hydrolysis studies of Section 2.4 were noted in the dialysis bags used for our procedures. Thus, it appears that different conditions will be needed for encapsulation of

2.1a or a related complex. Current research is being conducted in hydrolysis and kinetics of titanium complex in several aqueous solutions (refer to Section 2.4) to identify these conditions. Our current work suggests that our titanium complex is stable under 8 M urea, suggesting urea as an encapsulation method compatible with our titanium complex's properties. Unfortunately, there was insufficient time in the present project to investigate this hypothesis.

2.5.8. Conclusion

The ligand 6,6'-((methylazanediyl) *bis*(methylene))*bis*(2-methoxy-4-methylphenol) (**2.2a**) was synthesised. However, it also resulted in the isolation of 8-methoxy-3,6-dimethyl-3,4-dihydro-2*H*-benzo[e][1,3]oxazine (**2.4**). This affected both the yield and the purity of the complex **2.1a** isolated. Initial attempts to encapsulate our titanium complex **2.1a** into HSAFt using a standard pH dependent re-assembly method led to no detectable titanium (ICPMS) species within the apoferritin cage. A subsequent hydrolysis study of related **2.1b** revealed that such titanium complexes are not stable in aqueous and low/high pH conditions. In contrast, the titanium complex **2.1b** is much more stable under 8 M urea conditions, making that a potentially suitable environment for titanium encapsulation. In conclusion, the hydrolysis study of **2.1b** and **2.1c** suggested dimerisation and decomposition of titanium complex under several conditions, with urea as the best compromise to stabilise such titanium complexes.

The activities of the **2.1a** were tested against 2D PANC-1 pancreatic cell lines using MTT and clonogenic assays, as well as 3D PANC-1 spheroids. The MTT results show both complexes have GI_{50} values of around 7 µM, which is lower than cisplatin (used as a positive control). Clonogenic assay of **2.1a** also show that it has a cytotoxic effect, which disrupts PANC-1 colony formation. Furthermore, 3D PANC-1 spheroid growth has been established at an initial seeding

density of 2500 cells per well. This is proposed to mimic small pancreatic tumour environments in the human body. At 10 µM **2.1a** 3D PANC-1 spheroid growth slowed within 72 hours in lower concentrations. In contrast, cisplatin has no effect. This might make complex **2.1a** a promising anti-pancreatic cancer lead, even though our studies were conducted with impure complex.

2.5.9. Future Work

Further study needs to carried out on the encapsulation of the titanium complexes using apoferritin protein loading using 8 M urea, as our studies show these titanium complexes lead to intermediates that are stable in 8 M urea condition vs. the decomposition seen in other solvents. Attaching an appropriately placed urea-like donor group to the ligand **2.2** of the titanium complex could be an alternative pathway to increase the stability of the complex (or its derived intermediate) in aqueous solutions. Furthermore, the titanium complexes used in biological studies need to be pure, so the activity of our experimental agent **2.1a** needs to be revised.

In the biology area, future research needs to be conducted in 3D cell models subjected to titanium complexes to assess their activity against PANC-1 cells. Specifically, **2.1a**'s apparent significant activity in PANC-1 spheroids at 10 µM needs to be confirmed. This should be done using presto blue assay analysis, as quantitative measurement for the growth of PANC-1. Additionally, ATP assays might be adopted to explore compound cytotoxicity and efficacy, because these are a sensitive and robust assay for high-throughput screening. Finally, for qualitative agency-penetration study, assessing 3D models with fluorescent dyes is an alternative to observe the structure of the spheroid without fixation.

2.6. General experimental

2.6.1. General chemistry experimental

Moisture-sensitive reactions were carried out under nitrogen atmospheres using flame-dried Schlenk apparatus. All temperatures refer to the usage of the thermostatic cooling/heating baths (±1°C), including kinetics studies. All solvents used for moisture-sensitive reactions were dried over 4 Å molecular sieves prior to use. Thin layer chromatography was done using foil-backed plates coated with Merck silica gel 60 F_{254} (Merck, Germany). The plates were visualised using ultraviolet light and an alkaline potassium permanganate solution. Liquid chromatography was carried out using forced flow or flash column techniques with the solvent systems mentioned in the procedure. The stationary phase of the column was silica gel 60 (220-240 mesh) (Fluorochem, United Kingdom). Nuclear magnetic resonance spectra were recorded on Bruker AV(III)400 (400.1 MHz), Bruker AV400 (400.1 MHz), or Bruker Ascend™ 400 (400.1 MHz) spectrometers at room temperature. Chemical shifts are reported in parts per million (ppm) and were referenced to residual solvent peaks based on the values provided on MestReNova software. Coupling constants (*J*) are reported in Hertz (Hz) using the following abbreviations: br (broad), s (singlet), d (doublet), t (triplet), q (quartet), m (multiplet), and app (apparent). UV-vis spectra and kinetic studies were carried out on a Carey 5E spectrometer using its bespoke software.

2.6.2. General procedure A – synthesis of ligands (2.2)

Phenols (1 equiv.) were dissolved with stirring in methanol (10 mL). Subsequently, 37% w/w aqueous formaldehyde in water (3 equiv.) was added followed by 40% w/w methylamine in water (2 equiv.) to the stirred mixture. The final mixture was stirred at room temperature for 36 h and then at 65 °C for 4 h. The final mixture was cooled and then evaporated under reduced pressure to produce concentrated crude extract. The crude extract was purified using column chromatography (EtOAc/cyclohexane 1:1.5) to obtain the ligand fractions. The resulting material was crystallised from saturated ambient temperature of Et_2O/pentane (1:4) solutions upon cooling in 4 °C to afford analytically pure materials.

2.6.2.1. Attempted preparation of 6,6'-((methylazanediyl) *bis*(methylene))*bis*(2-methoxy-4-methylphenol) (2.2a) resulting in isolation of 8-methoxy-3,6-dimethyl-3,4-dihydro-*2H*-benzo[e][1,3]oxazine (2.4)

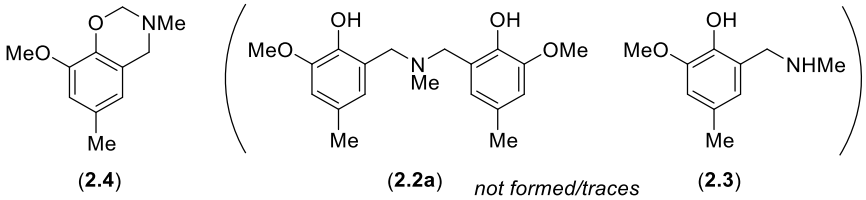

(**2.4**) (**2.2a**) *not formed/traces* (**2.3**)

Synthesised attempted according to General Procedure A using 2-methoxy-4-methylphenol (1.00 g, 7.23 mmol), 37% w/w aqueous formaldehyde in water (1.5 mL, 18.5 mmol), 40% w/w methylamine in water (1.1 mL, 14.1 mmol), and methanol (10 mL) as solvent. colourless needles were attained 0.725 mg, 4.04 mmol, 63%) that X-ray crystallography revealed to be benzoxazine (2.4)**. Mp** 59-60 °C**; ^{1}H NMR** (500.1 MHz, $CDCl_3$): δ_H 6.56 (s, 1H, ArH), 6.39 (s, 1H, Ar*H*), 4.85 (s, 2H, OCH_2), 3.91 (s, 2H, OCH_2), 3.86 (s, 3H, OCH_3), 2.61 (s, 3H, NCH_3), 2.26 (s, 3H, CH_3**^{13}C NMR** (125.0 MHz, $CDCl_3$): δ_C 147.5 (C), , 140.9 (C), 129.6 (C), 120.1 (C), 19.6 (CH), 110.5

(CH), 84.3 (CH_2), 56.0 (CH_2), 51.9 (OCH_3), 40.0 (NCH_3), 21.3 (CH_3). **ATR**: 2991, 2953, 2899, 1670, 1589, 1498, 1468, 1450, 1409, 1378, 1349, 1317, 1290, 1275, 1227, 1205, 1187, 1148, 1136, 1096, 1084, 1052, 1032, 1017, 982, 963, 944, 915, 856, 845, 823, 791, 751, 737, 715, 686, 607, 586, 537, 512, 474, 450. **HRMS** $(M+H)^+$ Calcd. for $C_{11}H_{16}O_2$ 194.2502, found 194.1179 ($|\sigma|$ = 6 ppm).

2.6.2.2. 6,6'-((Methylazanediyl)*bis*(methylene))*bis*(4-allyl-2-methoxyphenol (2.2b)

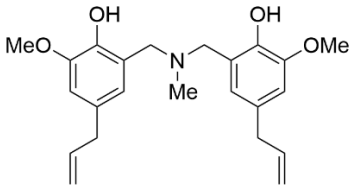

This compound was provided by Dr Mustapha Musa. Its purity was confirmed by ^{1}H NMR spectroscopy before use. The data attained were concordant with the published values.[85]

2.6.2.3. 6,6'-((methylazanediyl)bis(methylene))*bis*(4-fluoro-2-methoxyphenol) (2.2c)

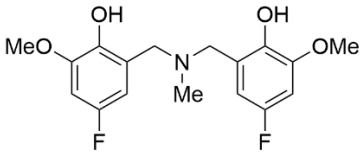

This compound was provided by Sarah Pryle. Its purity was confirmed by ^{1}H NMR spectroscopy before use. The data attained were concordant with the published values.[85]

General procedure B – Synthesis of titanium complexes (2.1)

The reaction was conducted under the nitrogen atmosphere using dray solvents. Bisphenolate ligand (**2.2**, 1 equiv.) was dissolved in toluene (0.6 mL per mmol of **2.2)** and stirred until fully

dissolved. Neat titanium (IV) isopropoxide (0.6 equiv.) was added to the mixture which was stirred at ambient temperature (4 h). During this time the reaction became deep orange in colour. The solvent was removed using trap-trap distillation techniques providing **2.2** as orange solids. Analytically pure materials were attained by liquid-liquid recrystallisation using suitable solvents, as described in the individual cases.

2.6.2.4. *Bis*((2,2'-((methylimino-N)*bis*(methylene))*bis*(4-methyl-6-methoxylphenolato-O)))titanium(IV) (2.1a)

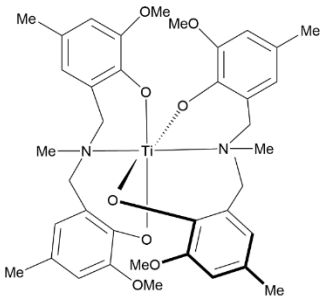

Synthesise according to General Procedure B using **2.2a** (100 mg, 0.13 mmol) and titanium (IV) isopropoxide (600 µL, 2.02 mmol) to afford orange solid compound with a yield similar to the literature prepartion.[76] **^{1}H NMR** (500.1 MHz, $CDCl_3$): δ_H 6.61 (d, 1H, *J* = 1.8 Hz, ArH), 6.54 (d, 1H, *J* = 1.8 Hz, ArH), 6.47 (d, 1H, *J* = 1.8 Hz, ArH), 6.44 (d, 1H, *J* = 1.8 Hz, ArH), 4.85 (d, 1H, *J* = 12.8 Hz, CH_aH_b), 4.77 (d, 1H, *J* = 12.8 Hz, CH_aH_b), 3.46 (s, 3H, ArOCH_3), 3.41 (d, 1H, *J* = 12.8 Hz, CH_aH_b), 3.32 (s, 3H, ArOCH_3), 3.30 (d, 1H, *J* = 12.8 Hz, CH_aH_b), 2.55 (s, 3H, NCH_3), 2.30 (s, 3H, ArCH_3), 2.24 (s, 3H, A*r*CH_3). **^{13}C NMR** (125.0 MHz, $CDCl_3$): δ_C 150.7 (C), 150.6 (C), 146.4 (2 x C), 127.1 (C), 126.9 (C), 124.6 (C), 123.7 (C), 124.4 (CH), 124.3 (CH), 113.0 (CH), 112.6 (CH), 46.6 (CH2), 46.4 (CH_2), 55.7 (2 x CH_3), 44.0 (NCH_3), 21.1 (CH_3), 21.0 (CH_3); $\boldsymbol{\nu_{max}}$ (neat): 2981, 2912, 2850, 2832, 1580, 1485, 1457, 1259, 1154, 1100, 982, 928, 822, 581, 556, 530, 405 cm-1; **HRMS** found 729.2624 (M+Na)+ Calcd. for $C_{38}H_{46}N_2O_8Ti$ 729.2626 (|σ| = 0.3 ppm); **elemental**

analysis Calcd. (%) for $C_{38}H_{46}N_2O_8Ti$: C, 64.59; H, 6.56; N, 3.96; found: C, 64.31; H, 6.67; N, 3.90. The compound was recrystallised from (4:1 pentane:ether).[84]

2.6.2.5. Synthesis of *Bis*((2,2'-((methylimino-N)*bis*(methylene))*bis*(4-allyl-6-methoxyphenolato-*O*)))titanium(IV) (2.1b)

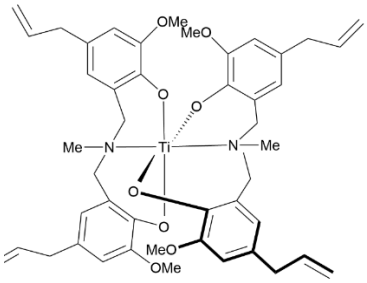

This compound was provided by Dr Mustapha Musa. Its purity was confirmed by ^{1}H NMR spectroscopy before use. The data attained were concordant with the published values.[85]

2.6.2.6. Synthesis of *Bis*((2,2'-((methylimino-N)*bis*(methylene))*bis*(4-fluoro-6-methoxyphenolato-*O*)))titanium(IV)2.1c

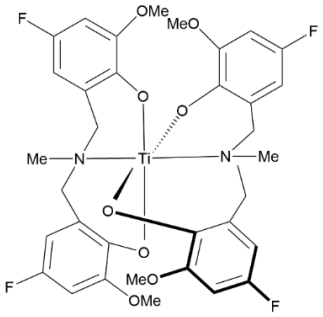

This compound was provided by Sarah Pryle. Its purity was confirmed by ^{1}H NMR spectroscopy before use. The data attained were concordant with the published values.[85]

2.6.3. Hydrolysis studies of titanium complex (2.1b and 2.1c)

2.6.3.1. Standard solutions

Analytically pure samples of (**2.2b**), typically 1-2 mg as required, were weighed to ±0.0005 mg accuracy using a Sartorius CPA26 micro balance into a 2 mL glass vial. Using a thermos scientific finnpipette 1000 µL (accurate to ±0.01 mL) The weighed sample of (**2.2b**) was transferred to a 25 mL volumetric flask using DMSO (5 × 1.00 mL aliquots) to ensure complete transfer of (**2.2b**). Subsequently, the orange DMSO solution was diluted to 25 mL with one of four different aqueous phases: (i) Deionised water, (ii) 8 M aqueous urea, (iii) 0.1 M acetate buffer pH 5, (iv) 0.1 M phosphate buffer pH 7.4, (v) 0.08 M hydroxide-glycine buffer pH 10. Details of how each of these solutions were prepared is given below. Solutions of up to ca. 76 µM in (**2.2b**) could be prepared this way and appeared as pale-yellow solutions (except in the case of 0.08 M hydroxide-glycine buffer pH 10 use) where instant decolouration was observed. For kinetic studies the kinetic clock was started as the first aqueous component was added.

2.6.3.2. Solution preparation

2.6.3.2.1. Deionised water

The deionised water was obtained from ELGA PURELAB Option water purification system with DV35 storage reservoir (ELGA LabWater, United Kingdom) and was boiled in temperature of 100^{o}C.

2.6.3.2.2. 8 M aqueous urea

Urea with weight of 12 gram was inserted into 25 mL volumetric flask and distilled water was made up to 25 mL to prepare 8 M aqueous urea.

2.6.3.2.3. 0.1 M acetate buffer pH 5

To make 0.1 M acetate buffer pH 5, 288.6 mg of sodium acetate was inserted into 50 mL volumetric flask. Then 40 mL of distilled water was inserted into the same volumetric flask to dissolve sodium acetate. After that, 88.9 mg acetic acid was added into solution. The pH was measured with pH electrode inlab expert pro-ism xerolyt and adjusted to pH 5 using drops of 2 M HCl. Distilled water was then added until the total volume is 50 mL.

2.6.3.2.4. 0.1 M phosphate buffer pH 7.4

To make 0.1 M phosphate buffer pH 7.4, 1.0107 gram of sodium phosphate dibasic heptahydrate was inserted into 50 mL volumetric flask following the addition of 169.7 mg sodium phosphate monobasic into the same volumetric flask. Then 40 mL of distilled water was inserted into the same volumetric flask to dissolve both compounds. The pH was measured with pH electrode inlab expert pro-ism xerolyt and adjusted to pH 7.4 using drops of 5 M NaOH. Distilled water was then added until the total volume is 50 mL.

2.6.3.3. Kinetic studies

Freshly prepared DMSO/aqueous component (20:80 v/v) mixtures were transferred to a sealed UV-vis cuvette and transferred to a thermally equilibrated (22 ±1 ^{o}C) Cary 5000 UV-vis spectrometer. A cuvette containing the same 20:80 solvent mixture, but without (**2.1b**) was used in the spectrometer's reference beam. Spectra (270-700 nm) were collected either in automation modes, or manually, over periods of 1 h to 1 week. Spectra data were exported into a .csv files and processed as described below.

All the rough data was combined into one file and arranged according to their time point. All of the data was zeroed in 632 nm, because 632 nm has the lowest point as compared with

entire wavelengths. The peak (380 nm) then was chosen and arranged based on their time point. The clean 380 nm data was then inserted into Scheme 2.6. The absorbance and the simulation value was then compared, and the plot was fitted using Solver tools from excel.

2.7. Biological experimental

2.7.1. Cell culture and maintenance of PANC-1 cell line

Human PANC-1 cell line (ATCC, USA) was maintained as batches of 0.3 to 1 × 10^6 cells in complete Dulbecco's Modified Eagle Medium (DMEM) of a supplemented version there of (cDMEM). The cDMEM medium was prepared from Dulbecco's Modified Eagle Medium (DMEM from Thermo Fisher, USA) by addition of 10% Fetal Bovine Serum (Thermo Fisher, USA). The PANC-1 cells were maintained in a T75 flask, typically at 3 × 10^5 cells/mL, inside a 37°C/5%/CO_2 incubator. After a week the cells had typically reached approximately 80% confluence. At this point the cells were washed with sterile phosphate buffer saline or PBS (Thermo Fisher, USA) and was introduced with trypsin (Thermo Fisher, USA) for detaching the cells. After 5 minutes, fresh cDMEM was inserted to stop the trypsin activity and the cells were centrifuged in 400G for 5 minutes. After that the cells were counted and the number of cells mentioned above were growth in the flask for maintenance.

2.7.2. MTT assay

MTT Assay was used to determine the growth of PANC-1 cell lines under the treatment of the titanium complex (**2.1a**). This technique was adapted from the procedure from Mosmann (1983).[121] The PANC-1 cells were seeded at 5000 cells per well and were incubated for 24 hours in 37 °C 5% CO_2 to allow cells to adhere properly in the well. After 24 hours, a T_0 value was obtained by performing the MTT assay in control wells as a baseline measurement before

adding the treatment agents to measured wells. Cisplatin was purchased from Merck Millipore (Burlington, MA, USA) and was used as a positive control. Both cisplatin and the titanium complex (**2.1a**) were stock solutions at 1.00 mM in DMSO. Serial dilutions of cisplatin and the titanium complexes were performed with cDMEM to achieve desire concentrations. This was achieved within 10 mins and the solutions freshly used. The final concentration of DMSO was ≤0.1% v/v, which is at the safe level for cell culture. The PANC-1 cells then were treated with concentrations of cisplatin and titanium complexes ranging 1-15 μM and were incubated for 72 hours in 37 °C 5% CO_2. After 72 hours, the media were aspirated and 2 mg/mL of MTT solution were added. After the addition of the MTT solution, the cells were incubated for 3-4 hours to allow the metabolic activity of the MTT solution to purple formazan by the live cells. Finally, the MTT solution was removed and DMSO (50 μL) added to the cells to solubilise the formazan precipitation of the cells. The absorbance was read at 570 nm wavelength in Tecan Spark 10M Microplate Reader.

2.7.3. Clonogenic assay

A clonogenic assay was used to determine the ability of cells to form colonies. The PANC-1 cells were seeded at 250 cells/wells and were incubated for 24 hours at 37 °C/5%/CO_2 to allow proper adhesion of the cells. Cisplatin (positive control) and the titanium complex (**2.1a**) stock solutions were prepared at 1.00 mM in DMSO. Serial dilutions of cisplatin and the titanium complexes were performed in the cDMEM to achieve 0 μM, 1 μM, 5 μM, and 10 μM. The final concentration of DMSO was ≤0.1% v/v, which is appropriate for reproducible cell culture. After the initial 24-hour attachment period, cells were treated with of the assayed cisplatin or titanium complex (**2.1a**) agent solutions (1 μM, 5 μM, 10 μM). The treated wells were incubated for 24 hours at 37 °C/5%/CO_2. Following this the treatment media were removed,

and the wells were gently washed twice with 1 mL of fresh media to remove any residual agent. Fresh cDMEM was then added to each well, and cells were incubated for 14 days to allow colony formation. After 14 days of incubation, when the colony count reached >50 colonies, the media were discarded, and the colonies were washed twice with 1 mL of ice-cold PBS. The colonies were then fixed in 100% MeOH for 10 minutes. The colonies were stained with 0.5 ml 0.05% methylene blue in 1:1 distilled water/MeOH for 10 minutes. The colonies were washed afterwards with water to remove excess methylene blue stain, air dried for 1 hour, and the total colonies counted.

2.7.4. 3D model spheroid of PANC-1

Suitable 3D models of PANC-1 were attained in 3D ULA 96 well plates. PANC-1 cells were seeded in different seeded numbers: 500 cells/well, 1000 cells/well, 1500 cells/well, 2000 cells/well, 2500 cells/well, and 3000 cells/well. Upon seeding, the cells were inserted into the 3D low attachment 96 well plates and centrifuged at 500 G for 5 minutes. This allowed the cells gather in the middle of the wells. The cells were then incubated for 24-72 hours being periodically observed to investigate their ability to aggregate and form spheroidal cell aggregates. The picture was obtained using a CKX53 inverted microscope equipped with an SC180 digital camera and cellSens Standard software (Olympus, Japan). Images were captured at 10× magnification. The diameter of the cells were then measured by ImageJ. Volume was measured with Equation 2.5.

$$\boldsymbol{Volume\ of\ Spheroid} = (\frac{4}{3})\boldsymbol{\pi r^3} \quad (2.5)$$

2.7.5. Examination of 2.1a growth effects in 3D spheroid PANC-1

The PANC-1 cells were seeded at 2500 cells per well and were incubated for 48 hours in 37 °C/5%/CO_2 to allow cells to aggregate and form spheroids. Cisplatin was used as the positive control. Both cisplatin and the titanium complex (**2.1a**) stock solution were made at 1.00 mM in DMSO. Serial dilutions of cisplatin and the titanium complex (**2.1a**) were performed in the cDMEM to achieve several concentrations: 0 μM, 1 μM, 3 μM, 5 μM, and 10 μM. The final concentration of DMSO was ≤0.1% v/v, appropriate for reproducible cell culture. After 48 hours, the cells were treated with the respective concentration of cisplatin or titanium complex (**2.1a**) and were incubated for 72 hours in 37 °C/5%/CO_2. Refer to Section 2.7.4, cells were observed, and diameter and volume of the spheroid were measured using Equation 2.5.

2.7.6. Examination of 2.1b growth effects in 3D spheroid MCF-7 and MRC-5

Both MCF-7 and MRC-5 cells were seeded at 2500 cells per well and were incubated for 48 hours in 37 °C/5%/CO_2 to allow cells to aggregate and form spheroid. Cisplatin was used as the positive control. Both cisplatin and the titanium complex (**2.1b**) stock solution were made at 1.00 mM in DMSO. Serial dilutions of cisplatin and the titanium complex (**2.1b**) were performed in the cDMEM to achieve several concentrations: 0 μM, 1 μM, 3 μM, 5 μM, and 10 μM. The final concentration of DMSO was ≤0.1% v/v, appropriate for reproducible cell culture. After 48 hours, the cells were treated with the respective concentration of cisplatin or titanium complex (**2.1b**) and were incubated for 72 hours in 37 °C/5%/CO_2. Refer to Section 2.7.4 and 2.7.5, cells were observed, and diameter and volume of the spheroid were measured using Equation 2.5.

2.7.7. Analysis of transferrin receptor 1 (Trf-1) level

Analysis of transferrin receptor 1 (TrF-1) Level was carried out using a flow cytometry method. PANC-1 cell lines (0.5 to 1.0 × 10^6) were harvested and resuspended in PBS, which was spun down at 800-1000 RPM for 5 minutes at room temperature. The resulting cell pellet was washed in ice cold PBS, followed by re-centrifugation at 800-10000 RPM for 5 minutes. This washing process was repeated three times. After the final was removed the pellet was resuspended in 4% aqueous paraformaldehyde. The resulting solution was then placed in a shaker incubator at room temperature for 15 minutes. The resultant solution was spun down and again resuspended with PBS. This final sample was stored in 4 ^oC until analysed. For analysis, the sample was split into two: unstained cells and cells stained with the appropriate primary antibody. Unstained cells was not treated with antibody. Stained cells sample was spin down and resuspended in 1% BSA in PBS-T (0.05% Tween) containing the antibody conjugated with PE, CD71 (Transferrin Receptor) Monoclonal Antibody (OKT9 (OKT-9)), PE, eBioscience™. Both samples were spun down and the pellets obtained washed three times in phosphate buffer saline (PBS). The cells then were analysed using flow cytometry.

2.7.8. Attempted titanium complex encapsulation using a pH re-assembly method

The encapsulation of titanium complex was initially done using re-assembled method. The encapsulation was done using HSAFt. The pure HSAFt was obtained from Reyhan Colpan in frozen conditions. The HSAFt was defrosted and diluted to 2.5 mg/mL. Sodium chloride buffer pH 2 was used to disassemble the HSAFt into subunits and the required buffer prepared by adding several drops of 1 M HCl to sodium chloride buffer until it was pH 2. The HSAFt sample (2.5 mg/mL) was prepared in a dialysis bag, which was put into a stirred sodium chloride buffer pH 2 at 4 °C for 30 minutes. Subsequently the HSAFt dialysis bag was moved to a stirred sodium

buffer solution at 4 °C for 1 h before this process was repeated using a sodium acetate buffer solution at pH 7.4. Titanium complex (**2.1a**) was diluted in DMSO and added to the hydrolysed apoferritin in a ratio of mol/mol 1:150 (apoferritin: compound) and stirred at 4 °C overnight (16 h). After that the HSAFt-Ti complex was moved into sodium acetate buffer at 25 mM pH 7.4 and incubated at 4 °C overnight. After overnight incubation, the dialysis process was carried out to further remove the aggregated protein and unencapsulated compound. This process is done by filtering the HSAFt-Ti complex with starlab sterile syringe filter PES membrane with diameter of 33 mm and pore size of 0.22 μm. The pure HSAFt-Ti complex is then stored at 4 °C.

2.7.9. Analysis of AFt reassembly and disassembly by native PAGE

The analysis of the disassembly of the AFt after encapsulation was carried out using Native PAGE. A Bio Rad® Mini-Protean 3 gel system was used for the protein gel electrophoresis. Composition of the gel layers can be found in Table 2.7.

Table 2.7. Native PAGE solution composition. The gel's solutions were made fresh before experiment and TEMED was added last to initiate the formation of the gel. Stacking gel was made 5 mL and the resolving gel was made 10 mL. The plates were incubated at 50 ^{o}C while the polymerisation reaction was taking place to speed up the formation of the gel.

Component	6% (w/v) Resolving gel (μL)	4% (w/v) Stacking gel (μL)
Milli Q Water	6660	2880
30% (w/v) Bis-acrylamide	2300	500
1.5M Tris pH 8.8	3000	-

1 M Tris pH 6.8	-	940
10% (w/v) Ammonium persulphate (APS)	150	60
TEMED	15	6

After the addition of TEMED, 6% resolving gel was added into the gel plates following the addition of 100% isopropanol on the top layer of the resolving gel. After the resolving gel had polymerised, the isopropanol layer was removed and 4% stacking gel was added on the top of the resolving gel with a 1 mm Teflon, 10 lane comb. Once the native PAGE gel was set, it was wrapped with Milli Q water and stored at 4 ^{o}C. Then, the gel was loaded into the tank with 1x native PAGE running buffer. Native protein sample was prepared by mixing Aft-encapsulation samples (12 μL) and native loading buffer (4 μL). After that, 10 μL of native protein samples were loaded into the well of the gel. NativeMark® (Invitrogen™, USA) protein ladder was used as a guideline for the protein size. Electophoresis ran at 100 V for 150 minutes. The gel was stained with GelCode blue stain reagent (Thermo Fisher, USA) for 90 seconds. The stain was removed with heat for 60 seconds and washed three times. Then, the gel was left overnight to de-stain in water. The gel was observed using Bio Rad® gel imaging system.

2.7.10. Detection of the level of 2.1a inside of AFt cage

The level of **2.1a** inside of the AFt cage were examined using inductively coupled plasma mass spectrometry (ICP-MS) with a PerkinElmer NexION 2000 instrument. Analyses were conducted at the School of Chemistry, University of Nottingham, under the guidance of Riley Hristoff. Samples were prepared according to standard protocols, including digestion in nitric acid and dilution of TiO_2 (Standard calibration at 10 ppm, 1 ppm, 100 ppb, 10 ppb, 1 ppb) prior to

analysis. Instrument calibration was performed using multi-element calibration standards, and internal standards were applied to correct for instrumental drift and matrix effects. Instrument tuning, data acquisition, and quality control were performed in accordance with the facility's standard operating procedures. The resulting data were processed by the author.

3. CHAPTER THREE: AN INVESTIGATION OF THE ANTI-CANCER PROPERTIES OF AMIDE DERIVATIVES

3.1. Research aims

While the titanium agents in Chapter 2 are clearly effective at inhibiting the growth of cancer *in vitro*, there is a need for a broader range of therapeutic strategies for cancer treatment. Therefore, the work presented in Chapter 3 is not directly related to the previous study and cannot be directly compared with Chapter 2 due to differences in the nature and mechanism of action of the compounds studied. Moreover, metal-based therapy is not the only category of agents with potential anticancer activity that warrants investigation. Despite the difference between these compounds, each are needed to undergo preliminary *in vitro* evaluation as previous literature has indicated their potential effects on cancer cells.

2-Aryl thiazol-5-amines or 2-ATA are a class of compounds in which a thiazole ring system bears a 2-aryl substituent and an amine group is also attached to C(5) of the thiazole ring (Figure 3.1).[159] Such compounds have been studied and become of interest in medicinal chemistry due to their anti-inflammatory and anti-cancer properties.[159] This is thought to be due to their ability to act as kinase inhibitors and tubulin polymerisation inhibitors, resulting in subsequently triggered apoptosis in cancer cell lines.[159]

The 2-ATA compound class has an ability to inhibit several kinases important for cancer cells. These include: the aurora A and B kinases (essential for chromosome segregation and cell division), the Src kinase (that has a function in cell growth and migration), the Abl kinase (involved in growth and differentiation) and finally the EGFR kinase (that is involved in cell proliferation and survival).[160] These abilities have been shown in A549 lung and MCF-7 breast

cancer cell line studies attempting to target EGFR and HER2 kinases.[161] The 2-ATA class of compounds also have reported to have the ability to inhibit the formation of microtubules, structures that are essential to successful mitosis, disruption of which leads to G2/M arrest and subsequent apoptosis.[159,162] Certain 2-ATA molecules are able to interfere with the colchicine binding site on tubulin, triggering G2/M cell cycle arrest.[159,162] Furthermore, like many anti-cancer compounds, the 2-ATA class has an ability to target proteins crucial for triggering the onset of apoptosis, such as Bcl family protein and Bax family protein, all leading eventually to programmed cell death.[163]

In contrast, 4-aminoantripyrine (4-AAP) belongs to structurally distinct class of pyrazolone compound.[164] The first 4-AAP synthesised was 4-aminoantipyrine (4-aminophenazone) prepared by Friederich Stolz and Ludwig Knorr in the late nineteenth century.[164] It is an aromatic heterocyclic compound with two nitrogen atoms that is joined with a reactive amine and a carbonyl functional group (Figure 3.1).[164] It demonstrates several activities in biological systems including: anti-inflammatory, anti-pyretic, and analgesic properties.[165] The 4-AAP compound itself is a metabolite of aminopyrine and metamizole, a known analgesic medication. The species 4-*N*-methylaminoantipyrine (4-MAA), a product of the nonenzymatic breakdown of metamizole, is demethylated to 4-AAP.[166] It can form a stable complex with a heme, iron-containing porphyrin ring structure.[167] However, it is rarely used as an analgesic due to the risk that agranulocytosis or low neurophile count in blood cells is created by the 4-AAP therapy. [167] In addition to their function as anti-inflammatory and anti-pyretic, amide derivatives 4-AAP are also being studied for their anti-cancer properties. These compounds show a promising inhibitory effect in cancer cell proliferation assays, specifically breast cancer, renal cancer, and leukemia.[168] Furthermore, 4-AAP can bind to DNA in the cancerous cells and

disrupt the transcription of essential genes for growth, leading to programmed cell death or apoptosis (refer to Figure 1.2). In another study, 4-AAP shows selective cytotoxicity activity in TNBC breast cancer cell lines, making it a promising experimental chemotherapy agent.[169]

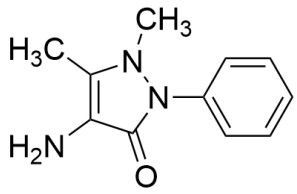

Figure 3.1. General Structure of 4-AAP.

Although 2-ATA and 4-AAP have different chemical structures, they share some function similarities as anti-cancer agents. The research in Chapter 3 aims to determine and evaluate the novel anticancer effects of amide derivatives of 4-AAP (**3.1**-**3.72**, Scheme 3.1) using MTT assays. Moreover, metal-based therapy is not the only agent category with potential anticancer activity that warrants investigation. The inclusion of this chapter therefore broadens the scope of the thesis by assessing structurally distinct yet functionally relevant candidates, contributing to the overall objective of identifying potential anticancer leads.

3.2. Testing of novel succinic derivatives of 4-AAP and 2-ATA

A library of succinic acid/succinimide derivatives of 4-amino-1,5-dimethyl-2-phenyl-1,2-dihydro-*3H*-pyrazol-3-one (4-AAP) (Scheme 3.1) or 2-arylthiazol-5-amine (2-ATA) (Scheme 3.2) are available to us through a collaboration.[170] Several structurally related compounds exist in sufficient amounts for biological studies and the sub-set **3.1-3.7**, **3.49**, **3.53**, **3.56**, **3.58**, **3.66**, **3.88**, **3.95** and **3.97** were selected for study due to its structural diversity.

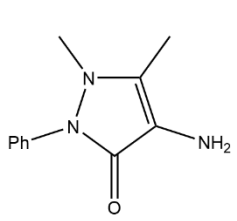

4-AAP

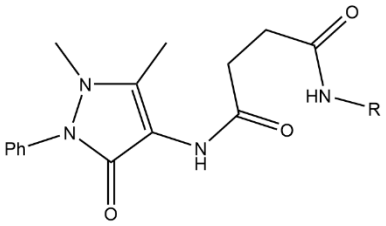

R:

3.1. Ph
3.2. 4-MeC_6H_4
3.3. 3-MeC_6H_4
3.4. 2-MeC_6H_4
3.5. 4-EtC_6H_4
3.6. 4-*i*PrC_6H_4
3.7. 3-*i*PrC_6H_4
3.8. 4-*n*BuC_6H_4
3.9. 3,6-$Me_2C_6H_3$
3.10. 3,5-$Me_2C_6H_3$
3.11. 3-FC_6H_4
3.12. 4-FC_6H_4
3.13. 3,4-$F_2C_6H_3$
3.14. 3,5-$F_2C_6H_3$
3.15. 3-$CF_3C_6H_4$
3.16. 4-$CF_3C_6H_4$
3.17. 4-ClC_6H_4
3.18. 3-ClC_6H_4
3.19. 3,5-$Cl_2C_6H_3$
3.20. 2,5-$Cl_2C_6H_3$
3.21. 3-BrC_6H_4
3.22. 4-BrC_6H_4
3.23. 2-Me-4-BrC_6H_3
3.24. 3-Br-4-MeC_6H_3
3.25. 4-IC_6H_4
3.26. 3-IC_6H_4
3.27. 2-$MeOC_6H_4$
3.28. 3-$MeOC_6H_4$
3.29. 4-$MeOC_6H_4$
3.30. 3,4-$(MeO)C_6H_3$
3.31. 3,5-$(MeO)C_6H_3$
3.32. 3-$(CF_3O)C_6H_4$
3.33. 4-$(CF_3O)C_6H_4$
3.34. 3-Br-4-$(MeO)C_6H_3$
3.35. 3-(MeO)-4-BrC_6H_3
3.36. 4-$(NO_2)C_6H_4$
3.37. 3-$(NO_2)C_6H_4$
3.38. 7-(2,3-dihydrobenzofuranyl)
3.39. 2-$(PhCH_2O)C_6H_4$
3.40. 3-$(MeO_2C)C_6H_4$
3.41. 4-$(MeO_2C)C_6H_4$
3.42. 4-$(PhN{=}N)C_6H_4$
3.43. 2-thiazole
3.44. $CHMe(c\text{-}C_6H_{11})$
3.45. CH_2CHPh_2
3.46. (*S*)-CHMe-4-$MeOC_6H_4$
3.47. (*R*)-CHMe-4-$MeOC_6H_4$
3.48. CHMe-2-naphthyl
3.49. CH(Ph)-4-ClC_6H_4
3.50. $CHPh_2$
3.51. CH_2Ph
3.52. $CO(CH)_2CONH(9H\text{-fluoren-9-yl})$
3.53. $(CH_2)_2(2\text{-}ClC_6H_4)$
3.54. CH_2COPh
3.55. $CHMe(4\text{-}MeC_6H_4)$
3.56. $CH_2(4\text{-}FC_6H_4)$
3.57. $(CH_2)_2(2,4\text{-}(MeO)_2C_6H_3)$
3.58. $CH_2(2\text{-}ClC_6H_4)$
3.59. CHMePh
3.60. CH_2(1-naphthyl)
3.61. $(CH_2)(2,4\text{-}(MeO)_2C_6H_3)$
3.62. $CHBnCO_2Bn$
3.63. CH_2CHPh
3.64. 1-adamantyl
3.65. 1-(2-phenylcyclopropyl)
3.66. $CHMe(4\text{-}ClC_6H_4F)$
3.67. $CH_2CH_2CH(OEt)_2$
3.68. *n*-C_6H_{13}
3.69. CH_2-2-(5-methylfuranyl)
3.70. 4-(1-(ethoxycarbonyl)piperidinyl)
3.71. CHMe(1-adamantyl)
3.72. $CH(CO_2Me)(CH_2\text{-}3\text{-idenyl})$
3.73. CHEtPh
3.74. $CHMe(3\text{-}MeOC_6H_4)$
3.75. 2-pinenyl
3.76. 1-(c-C_6H_{10}(2-OBn))
3.77. 2-benzimdazyl
3.78. 1-(c-C_6H_{10}(1CCH))
3.79. 3-(6-MeO-pyridyl)
3.80. 4-(1-(*t*BuO_2C)piperidinyl)
3.81. CHMe(1-naphthyl)
3.82. *n*-$C_{12}H_{25}$
3.83. 2-$(OH)C_6H_4$
3.84. 4-dibenzo[18crown6]-yl
3.85. $CH(CO_2Et)$-3-indenyl
3.86. CH_2CO_2Bn
3.87. $CH_2CH_2CH_2Ph$
3.88. $CH_2(4\text{-}Bpin)C_6H_4$
3.89. $CH(CO_2Me)CH_2Ph$

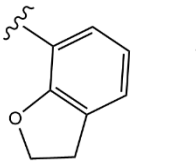

7-(2,3-diydrobenzofuranyl)

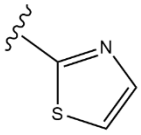

2-thiazole

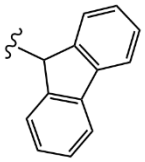

9*H*-fluoren-9-yl

1-adamantyl

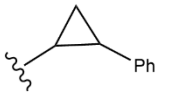

1-(2-phenylcyclopropyl)

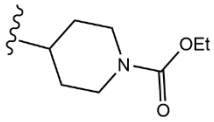

4-(1-(ethoxycarbonyl)piperidinyl)

Scheme 3.1. Library of 4-amino-1,5-dimethyl-2-phenyl-1,2-dihydro-*3H*-pyrazol-3-one (4-AAP) derivatives (**3.1-3.89**) available to us. The *in vitro* activity of the exemplars in red against HCT-116 and MCF-7 is reported herein. Examples (**3.90-3.91**, not shown) are 4-AAP analogues of 2-ATA compounds **3.92**, **3.93** in Scheme 3.2.

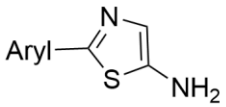

2-ATA

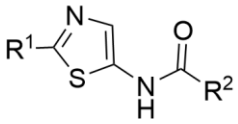

	R^1	R^2
3.92.	Ph	$CH_2CH_2CO_2H$
3.93.	Ph	(*E*)-$CH{=}CHCO_2H$
3.94.	4-MeC_6H_5	(*E*)-$CH{=}CHCO_2H$
3.95.	4-MeC_6H_5	$CH_2CH_2CO_2H$
3.96.	4-BrC_6H_5	$CH_2CH_2CO_2H$
3.97.	4-BrC_6H_5	(*E*)-$CH{=}CHCO_2H$

Scheme 3.2. Library of 2-arylthiazol-5-amine (2-ATA) derivatives (**3.92-3.97**) available to us. The *in vitro* activity of the exemplars in red against HCT-116 and MCF-7 is studied herein.

3.3. First preliminary screening of amide derivatives of 4-AAP and 2-ATA

Because of the large number of compounds available in the libraries of Schemes 3.1-3.2 preliminary screening is appropriate to determine the inactive and the active compounds for further anti-cancer investigations within this study. We chose to use 10 nm and 100 μM concentrations of the tested agents against HCT-116 and MCF-7, using cisplatin as a positive control (Figure 3.2).

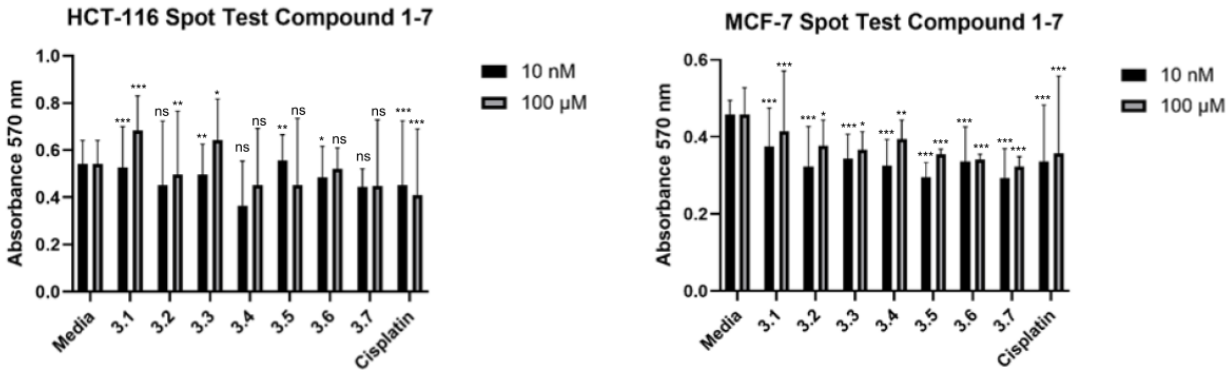

Figure 3.2. Preliminary screen of novel amide derivatives of 4-AAP against HCT –116 (left) and MCF-7 (right). Data shown as mean ±SD. n = 3. Statistical analysis was done using one-way ANOVA, comparing each treatment with control (media). * P < 0.05, ** P < 0.01, *** P <0.001, **** P < 0.0001; ns = not significant.

According to the data above, the preliminary results show that **3.1-3.7** possess inhibitory activity against the MCF cell line. However, **3.1-3.6** all show a relatively small number of hits for potent inhibitory activity, with slightly enhanced activity against the MCF-7 cell line compared to HCT-116 cells. For example, **3.1.** at 10 nM in MCF-7 has 5% of inhibition and at 100 µM has reduced absorbance to 0.38 as compared to media (0.44), resulting in 14% of inhibition. On the other hand, at 100 µM in HCT-116 has 9% of inhibition. Figure 3.2 also shown that after **3.6** at 10 nM , MCF-7 has 10% of inhibition and at 100 µM has reduced absorbance to 0.31 as compared to media (0.44), resulting in 30% of inhibition, while in HCT-116 it shows 16% of inhibition. Furthermore, **3.7** at 100 µM concentration exhibit 25% of inhibition in MCF-7 and 16% of inhibition in HCT-116. Thus, based on this observation, the lower growth inhibition and cytotoxicity marker seen in this selection is **3.1**, while **3.6** and **3.7** are chosen for their potentially (marginally) higher activity.

A second preliminary screening study was conducted to further examine potential cytotoxicity within the compound libraries (Figure 3.3). Compounds from both Scheme 3.2 and 3.3 were

chosen due to have maximal structural diversity compared to the family of compounds in Figure 3.2. We applied this strategy due to the uniform poor activities seen for the similar derivatives **3.1-3.7**. As seen in Figure 3.3, despite increasing the structural diversity of the compounds screened, all compounds only induce the growth of both cancer cell lines. Because these did not exhibit any inhibitory ability, we chose to focus further studies just on **3.1** and **3.6-3.7**.

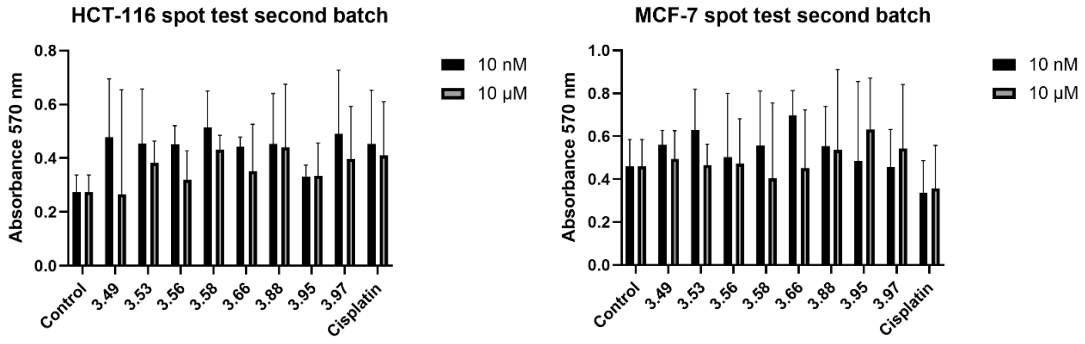

Figure 3.3. Second Preliminary Study of Novel Amide Derivatives of 4-AAP and and 2-ATA against HCT –116 (left) and MCF-7 (right).

3.4. Cell viability assay to determine the growth inhibition of amide derivatives of 4-AAP and 2-ATA

The preliminary screenings of **3.1**-**3.7** (refer to Section 3.3) shows that there are three compounds were chosen for further investigation. Compound **3.1** was selected as a comparator, as in the spot test this compound is judged to have the lowest activity in inhibiting the growth of MCF-7 and HCT-116 cells. This is to be compared against the apparently higher activity of **3.6-3.7**. To reinforce the conclusions of the spot tests dose-activity relationships of **3.1** and **3.6-3.7** are compared against cisplatin in Figure 3.4.

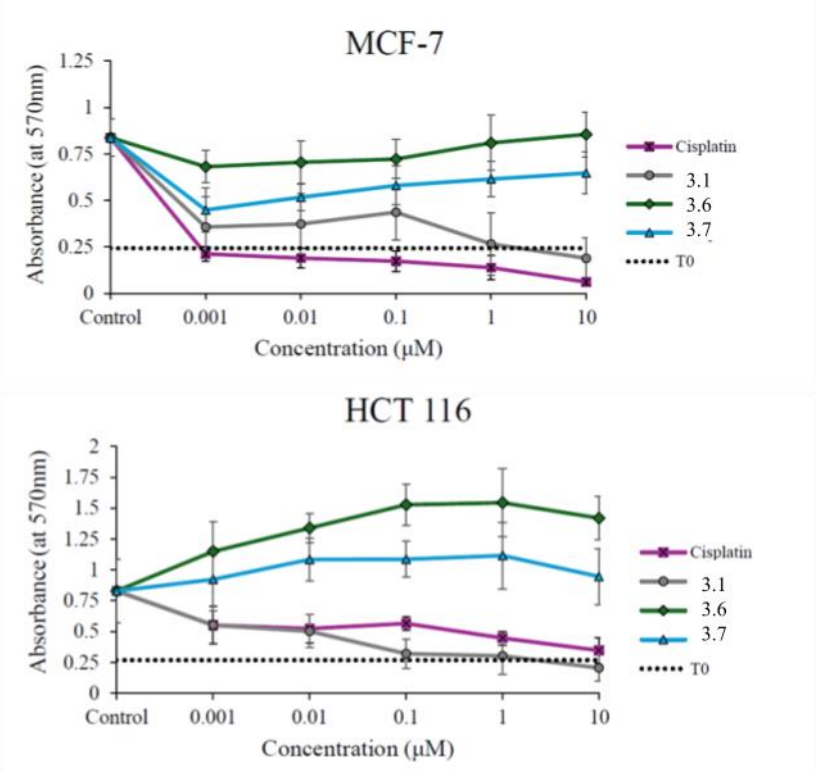

Figure 3.4. MTT cell viability assay of novel amide derivatives of 4-AAP selected from preliminary study (**3.1, 3.6**, and **3.7**) against MCF-7 (up) and HCT-116 (down). Cisplatin is being used as the positive control.[171] Data points are presented as mean absorbance values ± SD (n=4 for cisplatin, n=5 for **3.1, 3.6**, and **3.7**).

Based on Figure 3.4, cisplatin shows high dose-dependent reduction in cell viability. This can be seen by fast dropping of absorbance values below the value of T_0 (0.25) at concentrations ≥0.01 μM in MCF-7 and slow decrease with 40% viability persisting at 10 μM in HCT-116. These then confirmed its well-documented cytotoxicity and growth inhibitory effect towards cancerous cells[172,173], thus becoming the benchmark comparison (positive control) in this study.

Furthermore, **3.1** showed less growth inhibitory effect as compared to cisplatin in MCF-7, with partial reduction in cell viability at high concentration (10 μM). However, in contrast with that,

3.1 showed higher growth inhibition in HCT-116. This is due to the present of phenol in the structure of **3.1**, enabling redox-mediated induction of apoptosis of the cancerous cells by increasing accumulation of ROS inside of the cells.[174] This compound also more potent in HCT-116 because apparently phenol group has a selective reactivity towards colon cancer, because colon cancer is more susceptible to ROS-mediated cell death as compared to breast cancer.[175]

On the other hand, **3.6** and **3.7** are not able to inhibit the growth of both MCF-7 and HCT-116 cells. In contrast, both compounds slightly increase the viability of the cells. The presence of isopropyl group in the compound can increase the lipophilicity and steric bulk, which can disrupt the interaction of the compound to the cancer cells, lead to loss of activity of the compound.[176]

3.5. Dose response parameter : GI_{50} values

GI_{50} values are commonly used to determine the growth inhibitory and cytotoxicity effects of compounds and cisplatin, which commonly used as a positive control. The value of GI_{50} indicates the concentration (most often in μM) that inhibits cell growth by 50%. For low activity species, such as those in this study the use of GI_{50} is more appropriate as, clearly, compounds that promote growth cannot generate LD_{50} results (at least under the concentrations of our own study). The values of GI_{50} for the four compounds screened are compared to each other and literature values in Table 3.1 below.

Table 3.1. GI_{50} values of **3.1**, **3.6**, **3.7**, and cisplatin in HCT-116 and MCF-7 cell lines. Values are reported in nM and as mean ± SEM, n=3.

Compound	HCT-116 GI_{50} value	MCF-7 GI_{50} value
Cisplatin (literature values)[85]	8.2±0.4	7.6 ± 0.2
Cisplatin (Figure 3.4)	1.27±0.33	0.694±0.11
3.1	1.73±0.57	0.752±0.07
3.6	Not an inhibitor	Not an inhibitor
3.7	Not an inhibitor	Not an inhibitor

Based on Table 3.1, the growth inhibitory of cisplatin towards both cell lines is expected on both cell lines, with activity 2 folds more active in MCF-7 cell lines as compared with HCT-116. Interestingly **3.1** shows strong growth inhibition rate as compared with **3.6** and **3.7**, with GI_{50} value of 1.73±0.569 nM in HCT-116 and 0.752±0.067 nM in MCF-7. This also shows that **3.1** is more potent in MCF-7 as compared to HCT-116. On the other hand, **3.6** and **3.7** does not showing growth inhibition towards both MCF-7 and HCT-116. Thus, the GI_{50} of both compounds cannot defy and further research needs to be done to determine the biological function of these compounds, either as growth inhibitor agents of cancer or growth promoting agents.

The activity of our cisplatin shows differences with the GI_{50} values reported from the literature (Table 3.1). Although the experiment adopted the same cell lines, culture conditions, and exposure time, variations in cisplatin GI_{50} values may arise from the different passage number cells, drug stability, serum lot composition, and biological variability of MCF-7 and HCT-116 cells. Cisplatin is known to have a high sensitivity towards experimental variables that are often

underreported, including drug preparation, storage conditions, and chloride concentration, which contributes to its aqueous state and biological activity. Cisplatin is sensitive to chloride concentrations particularly. Under low-chloride conditions, the chloride ligands are replaced with water molecules, generate highly reactive platinum and induce DNA crosslink. [66] A little difference in serum composition can also alter the effectiveness of cisplatin due to its rapid protein binding, affecting the intracellular drug concentration.[177] Cisplatin binds strongly to serum protein (i.e. human serum albumin) which can reduce its free and active concentration. [177] The other factors are the biological variability of cancer cell lines used, such as cell-cycle distribution, passage number, and growth kinetics during the treatment period can influence cisplatin sensitivity.[179,180] A study has been found that late passage cell lines with faster growth rates showed an increased in cisplatin sensitivity as compared with the parental cell lines.[178] Furthermore, the MTT assay measures metabolic activity and is known to suppress mitochondrial function prior to loss of viability, which may result in lower apparent GI_{50} values.

Overall, the investigation of the library of compounds in Scheme 3.2 and 3.3 is disappointing. The investigations conducted seem to indicate that the addition of the amide function to the 4-AAP and 2-ATA cores have resulted in much less active anti-cancer agents than the parent cores. It is not clear why this is the case. Further studies need to examine the cellular and molecular mechanisms of the amide 4-AAP 2-ATA derived compounds, as at present it is not easy to see why **3.1** is the only active compound while **3.6** and **3.7** are inactive. At first sight the medicinal chemistry parameters of the four compounds are similar (Scheme 3.4).

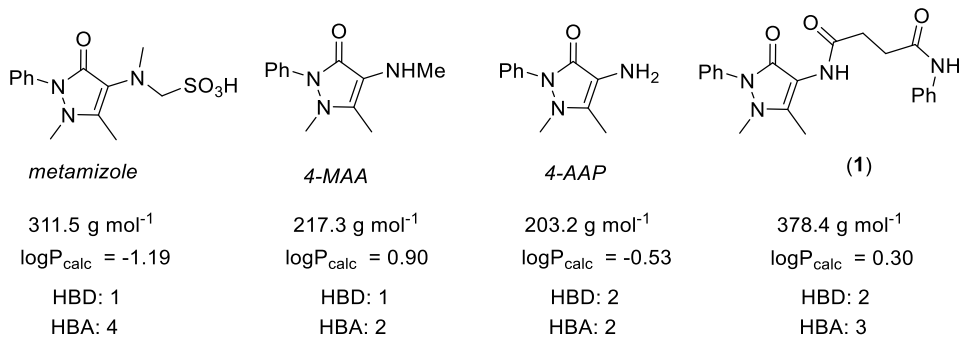

Scheme 3.4. Selected calculated medicinal chemistry parameters for metamizole and its biological degradation products vs. **3.1**. HBD = hydrogen bond donors, HBA = hydrogen bond acceptors.

3.6. Conclusion

The first preliminary screening of 4-AAP compound **3.1**-**3.7** against MCF-7 ad HCT-116 using MTT assay revealed the growth-inhibitory mechanism as the response of therapy. According to the preliminary screening in this experiment, the compound has a lipophilic substituent, which increases membrane permeability and absorption, made the growth-inhibitory effects more potent towards MCF-7 cell line. Furthermore, these inhibited cell viability in the HCT-116 cell line in a statistically insignificant way, making their interpretation uncertain. Compounds **3.1, 3.6, 3.7** were subsequently examined using the same experiment in light of these findings, yielding a dose-response relationship. These findings did defy the first screening, possibly as a result of 4-AAP' limited water solubility. On the other hand, second preliminary study shows that it has low activity towards both cell lines. The investigations indicate that the addition of the amide function to the 4-AAP and 2-ATA cores result in reduced activity compared to the parent cores. Thus, there is a need to determine the cellular and molecular mechanism of amide 4-AAP and 2-ATA derived compounds.

3.7. Future work

Future work needs to focus on the rational optimisation of amide-linked 4-AAP and 2-ATA derivatives through systematic modification of the amide-bound substituents. Optimisation of the aromatic substituents and amide linker within 4-AAP scaffold have a possibility to enhance the biological activity (i.e. targeting the metabolism) and selectivity, further improving the drug properties. *In silico* approaches (i.e. molecular docking and ADMET prediction) should be done before conducting biological assay of the drugs, to guide the design of improved derivatives of the drugs.

3.8. Biology experimental

3.8.1. Cell culture and maintenance of MCF-7 and HCT-116

Human MCF-7 and HCT-116 cell line (ATCC, USA) were maintained as batches of 0.3 to 1 × 10^6 cells in complete Dulbecco's Modified Eagle Medium (DMEM) of a supplemented version there of (cDMEM). The cDMEM medium was prepared from Dulbecco's Modified Eagle Medium (DMEM from Thermo Fisher, USA) by addition of 10% Fetal Bovine Serum (Thermo Fisher, USA). The PANC-1 cells were maintained in a T75 flask, typically at3 × 10^5 cells/mL, inside a 37°C/-5%/CO_2 incubator. After four days these cells had typically reached approximately 80% confluence. At this point the cells were washed with sterile phosphate buffer saline or PBS (Thermo Fisher, USA) and was introduced with trypsin (Thermo Fisher, USA) for detaching the cells. After 5 minutes, fresh cDMEM was inserted to stop the trypsin activity and the cells were centrifuged in 400G for 5 minutes. After that the cells were counted and the number of cells mentioned above were growth in the flask for maintenance.

3.8.2. Preparation of stock solutions for treatment media of novel amide derivatives of 4-AAP

The novel amide derivatives of 4-AAP used in this study were obtained as part of a collaboration with Mr Adil Afaq of Mirpur University of Science and Technology (MUST), Department of Chemistry, Pakistan. The amide derivatives of 4-AAP used (Schemes 3.1 and 3.2) were selected based on representative structure differences. Several compounds were chosen for this study: **3.1-3.7, 3.49, 3.53, 3.56, 3.58, 3.66, 3.88, 3.95**, and **3.97** (Scheme 3.1 and 3.2). Cisplatin was used as a positive control for this study. Cisplatin and all the selected amide derivatives tested were prepared as 1 mM of stock solutions in dimethyl sulfoxide (Thermo Fisher, USA, 100 µL).

3.8.3. First preliminary screening of amide derivatives of 4-AAP

Initially, spot test MTT (3-(4,5-dimethylthiazol-2-yl)-2,5-diphenyltetrazolium bromide) assays were conducted to explore the typical growth inhibition limits of the derivatives of 4-AAP (Scheme 3.1) and 2-AAT (Scheme 3.2). HCT-116 and MCF-7 cells were seeded at 3×10^3 and 4×10^3 cells per well respectively and were incubated for 24 hours in 37 °C/5%/CO_2 to allow cells to adhere to the well. Separately, serial dilutions of cisplatin and the amide compounds were performed using cDMEM to achieve two spot test concentrations, 10 nM and 100 µM. The final concentration of DMSO was ≤0.1% v/v, which was at a level not affecting cell culture. The cells then were treated with cisplatin and tested amides at the two selected concentrations, and the treated cells incubated for 72 hours in 37 °C/5%/CO_2. After 72 hours, the MTT assay was conducted under the same procedure as refer to Section 2.7.2.

3.8.4. Cell viability assay to determine the growth inhibition of Novel Amide Derivatives of 4-AAP

Selected compounds were further investigated to provide their dose response curves by MTT assay. HCT-116 and MCF-7 cells were seeded at 3×10^3 and 4×10^3 cells per well respectively and were incubated for 24 hours in 37 °C/5%/CO_2 to allow cells to adhere properly to the well. In each case, after 24 hours, a T_0 absorbance reading was obtained by adding MTT reagent in the desired wells as a baseline measurement. Serial dilutions of cisplatin and the amide derivatives (Scheme 3.1-3.2) were performed in the cDMEM to achieve the concentrations: 1 nM, 10 nM, 100 nM, 1 µM, and 10 µM. The final concentration of DMSO in each of these solutions was ≤0.1% v/v, which was at a level where cell culture was unaffected by its presence. The grown cells then were treated with the concentrations of cisplatin and amide agent mentioned above and were then incubated for 72 hours in 37 °C/5%/CO_2. After 72 hours, the MTT was conducted under the same procedure as Section 2.7.2.

3.8.5. Second preliminary screening of novel amide derivatives of 4-AAP

Second spot test MTT (3-(4,5-dimethylthiazol-2-yl)-2,5-diphenyltetrazolium bromide) assays were conducted to explore the typical growth inhibition and cytotoxicity of novel Schiff-base derivatives of 4-AAP (Scheme 3.1.). The technique used was adapted from the procedure by Mosmann (1983). HCT-116 and MCF-7 cells were seeded at 3×10^3 and 4×10^3 cells per well respectively and were incubated for 24 hours in 37 °C 5% CO_2 to allow cells to adhere to the well. Separately, serial dilutions of cisplatin and the Schiff-base species were performed using cDMEM to achieve two spot test concentrations, 10 nM and 10 µM. The final concentration of DMSO was ≤0.1% v/v, which was at a level not affecting cell culture. The cells then were treated with cisplatin and Schiff-base compounds at the two spot test concentrations used and the

treated cells incubated for 72 hours in 37 °C/5%/CO_2. After 72 hours, the MTT assay was conducted under the same procedure as refer to Section 2.7.2.

4. REFERENCES

1 J. Ferlay, M. Colombet, I. Soerjomataram, D. M. Parkin, M. Piñeros, A. Znaor and F. Bray, *Int. J. Cancer*, 2021, **149**, 778–789.

2 D. Hanahan and R. A. Weinberg, *Cell*, 2000, **100**, 57–70.

3 D. Hanahan, *Cancer Discov.*, 2022, **12**, 31–46.

4 D. Hanahan and R. A. Weinberg, *Cell*, 2011, **144**, 646–674.

5 N. A. Bhowmick, E. G. Neilson and H. L. Moses, *Nature*, 2004, **432**, 332–337.

6 N. Cheng, A. Chytil, Y. Shyr, A. Joly and H. L. Moses, *Mol. Cancer Res.*, 2008, **6**, 1521–1533.

7 X. Li, X. Huang, M. Chang, R. Lin, J. Zhang and Y. Lu, *Visualized Cancer Medicine*, 2024, **5**, 6.

8 T. L. Yuan and L. C. Cantley, *Oncogene*, 2008, **27**, 5497–5510.

9 B. H. Jiang and L. Z. Liu, *Adv. Cancer Res.*, 2009, **102**, 19–65.

10 D. L. Burkhart and J. Sage, *Nat. Rev. Cancer*, 2008, **8**, 671–682.

11 M. M. Lipinski and T. Jacks, *Oncogene*, 1999, **18**, 7873–7882.

12 N. Mizushima, *Genes Dev.*, 2007, **21**, 2861–2873.

13 B. Levine and G. Kroemer, *Cell*, 2008, **132**, 27–42.

14 J. F. Passos, G. Saretzki and T. Von Zglinicki, *Nucleic Acids Res.*, 2007, **35**, 7505–7513.

15 J. Il Park, A. S. Venteicher, J. Y. Hong, J. Choi, S. Jun, M. Shkreli, W. Chang, Z. Meng, P. Cheung, H. Ji, M. Mclaughlin, T. D. Veenstra, R. Nusse, P. D. Mccrea and S. E. Artandi, *Nature*, 2009, **460**, 66–72.

16 G. Berx and F. van Roy, *Cold Spring Harb. Perspect. Biol.*, DOI:10.1101/CSHPERSPECT.A003129.

17 S. Negrini, V. G. Gorgoulis and T. D. Halazonetis, *Nat. Rev. Mol. Cell Biol.*, 2010, **11**, 220–228.

18 J. J. Salk, E. J. Fox and L. A. Loeb, *Annual Review of Pathology: Mechanisms of Disease*, 2010, **5**, 51–75.

19 F. Colotta, P. Allavena, A. Sica, C. Garlanda and A. Mantovani, *Carcinogenesis*, 2009, **30**, 1073–1081.

20 J. S. Flier, L. H. Underhill and H. F. Dvorak, *N. Engl. J. Med.*, 1986, **315**, 1650–1659.

21 F. Pagès, J. Galon, M. C. Dieu-Nosjean, E. Tartour, C. Sautès-Fridman and W. H. Fridman, *Oncogene*, 2010, **29**, 1093–1102.

22 O. Warburg, *Science (1979).*, 1956, **123**, 309–314.

23 O. Warburg, *Science (1979).*, 1956, **124**, 269–270.

24 M. G. V. Heiden, L. C. Cantley and C. B. Thompson, *Science (1979).*, 2009, **324**, 1029–1033.

25 R. G. Jones and C. B. Thompson, *Genes Dev.*, 2009, **23**, 537–548.

26 P. P. Hsu and D. M. Sabatini, *Cell*, 2008, **134**, 703–707.

27 R. J. DeBerardinis, J. J. Lum, G. Hatzivassiliou and C. B. Thompson, *Cell Metab.*, 2008, **7**, 11–20.

28 B. Thienpont, L. Van Dyck and D. Lambrechts, *Mol. Cell. Oncol.*, DOI:10.1080/23723556.2016.1240549.

29 P. A. Gameiro and K. Struhl, *Cell Rep.*, 2018, **24**, 1415–1424.

30 B. A. Helmink, M. A. W. Khan, A. Hermann, V. Gopalakrishnan and J. A. Wargo, *Nat. Med.*, 2019, **25**, 377–388.

31 A. Dzutsev, J. H. Badger, E. Perez-Chanona, S. Roy, R. Salcedo, C. K. Smith and G. Trinchieri, *Annu. Rev. Immunol.*, 2017, **35**, 199–228.

32 S. Lee and C. A. Schmitt, *Nat. Cell Biol.*, 2019, **21**, 94–101.

33 D. V. Faget, Q. Ren and S. A. Stewart, *Nat. Rev. Cancer*, 2019, **19**, 439–453.

34 N. A. Lobo, Y. Shimono, D. Qian and M. F. Clarke, *Annu. Rev. Cell Dev. Biol.*, 2007, **23**, 675–699.

35 R. W. Cho and M. F. Clarke, *Curr. Opin. Genet. Dev.*, 2008, **18**, 48–53.

36 A. P. Klein, *Nat. Rev. Gastroenterol. Hepatol.*, 2021, **18**, 493.

37 V. Corbo, G. Tortora and A. Scarpa, *Curr. Drug Targets*, 2012, **13**, 744–752.

38 J. D. Mizrahi, R. Surana, J. W. Valle and R. T. Shroff, *The Lancet*, 2020, **395**, 2008–2020.

39 M. Osmola, B. Gierej, K. Mleczko-Sanecka, A. Jończy, O. Ciepiela, L. Kraj, B. Ziarkiewicz-Wróblewska and G. W. Basak, *Current Oncology*, 2023, **30**, 7722.

40 R. Khadka, W. Tian, X. Hao and R. Koirala, *International Journal of Surgery*, 2018, **52**, 342–346.

41 A. Adamska, A. Domenichini and M. Falasca, *Int. J. Mol. Sci.*, DOI:10.3390/IJMS18071338.

42 T. Conroy, F. Desseigne, M. Ychou, O. Bouché, R. Guimbaud, Y. Bécouarn, A. Adenis, J.-L. Raoul, S. Gourgou-Bourgade, C. de la Fouchardière, J. Bennouna, J.-B. Bachet, F. Khemissa-Akouz, D. Péré-Vergé, C. Delbaldo, E. Assenat, B. Chauffert, P. Michel, C. Montoto-Grillot and M. Ducreux, *N. Engl. J. Med.*, 2011, **364**, 1817–1825.

43 D. D. Von Hoff, T. Ervin, F. P. Arena, E. G. Chiorean, J. Infante, M. Moore, T. Seay, S. A. Tjulandin, W. W. Ma, M. N. Saleh, M. Harris, M. Reni, S. Dowden, D. Laheru, N. Bahary, R. K. Ramanathan, J. Tabernero, M. Hidalgo, D. Goldstein, E. Van Cutsem, X. Wei, J. Iglesias and M. F. Renschler, *New England Journal of Medicine*, 2013, **369**, 1691–1703.

44 J. P. Neoptolemos, D. D. Stocken, H. Friess, C. Bassi, J. A. Dunn, H. Hickey, H. Beger, L. Fernandez-Cruz, C. Dervenis, F. Lacaine, M. Falconi, P. Pederzoli, A. Pap, D. Spooner, D. J. Kerr and M. W. Büchler, *N. Engl. J. Med.*, 2004, **350**, 1200–1210.

45 E. Morgan, M. Arnold, A. Gini, V. Lorenzoni, C. J. Cabasag, M. Laversanne, J. Vignat, J. Ferlay, N. Murphy and F. Bray, *Gut*, 2023, **72**, 338–344.

46 M. Maida, F. S. Macaluso, G. Ianiro, F. Mangiola, E. Sinagra, G. Hold, C. Maida, G. Cammarota, A. Gasbarrini and G. Scarpulla, *Expert Rev. Anticancer Ther.*, 2017, **17**, 1131–1146.

47 L. Roncucci and F. Mariani, *Eur. J. Intern. Med.*, 2015, **26**, 752–756.

48 B. Duan, Y. Zhao, J. Bai, J. Wang, X. Duan, X. Luo, R. Zhang, Y. Pu, M. Kou, J. Lei and S. Yang, *Gastrointestinal Cancers*, 2022, 1–12.

49 S. Łukasiewicz, M. Czeczelewski, A. Forma, J. Baj, R. Sitarz and A. Stanisławek, *Cancers 2021, Vol. 13, Page 4287*, 2021, **13**, 4287.

50 B. Weigelt, F. L. Baehner and J. S. Reis-Filho, *J. Pathol.*, 2010, **220**, 263–280.

51 F. Ades, D. Zardavas, I. Bozovic-Spasojevic, L. Pugliano, D. Fumagalli, E. De Azambuja, G. Viale, C. Sotiriou and M. Piccart, *J. Clin. Oncol.*, 2014, **32**, 2794–2803.

52 S. A. Roberts, M. S. Lawrence, L. J. Klimczak, S. A. Grimm, D. Fargo, P. Stojanov, A. Kiezun, G. V. Kryukov, S. L. Carter, G. Saksena, S. Harris, R. R. Shah, M. A. Resnick, G. Getz and D. A. Gordenin, *Nat. Genet.*, 2013, **45**, 970–976.

53 L. A. Newman, J. S. Reis-Filho, M. Morrow, L. A. Carey and T. A. King, *Ann. Surg. Oncol.*, 2015, **22**, 874–882.

54 Y. Li, D. Yang, X. Yin, X. Zhang, J. Huang, Y. Wu, M. Wang, Z. Yi, H. Li, H. Li and G. Ren, *JAMA Netw. Open*, 2020, **3**, E1918160.

55 A. E. Obr and D. P. Edwards, *Mol. Cell. Endocrinol.*, 2012, **357**, 4–17.

56 B. A. Kohler, R. L. Sherman, N. Howlader, A. Jemal, A. B. Ryerson, K. A. Henry, F. P. Boscoe, K. A. Cronin, A. Lake, A. M. Noone, S. J. Henley, C. R. Eheman, R. N. Anderson and L. Penberthy, *J. Natl. Cancer Inst.*, DOI:10.1093/JNCI/DJV048.

57 A. Brown, S. Kumar and P. B. Tchounwou, *J. Cancer Sci. Ther.*

58 B. Rosenberg, L. Van Camp and T. Krigas, *Nature*, 1965, **205**, 698–699.

59 H. Boer, J. H. Proost, J. Nuver, S. Bunskoek, J. Q. Gietema, B. M. Geubels, R. Altena, N. Zwart, S. F. Oosting, J. M. Vonk, J. D. Lefrandt, D. R. A. Uges, C. Meijer, E. G. E. de Vries and J. A. Gietema, *Annals of Oncology*, 2015, **26**, 2305.

60 G. V. Kondagunta, J. Sheinfeld, M. Mazumdar, T. V. Mariani, D. Bajorin, J. Bacik, G. J. Bosl and R. J. Motzer, *Journal of Clinical Oncology*, 2004, **22**, 464–467.

61 P. L. Zorat, A. Paccagnella, G. Cavaniglia, L. Loreggian, A. Gava, C. A. Mione, F. Boldrin, C. Marchiori, F. Lunghi, A. Fede, A. Bordin, M. C. Da Mosto, V. C. Sileni, A. Orlando, A. Jirillo, L. Tomio, G. L. Pappagallo and M. G. Ghi, *J. Natl. Cancer Inst.*, 2004, **96**, 1714–1717.

62 H. Von der Maase, S. W. Hansen, J. T. Roberts, L. Dogliotti, T. Oliver, M. J. Moore, I. Bodrogi, P. Albers, A. Knuth, C. M. Lippert, P. Kerbrat, P. Sanchez Rovira, P. Wersall, S. P. Cleall, D. F. Roychowdhury, I. Tomlin, C. M. Visseren-Grul and P. F. Conte, *J. Clin. Oncol.*, 2000, **18**, 3068–3077.

63 G. V. Scagliotti, F. De Marinis, M. Rinaldi, L. Crinò, C. Gridelli, S. Ricci, E. Matano, C. Boni, M. Marangolo, G. Failla, G. Altavilla, V. Adamo, A. Ceribelli, M. Clerici, F. Di Costanzo, L. Frontini and M. Tonato, *J. Clin. Oncol.*, 2002, **20**, 4285–4291.

64 J. Valle, H. Wasan, D. H. Palmer, D. Cunningham, A. Anthoney, A. Maraveyas, S. Madhusudan, T. Iveson, S. Hughes, S. P. Pereira, M. Roughton and J. Bridgewater, *N. Engl. J. Med.*, 2010, **362**, 1273–1281.

65 L. Qi, Q. Luo, Y. Zhang, F. Jia, Y. Zhao and F. Wang, *Chem. Res. Toxicol.*, 2019, **32**, 1469–1486.

66 A. M. J. Fichtinger-Schepman, P. H. M. Lohman, J. L. van der Veer, J. H. J. den Hartog and J. Reedijk, *Biochemistry*, 1985, **24**, 707–713.

67 B. Köberle, M. T. Tomicic, S. Usanova and B. Kaina, *Biochim. Biophys. Acta Rev. Cancer*, 2010, **1806**, 172–182.

68 L. Amable, *Pharmacol. Res.*, 2016, **106**, 27–36.

69 H. H. Hsu, M. C. Chen, R. Baskaran, Y. M. Lin, C. H. Day, Y. J. Lin, C. C. Tu, V. Vijaya Padma, W. W. Kuo and C. Y. Huang, *J. Cell. Physiol.*, 2018, **233**, 5458–5467.

70 D. J. Stewart, *Crit. Rev. Oncol. Hematol.*, 2007, **63**, 12–31.

71 S. Leijen, S. A. Burgers, P. Baas, D. Pluim, M. Tibben, E. Van Werkhoven, E. Alessio, G. Sava, J. H. Beijnen and J. H. M. Schellens, *Invest. New Drugs*, 2015, **33**, 201–214.

72 J. L. Spratlin, G. M. O'Kane, D.-Y. Oh, S. Y. Rha, E. McWhirter, E. Elimova, P. Kavan, M. K. Choi, D. W. Kim, R. A. Goodwin, J. R. Hecht, S. T. Kim, D.-H. Koo, K. Halani, E. R. McAllister, M. Jones, M. Snow, Y. Lemmerick, G. Spera and J. Pankovich, *Journal of Clinical Oncology*, 2024, **42**, 143–143.

73 C. G. Hartinger, M. A. Jakupec, S. Zorbas-Seifried, M. Groessl, A. Egger, W. Berger, H. Zorbas, P. J. Dyson and B. K. Keppler, *Chem. Biodivers.*, 2008, **5**, 2140–2155.

74 M. Cini, T. D. Bradshaw and S. Woodward, *Chem. Soc. Rev.*, 2017, **46**, 1040–1051.

75 G. Gasser, I. Ott and N. Metzler-Nolte, *J. Med. Chem.*, 2010, **54**, 3–25.

76 H. Köpf and P. Köpf-Maier, *Angewandte Chemie International Edition in English*, 1979, **18**, 477–478.

77 E. Meléndez, *Crit. Rev. Oncol. Hematol.*, 2002, **42**, 309–315.

78 B. K. Keppler, C. Friesen, H. G. Moritz, H. Vongerichten and E. Vogel, 1991, 97–127.

79 E. Y. Tshuva and J. A. Ashenhurst, *Eur. J. Inorg. Chem.*, 2009, **2009**, 2203–2218.

80 U. Schatzschneider, *Met. Ions Life Sci.*, 2018, **18**, 387–436.

81 E. Y. Tshuva, N. Gendeziuk and M. Kol, *Tetrahedron Lett.*, 2001, **42**, 6405–6407.

82 M. Miller and E. Y. Tshuva, *Sci. Rep.*, 2018, **8**, 1–9.

83 E. Y. Tshuva, M. Versano, I. Goldberg, M. Kol, H. Weitman and Z. Goldschmidt, *Inorg. Chem. Commun.*, 1999, **2**, 371–373.

84 M. Abid, R. Nouch, T. D. Bradshaw, W. Lewis and S. Woodward, *Eur. J. Inorg. Chem.*, 2019, **2019**, 2774–2780.

85 M. Musa, M. Abid, T. D. Bradshaw, D. J. Boocock, C. Coveney, S. P. Argent and S. Woodward, *J. Med. Chem.*, 2024, **67**, 2732–2744.

86 Musa Mustapha, *DESIGN, SYNTHESIS, CHARACTERISATION AND OPTIMISATION FOR TITANIUM COMPLEXES FOR ANTICANCER ACTIVITY*, 2023.

87 S. Meker, O. Braitbard, K. Margulis-Goshen, S. Magdassi, J. Hochman and E. Y. Tshuva, *Molecules*, 2015, **20**, 18526.

88 S. Bhaskar and S. Lim, *NPG Asia Mater.*, 2017, **9**, e371–e371.

89 N. M. Molino and S. W. Wang, *Curr. Opin. Biotechnol.*, 2014, **28**, 75–82.

90 A. B. Mason, S. L. Byrne, S. J. Everse, S. E. Roberts, N. D. Chasteen, V. C. Smith, R. T. A. MacGillivray, B. Kandemir and F. Bou-Abdallah, *Journal of Molecular Recognition*, 2009, **22**, 521–529.

91 P. V. Candelaria, L. S. Leoh, M. L. Penichet and T. R. Daniels-Wells, *Front. Immunol.*, 2021, **12**, 607692.

92 A. Essaghir and J. B. Demoulin, *PLoS One*, 2012, **7**, e39666.

93 K. A. O'Donnell, D. Yu, K. I. Zeller, J. Kim, F. Racke, A. Thomas-Tikhonenko and C. V. Dang, *Mol. Cell. Biol.*, 2006, **26**, 2373–2386.

94 X. P. Jiang and R. L. Elliott, *Anticancer Res.*, 2017, **37**, 2297–2305.

95 N. S. Kenneth, S. Mudie, S. Naron and S. Rocha, *Biochemical Journal*, 2012, **449**, 275.

96 A. Jain, A. Jain, N. K. Garg, R. K. Tyagi, B. Singh, O. P. Katare, T. J. Webster and V. Soni, *Acta Biomater.*, 2015, **24**, 140–151.

97 B. (Pandya) Shesh and J. R. Connor, *Biochim. Biophys. Acta Rev. Cancer*, 2023, **1878**, 188917.

98 M. A. Knovich, J. A. Storey, L. G. Coffman, S. V. Torti and F. M. Torti, *Blood Rev.*, 2009, **23**, 95–104.

99 G. Deng, Y. Li, N. Liang, P. Hu, Y. Zhang, L. Qiao, Y. Zhang, J. Xie, H. Luo, F. Wang, F. Chen, F. Liu, D. Xu and J. Zhang, *Cancer Med.*, 2023, **12**, 11570.

100 N. Gálvez, B. Fernandez, E. Valero, P. Sánchez, R. Cuesta and J. M. Domínguez-Vera, *Comptes Rendus Chimie*, 2008, **11**, 1207–1212.

101 M. Liu, L.-E. Quek, G. Sultani and N. Turner, *Cancer & Metabolism 2016 4:1*, 2016, **4**, 1–13.

102 Y. Shichi, N. Sasaki, M. Michishita, F. Hasegawa, Y. Matsuda, T. Arai, F. Gomi, J. Aida, K. Takubo, M. Toyoda, H. Yoshimura, K. Takahashi and T. Ishiwata, *Sci. Rep.*, 2019, **9**, 1–10.

103 L. Wang, P. Li, W. Hu, Y. Xia, C. Hu, L. Liu and X. Jiang, *Oncol. Lett.*, 2017, **14**, 1341.

104 D. Barnett, Y. Liu, K. Partyka, Y. Huang, H. Tang, G. Hostetter, R. E. Brand, A. D. Singhi, R. R. Drake and B. B. Haab, *Sci. Rep.*, 2017, **7**, 4020.

105 M. Li, R. Zhang, F. Li, H. Wang, J. K. Hee, L. Becnel, Q. Yao, C. Chen and W. E. Fisher, *J. Am. Coll. Surg.*, 2005, **201**, 571–578.

106 R. Gradiz, H. C. Silva, L. Carvalho, M. F. Botelho and A. Mota-Pinto, *Sci. Rep.*, 2016, **6**, 21648.

107 A. Farina, S. Tartaglione, A. Preziosi, P. Mancini, A. Angeloni and E. Anastasi, *Int. J. Mol. Sci.*, 2024, **25**, 3498.

108 M. Xu, X. Chen, Y. Han, C. Ma, L. Ma and S. Li, *Int. J. Clin. Exp. Med.*, 2015, **8**, 12476.

109 F. Bianchi, M. Sommariva, L. B. Cornaghi, L. Denti, A. Nava, F. Arnaboldi, C. Moscheni and N. Gagliano, *Cells*, 2022, **11**, 1318.

110 T. Ohnishi, N. Tomita, T. Monden, M. Ohue, I. Yana, K. Takami, H. Yamamoto, T. Yagyu, N. Kikkawa, T. Shimano and M. Monden, *Br. J. Cancer*, 1997, **75**, 341–347.

111 L. Sun, W. U. Shaoping, K. Coleman, K. C. Fields, L. E. Humphrey and M. G. Brattain, *Exp. Cell Res.*, 1994, **214**, 215–224.

112 M. P. Applanat, H. Buteau-Lozano, M. A. Herve and A. Corpet, *Adv. Exp. Med. Biol.*, 2008, **617**, 437–444.

113 A. Gougelet, C. Bouclier, V. Marsaud, S. Maillard, S. O. Mueller, K. S. Korach and J. M. Renoir, *Journal of Steroid Biochemistry and Molecular Biology*, 2005, **94**, 71–81.

114 J. P. Jacobs, C. M. Jones and J. P. Baille, *Nature*, 1970, **227**, 168–170.

115 M. Kapałczyńska, T. Kolenda, W. Przybyła, M. Zajączkowska, A. Teresiak, V. Filas, M. Ibbs, R. Bliźniak, Ł. Łuczewski and K. Lamperska, *Arch. Med. Sci.*, 2016, **14**, 910.

116 N. E. Ryu, S. H. Lee and H. Park, *Cells*, 2019, **8**, 1620.

117 R. Gradiz, H. C. Silva, L. Carvalho, M. F. Botelho and A. Mota-Pinto, *Sci. Rep.*, 2016, **6**, 1–14.

118 M. J. Ware, K. Colbert, V. Keshishian, J. Ho, S. J. Corr, S. A. Curley and B. Godin, *Tissue Eng. Part C Methods*, 2016, **22**, 312.

119 T. M. Achilli, J. Meyer and J. R. Morgan, *Expert Opin. Biol. Ther.*, 2012, **12**, 1347–1360.

120 R. Z. Lin, L. F. Chou, C. C. M. Chien and H. Y. Chang, *Cell Tissue Res.*, 2006, **324**, 411–422.

121 T. Mosmann, *J. Immunol. Methods*, 1983, **65**, 55–63.

122 J. van Meerloo, G. J. L. Kaspers and J. Cloos, *Methods Mol. Biol.*, 2011, **731**, 237–245.

123 T. L. Riss, R. A. Moravec, A. L. Niles, S. Duellman, H. A. Benink, T. J. Worzella and L. Minor, *Assay Guidance Manual*.

124 F. Denizot and R. Lang, *J. Immunol. Methods*, 1986, **89**, 271–277.

125 Musa M and Prayle S, .

126 E. J. Billo, *Excel for Chemists: A Comprehensive Guide*, Wiley–Blackwell, 2nd edn., 2001, vol. 25.

127 K. Gilmore, R. K. Mohamed and I. V. Alabugin, *Wiley Interdiscip. Rev. Comput. Mol. Sci.*, 2016, **6**, 487–514.

128 N. A. P. Franken, H. M. Rodermond, J. Stap, J. Haveman and C. van Bree, *Nat. Protoc.*, 2006, **1**, 2315–2319.

129 S. Zeng, M. Pöttler, B. Lan, R. Grützmann, C. Pilarsky and H. Yang, *Int. J. Mol. Sci.*, 2019, **20**, 4504.

130 R. Mezencev, L. V. Matyunina, G. T. Wagner and J. F. McDonald, *Cancer Gene Ther.*, 2016, **23**, 446.

131 L. Yao, J. Gu, Y. Mao, X. Zhang, X. Wang, C. Jin, D. Fu and J. Li, *Oncol. Lett.*, 2018, **15**, 5602.

132 M. Vinci, S. Gowan, F. Boxall, L. Patterson, M. Zimmermann, W. Court, C. Lomas, M. Mendiola, D. Hardisson and S. A. Eccles, *BMC Biol.*, 2012, **10**, 1–21.

133 S. El Harane, B. Zidi, N. El Harane, K. H. Krause, T. Matthes and O. Preynat-Seauve, *Cells 2023, Vol. 12, Page 1001*, 2023, **12**, 1001.

134 P. Longati, X. Jia, J. Eimer, A. Wagman, M. R. Witt, S. Rehnmark, C. Verbeke, R. Toftgård, M. Löhr and R. L. Heuchel, *BMC Cancer*, DOI:10.1186/1471-2407-13-95.

135 A. Acikgöz, S. Giri, M. G. Cho and A. Bader, *Biomolecules*, 2013, **3**, 242.

136 T. L. Place, F. E. Domann and A. J. Case, *Free Radic. Biol. Med.*, 2017, **113**, 311.

137 D. C. Poole, Y. Kano, S. Koga and T. I. Musch, *Comp. Biochem. Physiol. A Mol. Integr. Physiol.*, 2020, **253**, 110852.

138 J. P. Freyer and R. M. Sutherland, *J. Cell. Physiol.*, 1985, **124**, 516–524.

139 D. R. Grimes, P. Kannan, A. McIntyre, A. Kavanagh, A. Siddiky, S. Wigfield, A. Harris and M. Partridge, *PLoS One*, 2016, **11**, e0153692.

140 L. B. Weiswald, D. Bellet and V. Dangles-Marie, *Neoplasia*, 2015, **17**, 1.

141 F. Hirschhaeuser, H. Menne, C. Dittfeld, J. West, W. Mueller-Klieser and L. A. Kunz-Schughart, *J. Biotechnol.*, 2010, **148**, 3–15.

142 L. A. Kunz-Schughart, M. Kreutz and R. Knuechel, *Int. J. Exp. Pathol.*, 1998, **79**, 1–23.

143 E. Pupo, D. Avanzato, E. Middonti, F. Bussolino and L. Lanzetti, *Front. Oncol.*, 2019, **9**, 848.

144 S. Höfer, L. Frasch, S. Brajkovic, K. Putzker, J. Lewis, H. Schürmann, V. Leone, A. Sakhteman, M. The, F. P. Bayer, J. Müller, F. Hamood, J. T. Siveke, M. Reichert and B. Kuster, *Mol. Syst. Biol.*, 2025, **21**, 231–253.

145 G. J. LaBonia, S. Y. Lockwood, A. A. Heller, D. M. Spence and A. B. Hummon, *Proteomics*, 2016, **16**, 1814–1821.

146 M. Erlanson, E. Daniel-Szolgay and J. Carlsson, *Cancer Chemother. Pharmacol.*, 1992, **29**, 343–353.

147 W. Mueller-Klieser, J. P. Freyer and R. M. Sutherland, *Br. J. Cancer*, 1986, **53**, 345–353.

148 V. S. Murali, B. J. Chang, R. Fiolka, G. Danuser, M. C. Cobanoglu and E. S. Welf, *BMC Cancer*, 2019, **19**, 502.

149 O. Sirenko, T. Mitlo, J. Hesley, S. Luke, W. Owens and E. F. Cromwell, *https://home.liebertpub.com/adt*, 2015, **13**, 402–414.

150 S. J. Han, S. Kwon and K. S. Kim, *Cancer Cell Int.*, 2021, **21**, 1–19.

151 L. Kelland, *Nat. Rev. Cancer*, 2007, **7**, 573–584.

152 S. Dasari and P. Bernard Tchounwou, *Eur. J. Pharmacol.*, 2014, **740**, 364–378.

153 E. R. Camp, C. Wang, E. C. Little, P. M. Watson, K. F. Pirollo, A. Rait, D. J. Cole, E. H. Chang and D. K. Watson, *Cancer Gene Ther.*, 2013, **20**, 222.

154 Duncan Josh and Pan Michael, .

155 H. Abuzaid, S. Abdelrazig, L. Ferreira, H. M. Collins, D. H. Kim, K. H. Lim, T. S. Kam, L. Turyanska and T. D. Bradshaw, *ACS Omega*, 2022, **7**, 21473–21482.

156 A. A. Suran and H. Tarver, *Arch. Biochem. Biophys.*, 1965, **111**, 399–406.

157 R. R. Crichton and C. F. Bryce, *Biochem. J.*, 1973, **133**, 289–299.

158 R. R. Crichton, J. A. Soruco, F. Roland, M. A. Michaux, B. Gallois, G. Précigoux, J. P. Mahy and D. Mansuy, *Biochemistry*, 1997, **36**, 15049–15054.

159 M. Sun, Q. Xu, J. Xu, Y. Wu, Y. Wang, D. Zuo, Q. Guan, K. Bao, J. Wang, Y. Wu and W. Zhang, *PLoS One*, 2017, **12**, e0174006.

160 V. Ratushny, H. B. Pathak, N. Beeharry, N. Tikhmyanova, F. Xiao, T. Li, S. Litwin, D. C. Connolly, T. J. Yen, L. M. Weiner, A. K. Godwin and E. A. Golemis, *Oncogene*, 2012, **31**, 1217–1227.

161 T. Al-Warhi, A. M. El Kerdawy, M. A. Said, A. Albohy, N. Aljaeed, E. B. Elkaeed, W. M. Eldehna, H. A. Abdel-Aziz, Z. M. Elsayed and M. A. Abdelmoaz, *Drug Des. Devel. Ther.*, 2022, **16**, 1457–1471.

162 P. Oliva, V. Onnis, E. Balboni, E. Hamel, F. Estévez-Sarmiento, J. Quintana, F. Estévez, A. Brancale, S. Ferla, S. Manfredini and R. Romagnoli, *Molecules*, 2020, **25**, 2177.

163 P. Oliva, V. Onnis, E. Balboni, E. Hamel, F. Estévez-Sarmiento, J. Quintana, F. Estévez, A. Brancale, S. Ferla, S. Manfredini and R. Romagnoli, *Molecules*, 2020, **25**, 2177.

164 A. Erbaş, S. Dikim, F. Arslan, O. C. Bodur, S. Arslan, F. Özdemir and N. Sarı, *Bioinorg. Chem. Appl.*, 2025, **2025**, 2786064.

165 A. Erbaş, S. Dikim, F. Arslan, O. C. Bodur, S. Arslan, F. Özdemir and N. Sarı, *Bioinorg. Chem. Appl.*, 2025, **2025**, 2786064.

166 L. S. Blaser, U. Duthaler, J. Bouitbir, A. B. Leuppi-Taegtmeyer, E. Liakoni, R. Dolf, M. Mayr, J. Drewe, S. Krähenbühl and M. Haschke, *Front. Pharmacol.*, 2021, **12**, 620635.

167 Y. Teng and R. Liu, *J. Hazard. Mater.*, 2013, **262**, 318–324.

168 C. Chen and J. Zhang, *Cancers (Basel).*, 2024, **16**, 1171.

169 P. Chawengrum, N. Luepongpatthana, S. Thongnest, J. Sirirak, J. Boonsombat, K. Lirdprapamongkol, S. Keeratichamroen, P. Kongwaen, P. Montatip, P. Kittakoop, J. Svasti and S. Ruchirawat, *Sci. Rep.*, 2023, **13**, 1–18.

170 Afaq Adil, .

171 Vigo Annabella, *An Investigation Into the Anticancer Effects of Novel Schiff Base Derivatives of 4-Aminoantipyrine (4-AAP).*, .

172 S. Dasari and P. Bernard Tchounwou, *Eur. J. Pharmacol.*, 2014, **740**, 364–378.

173 L. Galluzzi, L. Senovilla, I. Vitale, J. Michels, I. Martins, O. Kepp, M. Castedo and G. Kroemer, *Oncogene*, 2012, **31**, 1869–1883.

174 *Anal. Chem.*, 2012, **67**, 563A-563A.

175 Y. Wang, H. Qi, Y. Liu, C. Duan, X. Liu, T. Xia, D. Chen, H. L. Piao and H. X. Liu, *Theranostics*, 2021, **11**, 4839.

176 C. A. Lipinski, F. Lombardo, B. W. Dominy and P. J. Feeney, *Adv. Drug Deliv. Rev.*, 1997, **23**, 3–25.

177 C. R. Park, H. Y. Kim, M. G. Song, Y. S. Lee, H. Youn, J. K. Chung, G. J. Cheon and K. W. Kang, *Int. J. Mol. Sci.*, 2020, **21**, 7932.

178 R. P. Perez, S. W. Johnson, L. M. Handel, P. J. O'Dwyer and T. C. Hamilton, *Gynecol. Oncol.*, 1995, **58**, 312–318.

179 M. Ćwiklińska-Jurkowska, M. Wiese-Szadkowska, S. Janciauskiene and R. Paprocka, *Molecules*, 2023, **28**, 5761.

180 A. E. Granada, A. Jiménez, J. Stewart-Ornstein, N. Blüthgena, S. Reber, A. Jambhekar and G. Lahav, *Mol. Biol. Cell*, 2020, **31**, 845–857.

5. APPENDIX

Appropriate electronic data have been deposited with S. Woodward and T. D. Bradshaw.

Table 5.1. Selected bond distances and angles for (**2.2a**).

Bond	Distance (Å)	Angle	(°)
N(1A)–C(2A)	1.4630(15)	C(2A)–N(1A)–C(11A)	110.52(9)
N(1A)–C(11A)	1.4765(15)	C(2A)–N(1A)–C(31A)	110.26(9)
N(1A)–C(31A)	1.4687(15)	C(31A)–N(1A)C–(11A)	111.30(9)
C(11A)–C(12A)	1.5053(16)	N(1A)–C(11A)–C(12A)	111.40(9)
C(12A)–C(13A)	1.3896(17)	C(13A)–C(12A)–C(11A)	119.11(10)
C(12A)–C(17A)	1.3976(17)	C(13A)–C(12A)–C(17A)	119.06(11)
C(13A)–C(14A)	1.4059(16)	C(17A)–C(12A)–C(11A)	121.75(11)
C(13A)–O(18A)	1.3579(14)	C(12A)–C(13A)–C(14A)	119.64(11)
C(14A)–C(15A)	1.3845(17)	O(18A)–C(13A)–C(12A)	118.52(10)
C(14A)–O(19A)	1.3667(15)	O(18A)–C(13A)–C(14A)	121.74(10)
C(15A)–C(16A)	1.3986(19)	C(15A)–C(14A)–C(13A)	120.32(11)
C(16A)–C(17A)	1.3842(18)	O(19A)–C(14A) –C(13A)	114.48(10)

C(16A)–C(21A)	1.5100(18)	O(19A)–C(14A) –C(15A)	125.19(11)
O(19A)–C(20A)	1.4303(15)	C(14A)–C(15A)–C(16A)	120.38(12)
C(31A)–C(32A)	1.5067(16)	C(15A)–C(16A)–C(21A)	120.13(12)
C(32A)–C(33A)	1.3934(17)	C(17A)–C(16A)–C(15A)	118.73(11)
C(32A)–C(37A)	1.3961(17)	C(17A)–C(16A)–C(21A)	121.14(12)
C(33A)–C(34A)	1.4071(16)	C(16A)–C(17A)–C(12A)	121.77(11)
C(33A)–O(38A)	1.3679(14)	C(14A)–O(19A)–C(20A)	116.60(10)
C(34A)–C(35A)	1.3869(19)	N(1A)–C(31A)–C(32A)	112.51(9)
C(34A)–O(39A)	1.3676(15)	C(33A)–C(32A)–C(31A)	120.45(10)
C(35A)–C(36A)	1.395(2)	C(33A)–C(32A)–C(37A)	119.42(11)
C(36A)–C(37A)	1.3850(18)	C(37A)–C(32A)–C(31A)	120.06(11)
C(36A)–C(41A)	1.5116(19)	C(32A)–C(33A)–C(34A)	119.47(11)
O(39A) – C(40A)	1.4332(15)	O(38A)–C(33A)–C(32A)	122.64(10)
		O(38A) –C(33A) –C(34A)	117.87(10)
		C(35A)–C(34A)–C(33A)	119.86(11)
		O(39A)–C(34A)–C(33A)	114.96(11)

		O(39A)–C(34A)–C(35A)	125.17(11)
		C(34A)–C(35A)–C(36A)	121.12(11)
		C(35A)–C(36A)–C(41A)	120.82(13)
		C(37A)–C(36A)–C(35A)	118.42(12)
		C(37A)–C(36A)–C(41A)	120.72(13)
		C(36A)–C(37A)–C(32A)	121.71(12)
		C(34A)–O(39A)–C(40A)	116.86(11)

Table 5.2. Selected bond distances and angles for (**2.4**).

Bond	Distance (Å)	Angle	(°)
N(1)–C(2)	1.4310(14)	C(2)–N(1)–C(13)	109.00(8)
C(5)–C(4)	1.3898(15)	C(4)–C(5)–C(6)	119.41(10)
C(5)–C(6)	1.3983(15)	C(4)–C(5)–C(13)	118.83(9)
C(5)–C(13)	1.5153(14)	C(6)–C(5)–C(13)	121.77(9)
C(4)–C(9)	1.4108(15)	O(3)–C(4)–C(5)	123.38(9)
C(6)–C(7)	1.3837(15)	O(3)–C(4)–C(9)	116.83(9)

C(9)–C(8)	1.3848(15)	C(5)–C(4)–C(9)	119.77(10)
C(8)–C(7)	1.4030(16)	C(7)–C(6)–C(5)	121.56(10)
C(7)–C(12)	1.5098(15)	O(10)–C(9)–C(4)	115.20(9)
O(3)–C(4)	1.3715(13)	O(10)–C(9)–C(8)	125.06(10)
O(3)–C(2)	1.4596(12)	C(8)–C(9)–C(4)	119.74(10)
O(10)–C(9)	1.3682(13)	C(9)–C(8)–C(7)	120.90(10)
O(10)–C(11)	1.4291(13)	N(1)–C(13)–C(5)	111.81(9)
N(1)–C(14)	1.4656(14)	N(1)–C(2)–O(3)	114.31(8)
N(1)–C(13)	1.4667(13)	C(6)–C(7)–C(8)	118.62(10)
		C(6)–C(7)–C(12)	121.33(10)
		C(8)–C(7)–C(12)	120.04(10)
		C(4)–O(3)–C(2)	113.72(8)
		C(9)–O(10)–C(11)	116.60(8)
		C(14)–N(1)–C(13)	112.01(8)
		C(2)–N(1)–C(14)	112.74(9)